# A Comprehensive Integrity Monitoring System for Bolted Flange Connections

by
Jinwei Jiang

A dissertation submitted to the Department of Mechanical Engineering,
Cullen College of Engineering
in partial fulfillment of the requirements for the degree of

DOCTOR OF PHILOSOPHY

in Mechanical Engineering

Chair of Committee: Dr. Gangbing Song

Committee Member: Dr. Matthew A. Franchek

Committee Member: Dr. Karolos Grigoriadis

Committee Member: Dr. Zheng Chen

Committee Member: Dr. Yi-Lung Mo

University of Houston
August 2020

# ACKNOWLEDGMENTS

First of all, I am extremely grateful to my advisor, Dr. Gangbing Song, for his vision and expertise that guide me to the structural health monitoring field. He always offered me valuable advises and full support through my Ph.D studies.

I would also like to thank my committee members, Dr. Matthew Franchek, Dr. Karolos Grigoriadis, Dr. Yi-Lung Mo and Dr. Zheng Chen, for their valuable time and constructive comments. Special thanks go to Dr. Franchek for his inspiration and scholarship, Dr. Mo for his help in structural lab, and Dr. Chen for his support in smart-touch project and help from his research team.

I would like to express my appreciation to all my colleagues at the Smart Martials and Structure Laboratory. In particular, special appreciation go to Dr. Michael Ho for his great help in countless ways, Dr. Qingzhao Kong and Dr. Chenyu Wang for their guides in instrumentation, Dr. Junxiao Zhu for his expertise in Matlab tool, Dr. Wenxi Wang for his teamwork in the basement lab, Dr. Xianfeng Wang for his insightful discussions, and Ms. Sihong He for her assistance in TA duties. In addition, Mr. Furui Wang, Mr. Wenyu Zuo, Mr. Xiongfeng Yi, Mr. Nathanael Markle, Mr. Taylor Tippitt, and Mr. Lucas Karwei Wong helped me in various research projects.

This research is supported by Texas Commission on Environmental Quality through Subsea Systems Institute (Award #582-15-57593), which is appreciated.

Finally, and the most importantly, I would like to greatly thank my family for their unconditional love, understanding and support these years.

# ABSTRACT

Bolted flange connections are commonly utilized to link pressure vessels and pipeline systems. Although there exists a series of design codes and standards to specify the design of flange joints, multiple adverse factors, such as unexpected loads and excessively high pressures and temperatures, can directly cause leakage failures of the flange connections in service. Leakage failures, if undetected, may result in crippling economic losses and sometimes irreversible environmental damages, especially for offshore applications. Therefore, integrity monitoring and inspection of both onshore and offshore bolted flange connections is necessary.

In this dissertation, a comprehensive integrity monitoring system is proposed and developed through the implementation of cutting-edge sensing technologies to thoroughly investigate the integrity of a bolted flange assembly under tensile loads, internal pressure loads and a combination of both. API 6A flanges (4-1/16”, Type 6B, 2000 psi) were selected to perform the proposed research. Fiber Bragg grating (FBG) -enabled bolts offer a direct measurement of the bolt strains in the flange assembly. The piezo-based active sensing method and the electromechanical impedance (EMI) method provide different approaches to monitor the characteristic variations in the metal-to-metal sealing condition. Upon seal failure, the acoustics generated by the sudden release of the escaping pressurized nitrogen gas were readily detected by the acoustic emission (AE) system. Meanwhile, the internal pressure of the flange assembly was simultaneously recorded as a reference for other measurements. Through the data analysis, this comprehensive integrity monitoring system provides useful insights of flange connection behaviors under different internal pressures and tensile loads and a preliminary understanding of a leakage failure envelope considering the bolt torques and tensile loads. Moreover, a touch-based sensing mechanism was also explored and further applied on a specifically designed robotic manipulator, which was incorporated with an undersea remotely operated vehicle (ROV) to comprise a remote inspection system for subsea bolted connections. Its undersea inspection performance was demonstrated through field testing in a local marine environment. Thus, the proposed comprehensive integrity monitoring system offers potential solutions for assuring the performance and integrity of onshore and offshore bolted flange joints in practical applications.

# TABLE OF CONTENTS

**ACKNOWLEDGMENTS .......... iii**

**ABSTRACT .......... iv**

**TABLE OF CONTENTS .......... vi**

**LIST OF TABLES .......... ix**

**LIST OF FIGURES .......... x**

**1. INTRODUCTION .......... 1**

- 1.1 Motivation and Objectives .......... 1
- 1.2 Contributions .......... 7
- 1.3 Organization .......... 10

**2. STRUCTURAL INTEGRITY MONITORING SYSTEMS .......... 12**

- 2.1 Piezo-based active Sensing Method .......... 12
  - 2.1.1 Spectrogram .......... 14
  - 2.1.2 Wavelet Packet-based Energy .......... 15
- 2.2 Electromechanical Impedance Measurement .......... 18
- 2.3 Acoustic Emission Leak Detection System .......... 20
- 2.4 FBG-enabled Bolt Strain Monitoring .......... 22

**3. MONITORING OF BOLTED FLANGE CONNECTIONS USING ELECTROMECHANICAL IMPEDANCE (EMI) METHOD .......... 24**

- 3.1 Introduction .......... 24
- 3.2 Experimental Setup and Procedures .......... 25
- 3.3 Results and Discussions .......... 27
  - 3.3.1 Results of Pressurization Process .......... 27
  - 3.3.2 Results of Depressurization Process .......... 32
- 3.4 Summary .......... 36

**4. LEAK DETECTION OF BOLTED FLANGE JOINT UNDER INTERNAL PRESSURE CONDITIONS .......... 38**

- 4.1 Introduction .......... 38

4.2 Experimental Setup and Procedures ........ 39
4.3 Results and Discussions ........ 41
    4.3.1 Results of FBG-enabled Strain Monitoring ........ 41
    4.3.2 Results of Acoustic Emission Detection ........ 45
4.4 Summary ........ 49

**5. A COMPREHENSIVE INTEGRITY MONITORING OF BOLTED FLANGE JOINT UNDER COMBINED TENSILE LOADS AND INTERNAL PRESSURE ........ 50**

5.1 Introduction ........ 50
5.2 Experimental Setup and Procedures ........ 52
5.3 Results and Discussions ........ 58
    5.3.1 Results of FBG-enabled Bolt Strain Monitoring ........ 58
    5.3.2 Results of AE Leak Detection System ........ 62
    5.3.3 Results of piezo-based Active Sensing ........ 65
    5.3.4 Results of Electromechanical Impedance ........ 67
    5.3.5 Results of leak-related Tension Limit ........ 72
5.4 Summary ........ 79

**6. A TOUCH-ENABLED INSPECTION APPROACH FOR SUBSEA BOLTED CONNECTIONS ........ 81**

6.1 Introduction ........ 81
6.2 Design for the Touch-enabled Sensing ........ 83
6.3 The Touch-enabled Active Sensing Method ........ 85
6.4 Experimental Setup and Procedures ........ 86
6.5 Results and Discussion ........ 88
    6.5.1 Time-domain Analysis of Active Sensing Results ........ 88
    6.5.2 Spectral Analysis of Active Sensing Results ........ 89
    6.5.3 Results of Wavelet Packet-based Energy Method ........ 91
6.6 Summary ........ 93

**7. REMOTELY OPERATED VEHICLE (ROV) ASSISTED ROBOTIC INSPECTION FOR UNDERSEA BOLTED CONNECTIONS ........ 95**

7.1 Introduction ........ 95

7.2 Characterization of ROV-enabled Undersea Robotic Inspection........... 96
    7.2.1 Waterproof Design of Piezoceramic Transducers....................... 96
    7.2.2 Touch-enabled Sensing Design of a Manipulator Model............ 97
    7.2.3 Design of ROV-enabled Robotic Inspection Tool ...................... 98
7.3 Principles for Undersea Bolted Connections Inspection ...................... 100
    7.3.1 Active Sensing Principle .......................................................... 100
    7.3.2 Spectrum Presentation Principle ............................................... 101
7.4 Undersea Test Setup and Procedures.................................................... 102
7.5 Undersea Test Results and Discussions................................................ 103
    7.5.1 Time-domain Representations................................................... 103
    7.5.2 Frequency-domain Representations .......................................... 105
    7.5.3 Wavelet Packet Transform-based Energy Results .................... 107
7.6 Summary................................................................................................ 108

**8. CONCLUSIONS AND FUTURE WORK.............................................. 110**

**REFERENCES........................................................................................... 113**

# LIST OF TABLES

Table 3-1 Summary of the first peak frequencies during pressurization process ........ 31

Table 3-2 Summary of the second peak frequencies during pressurization process ........ 31

Table 3-3 Summary of the first peak frequencies during the depressurization process ........ 35

Table 3-4 Summary of the second peak frequencies during the depressurization process ........ 35

Table 5-1 Summary of peak frequency of the flange assembly under tensile loads ........ 69

Table 5-2 Summary of conductance of the flange assembly under tensile loads ........ 69

Table 5-3 Summary of peak frequency of the flange assembly under combined tensile and internal pressure loads ........ 71

Table 5-4 Summary of conductance signatures of the flange assembly under combined tensile and internal pressure loads ........ 71

Table 5-5 Summary of leak-related tensile loads based on the results of internal pressure and FBG enable strain monitoring on bolts ........ 79

Table 6-1 Properties of PZT Transducers ........ 84

# LIST OF FIGURES

Figure 1-1 Cross-section of the bolted flange joint ................................................ 1

Figure 2-1 Demonstration of active sensing measurements ................................ 12

Figure 2-2 Illustration of a three-level wavelet packet decomposition ................ 16

Figure 2-3 Demonstration of AE detection measurement .................................... 20

Figure 2-4 Illustration of parameters within an AE signal ................................... 21

Figure 2-5 Principle of FBG sensors ................................................................... 22

Figure 2-6 Demonstration of the FBG-enable bolts strain monitoring ................ 23

Figure 3-1 Experimental setup of the bolted flange joint using EMI technique ............................................................................ 27

Figure 3-2 Raw date of the conductance signatures during pressurization process ............................................................................ 29

Figure 3-3 Processed date of the conductance signatures during pressurization process ............................................................ 29

Figure 3-4 Zoomed-in view of the conductance signatures around the first peak frequency during pressurization process .................................. 30

Figure 3-5 Zoomed-in view of the conductance signatures around the second peak frequency during pressurization process ........................ 30

Figure 3-6 Relationship of the peak frequencies and the increasing internal pressure ............................................................................ 31

Figure 3-7 Raw date of the conductance signatures during depressurization process ............................................................................ 33

Figure 3-8 Processed date of the conductance signatures during depressurization process .................................................................. 34

Figure 3-9 Zoomed-in view of the conductance signatures around the first peak frequency during the depressurization process ........................... 34

Figure 3-10 Zoomed-in view of the conductance signatures around the second peak frequency during the depressurization process ............ 35

Figure 3-11 Relationship of the peak frequencies and the decreasing internal pressure ............................................................................ 36

Figure 4-1 Experimental Setup and data acquisition system of leak detection investigation on the bolted flange assembly ........................ 41

Figure 4-2 Micro-II digital acoustic emission data acquisition system ................ 41

Figure 4-3 FBG-enabled Bolts with numbers on the flange assembly ................. 42

Figure 4-4 Pressure signals versus FBG-enabled strain monitoring on the Bolt-1 ........................................................................................ 43

Figure 4-5 Pressure signals versus FBG-enabled strain monitoring on the Bolt-3 ........................................................................................ 43

Figure 4-6 Pressure signals versus FBG-enabled strain monitoring on the Bolt-5 ........................................................................................ 44

Figure 4-7 Pressure signals versus FBG-enabled strain monitoring on the Bolt-7 ........................................................................................ 44

Figure 4-8 Pressure signals versus cumulative AE hit signals.............................. 47

Figure 4-9 Pressure signals versus transient AE hit signals in histogram bar ...... 47

Figure 4-10 Pressure signals versus cumulative AE energy signals ..................... 48

Figure 4-11 Pressure signals versus transient AE energy signals in histogram bar ........ 48

Figure 5-1 3D modeling of the bolted flange joint for tensile testing........ 53

Figure 5-2 Demonstration of the bolted flange joint on MTS test frame........ 54

Figure 5-3 A comprehensive monitoring system for flange joint on the MTS test frame........ 57

Figure 5-4 Experimental setup of transducers on the bolted flange joint ........ 57

Figure 5-5 Demonstration of active sensing measurement........ 58

Figure 5-6 Demonstration of electromechanical impedance Measurement........ 58

Figure 5-7 Experimental Results: (a)tensile loading from the MTS test frame, (b) FBG-enabled bolts numbering on the flange, (c) FBG strains on bolt-1, (d) FBG strains on bolt-3, (e) FBG strains on bolt-5, (f) FBG strains on bolt-7 ........ 60

Figure 5-8 Comparison of MTS loadings and FBG strains on bolt-7........ 61

Figure 5-9 Comparison of internal pressure and FBG strains on bolt-7........ 61

Figure 5-10 Comparison of FBG strains and the transient AE energy signals ........ 63

Figure 5-11 Comparison of FBG strains and the cumulative AE energy signals ........ 63

Figure 5-12 Comparison of internal pressure and the transient AE energy signals ........ 64

Figure 5-13 Comparison of internal pressure and the cumulative AE energy signals ........ 64

Figure 5-14 Active sensing results under different tensile loads .......................... 65

Figure 5-15 Comparison of each piezo-based active sensing results under tensile loads (a) time-domain response and (b) wavelet packet-based energy index .......................................................................... 66

Figure 5-16 Active sensing results under combined tensile loads and internal pressure .................................................................................. 66

Figure 5-17 Comparison of active sensing results under combined tensile loads and internal pressure (a) time-domain response and (b) wavelet packet-based energy index ................................................. 67

Figure 5-18 Conductance signatures of the flange assembly under tensile loads ........................................................................................................ 68

Figure 5-19 Zoomed-in view of conductance signatures of the flange assembly under tensile loads ........................................................... 69

Figure 5-20 Summary of peak frequency and conductance under the tensile loads ........................................................................................................ 70

Figure 5-21 Conductance signatures of the flange assembly under combined tensile and internal pressure loads ................................... 70

Figure 5-22 Zoomed-in view of conductance signatures of the flange assembly under combined tensile and internal pressure loads ......... 71

Figure 5-23 Summary of peak frequencies and conductance signatures under the applied tensile and internal pressure loads ....................... 72

Figure 5-24 Leak-related tension test results of the bolted flange joint under tightened torque of 20 ft-lb (a) internal pressure and (b) FBG strains ..................................................................................................... 74

Figure 5-25 Leak-related tension test results of the bolted flange joint under tightened torque of 25 ft-lb (a) internal pressure and (b) FBG strains ........ 75

Figure 5-26 Leak-related tension test results of the bolted flange joint under tightened torque of 30 ft-lb (a) internal pressure and (b) FBG strains ........ 76

Figure 5-27 Leak-related tension test results of the bolted flange joint under tightening torque of 35 ft-lb (a) internal pressure and (b) FBG strains ........ 77

Figure 5-28 Leak-related tension test results of the bolted flange joint under tightening torque of 40 ft-lb (a) internal pressure and (b) FBG strains ........ 78

Figure 5-29 Relationship between the bolt torques and the leak-related tensile loads ........ 79

Figure 6-1 Envision of an underwater robotic vehicle incorporated with the piezo-based portable sensing approach for the inspection of subsea bolted connections. ........ 82

Figure 6-2 Configuration of an enabled PZT transducer assembly ........ 85

Figure 6-3 A proof-of-concept design of the touch-based sensing device........ 85

Figure 6-4 Method of active sensing measurement using the proposed touch-based inspection approach ........ 87

Figure 6-5 Test specimen in different environments: (a) in air and (b) in salt water. ........ 88

Figure 6-6 Time-domain active sensing responses in air........ 89

Figure 6-7 Time-domain active sensing responses in salt water ........ 89

Figure 6-8 Spectrograms of active sensing results in air ..................................... 91

Figure 6-9 Spectrograms of active sensing results in saltwater ............................ 91

Figure 6-10 Results of wavelet packet-based energy index (a) in air, (b) in salt water. ......................................................................... 92

Figure 7-1 Configuration of an enabled piezoceramic transducer ........................ 97

Figure 7-2 Design of a robotic sensing manipulator: (a) a manipulator integrated with piezoceramic transducers; (b) a cutaway view of the transducer assembly. .................................................................... 98

Figure 7-3 Illustration of the ROV enabled robotic inspection tool: (a) the ROV; (b) the integration of the ROV with the PZT-based sensing manipulator; (c) the main dimension of the entire ROV enabled robotic inspection tool. ......................................................... 99

Figure 7-4 Illustration of the ROV-enabled robotic inspection principle ........... 101

Figure 7-5 Experimental demonstration of bolted connection inspection: (a) and (b) in water tank in laboratory; (c) and (d) undersea tests in field ............................................................................................. 103

Figure 7-6 Time-domain response of undersea bolt inspection in field............. 104

Figure 7-7 Frequency-domain response of undersea bolt inspection in field: (a) the comparison in 3-D view; (b) the comparison in zoomed-in view............................................................................................ 106

Figure 7-8 Wavelet packet transform-based energy index of undersea bolt inspection .......................................................................................... 108

# 1. Introduction

## 1.1 Motivation and Objectives

Bolted flange connections typically includes two flanges, a ring-type gasket and multiple bolts [1], as shown in Fig. 1-1. Through tightening the bolts, the generated axial loads compress the mating surface between the ring gasket and the flange grooves to initialize a metal-to-metal seal [2]. Bolted flange connections are commonly utilized to link pressure vessels and pipeline systems [3], including offshore engineering structures, such as blowout preventers (BOPs), subsea risers [4, 5]. When the internal contents with pressure flow through the bolted flange connectors, the hydrostatic end forces always attempt to separate the flange components against the forces from the torqued bolts and blow out from the ring gasket [6]. Therefore, a prime concern of bolted flange connections is bolt and connector failure, which may cause a catastrophic result.

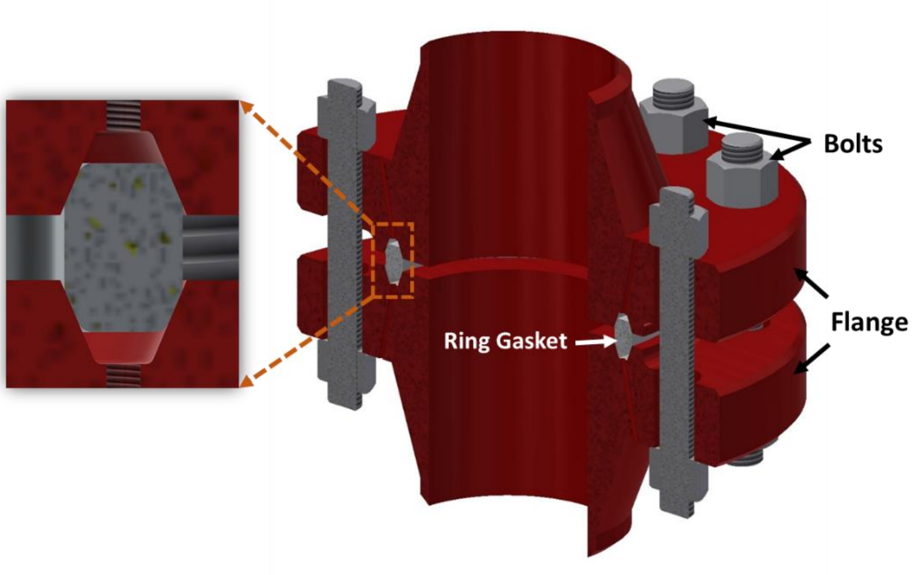

Figure 1-1 Cross-section of the bolted flange joint

Although there exists a series of design codes and standards to specify the design of flange joints, multiple adverse factors, such as unexpected loads and excessively high pressures, vibration and fatigue [7, 8], erosion [9, 10], corrosion [11, 12], ground movement [13], and impacts by foreign objects [14], may potentially cause leakage failures of the flange connections in service. Leakage failures, if undetected, may result in crippling economic losses and even sometimes irreversible environmental damages, especially for subsea environment. Therefore, to improve the reliability of the bolted connections and mitigate the occurrence and consequences of these failures, integrity monitoring or inspection of bolted flange connections is necessary [15].

With the recent advances in structural health monitoring (SHM) [16-18] and damage detection [19-21], many inspection and monitoring methods have been explored to determine the integrity of bolted connections on land [22]. As an old fashion way, inspectors draw a line across both the bolt and the host structure when the connection is satisfactorily tightened. Over time, misalignment of the line can indicate the looseess of the bolt. This method is still commonly used nowadays. With the introduction of high performance cameras and advanced image processing algorithms, the vision-based inspection method is now being automated [23-25]. For example, by using the Hough transform, Wang developed a new image based method to accurately determine the rotation angle of a bolt/nut to reveal bolt loosening [26]. However, in general the image based methods cannot detect the loss of the preload of a bolt connection since the bolt rotation indicates most of the preload has already been lost. Most recently, an unmanned aerial vehicle (UAV) was incorporated with digital camera devices to further improve the visual inspection method [27, 28]. The UAV was remotely controlled by an operator on ground to capture images of the targets, thereby achieving a remote visual inspection for large-scale structures [29], such as wind turbines [30], bridges [31] and buildings [32]. The UAV-assisted visual inspection methods can significantly improve the efficiency of inspection tasks with high flexibility and reduce the operation risk of human [33].

Strain sensors, such as strain gauges and fiber optic sensors (FOSs), are often integrated with bolts for pre-load estimation. While electrical strain gauges are able to provide the required data, fiber optic sensor (FOS) based strain sensors are less invasive and less affect bolt performance due to the much-less profile of the optic fibers [34, 35]. Vibration induced by using a shaker [36] and a laser beam [37] have also been reported for the inspection of bolt joint integrity. In addition, sound generated from an impact on a bolt connection has been used [38-40]. Due to the advantages of dual sensing and actuation, piezoceramic transducers, especially PZT (Lead Zirconate Titanate) transducers, have been widely explored for structural health monitoring [41, 42]. PZT transducers have the ability to generate stress waves, ultrasonic waves, and guided waves for structural health monitoring [43-46], including bolt monitoring [47, 48]. The PZT-transducer enabled active sensing method, which employs one transducer to generate a stress wave that travels across the bolted connection and another PZT transducer to detect the propagating wave, has been employed to monitoring bolt connection [49]. Analyses of the detected wave’s properties, such as the attenuation of the signal strength and shifting of frequency components, reveal the insight of the status of the bolt connection [50]. Also using PZT transducers, electromechanical impedance (EMI) based method has been developed to be a useful nondestructive testing (NDT) method [51, 52], which has been wildly used to monitor structural integrity in mechanical and civil structures [53-55], including the bolted connection monitoring [56-58]. The impedance-based measurements take the advantages of the direct and converse piezoelectric effects of the transducer, which ensures the PZT patch simultaneously function as an actuator and sensor through an impedance analyzer [59]. Through the interface between the surface-bonded piezoceramic patch and the monitored specimen, the electrical impedance signature of the piezoceramic path is highly correlated to the mechanical properties of the host structure, especially for the local area where the piezoceramic patch was mounted [60]. Therefore, damages or characteristics changes in the host structure can be directly reflected on the electromechanical impedance signatures [61].

Furthermore, acoustic emission (AE) technique is another promising nondestructive evaluation methods for a broad variety of materials [62] and structures [63], including bridges monitoring [64-67], fatigue creaks [68, 69], and especially for leak detection of pipelines and pressure vessels [70-73]. AE describes a phenomenon of transient elastic stress waves that generated by a rapid release of energy from a localized source in a structure subjected to a sudden change of pressure, load or temperature [63]. The waves propagate through the structure and are then detected and converted into electrical voltage signals by an AE sensor which are directly mounted on the surface [74]. The key component of an AE sensor is piezoelectric materials, encased in a protective housing, and AE probes can cover a wide frequency range of 1 kHz to 1 MHz depending on the nature of the sources and the selected band-pass filters [63].

Among the reviewed bolt connection monitoring methods on land, the PZT-based approaches hold a great promise of the further development of inspection approach for subsea bolted connections because of the advantages, such as small size, light-weight, cost-effectiveness, and robustness [75, 76]. However, the typical PZT based methods require permanent installation of transducers onto or near the bolted connections, which may be difficult for subsea applications. Therefore, an approach to inspecting bolt connection without the permanent installation of PZT transducers should be developed. To avoid the permanent bonding condition between the transducer and the inspected structure, a touch-based sensing device is proposed to utilize magnetic forces for providing a temporary and effective coupling condition between the transducers and the bolted specimen. Since stress wave can be transmitted upon touching or contact, it is possible to integrate PZT transducers with the fingers of a robotic manipulator to enable the touch-based active sensing method for bolted connection inspection. Considering the difficulty of accessing subsea pipelines by human divers, this potential method shall be easily integrated with a subsea robotic system, such as a remotely operated vehicle (ROV). Recently, an unmanned underwater vehicle (UUV) becomes one of the most useful devices for conducting remote tasks [77]. ROV is one type of UUVs and is tethered with an umbilical cable. Through this umbilical cable, the ROV’s motion undersea can be remotely controlled by an operator on land [78]. To date, ROVs have been used to accomplish various mission-related tasks in shallow or deep sea [79], such as geotechnical investigations, mineral explorations, environmental monitoring applications and offshore engineering operations [80]. Furthermore, a robot manipulator has been wildly used with UUVs to execute subsea operations [81]. Therefore, a manipulator equipped with sensing devices can be used to conduct remote inspections for undersea bolted connections. For the sensing part, PZT transducers were selected due to their cost-effectiveness and dual sensing and actuation functions [42]. Furthermore, PZT-based inspection/monitoring applications have been widely developed. [75, 82]. The associated acoustic and vibration-based analysis have been employed to monitor the integrity of a variety of structures, including bolted connections [40, 47, 48, 83]. By using active sensing method, one pair of piezoceramic transducers were bonded on the structure in a way that one transducer generated a reference signal as stress waves to travel across the interest area of the structure and anther transducer simultaneously acquired the transmitted signals [84, 85]. Based on the acquired signal's characteristics, such as signal strength or signal energy, it can offer insights of the integrity of the structure. However, the proposed undersea ROV-enable remote inspection system using touch-based active sensing method for inspecting bolted connections has not been explored on the same topic in subsea environment.

Therefore, the primary objective of this dissertation is to develop a comprehensive integrity monitoring system through the implementation of cutting-edge sensing technologies for bolted flange connection onshore and offshore. First of all, a thorough investigation of the integrity of a bolted flange assembly will be conducted under tensile loads, internal pressure loads and the combination of them, respectively.

The monitoring techniques include FBG based bolt strain monitoring, piezo-based active sensing and the electromechanical impedance monitoring, AE leak detection, and internal pressure measurements. Secondly, the potential effective sensing technologies on land will be further advanced in a portable manner for remotely conducting subsea bolted connections. A touch-based sensing mechanism will be explored and further applied on a specifically designed robotic manipulator, which will be incorporated with an undersea remotely operated vehicle (ROV) to achieve a remote inspection system for undersea bolted connections. The inspection performance will also be demonstrated through an undersea field evaluation. Therefore, the proposed research of the comprehensive integrity monitoring system can provide a real-time monitoring of the bolted flange joints for an in-depth understanding of the behaviors of on shore flange connections under a variety of tensile loads, internal pressure load and the combination of them. Additionally, a touch-based inspection technology can be used by a ROV and robotic manipulator to effectively inspect the status of subsea bolted connections. Consequently, the proposed research offers potential solutions for assuring the performance and integrity of both onshore and offshore bolted flange connections to reduce mitigate the occurrence and consequences of bolt and connection failures.

## 1.2 Contributions

The contributions of this dissertation are multifold:

First of all, a new piezo-based electromechanical impedance technique was developed and experimentally verified by using a pair of API 6A flanges (4-1/16”, Type 6B, 2000 psi), which were selected and specifically designed and fabricated to accommodate for pressurization and tensile loading tests. The piezo-based electromechanical impedance technique was studied the characteristic changes over the bolted flange connection under the internal pressure loads during both pressurization and depressurization process. A repeatability study reveals that a near-linear relationship between the resonant frequencies and the corresponding internal pressures, which verifies the effectiveness of the proposed electromechanical impedance method in monitoring the pressure-induced variations in the bolted flange joint.

Secondly, a comprehensive system of leak detection of a bolted flange joint assembly was developed by using acoustic emission system, internal pressure measurement, and FBG-enabled bolts strain monitoring. The leak around the ring gasket was induced by continuously injecting nitrogen gas. By analyzing the signals, results of FBG sensors clearly illustrated the strain changes under the different internal pressures; acoustic signals identified the moment of the pressure-induced leak in the features of AE hits and AE energy; and the leak-related pressure was also determined by the pressure signals.

Thirdly, the flange joint was tested on the MTS test frame to thoroughly investigate the integrity of a bolted flange assembly under different loading conditions by the proposed comprehensive integrity monitoring system. The characteristic variations of the flange connection under the tensile loads and combined tensile and internal pressure loads were both studied by the piezo-based active sensing method and electromechanical impedance measurement, respectively. In addition, the real-time FBG-enabled strain monitoring of bolts, internal pressure and AE acoustics enabled to determine the leakage failures of the flange connections subjected to the increasing tensile loads and internal pressure. Furthermore, a preliminary result of the leak-related tension limit was obtained under a variety of tightened torques on the bolts, which offered a useful leakage failure envelope to potentially mitigate the potential failures of the future use of flange connections in field.

Fourthly, considering the difficulty of accessing subsea pipelines by human divers, a touch-enabled bolt connection inspection approach was developed. An active sensing approach using PZT transducers mounted on a proof-of-concept clamping device that mimics two robotic fingers was designed and investigated for inspecting bolt connections. The clamping mechanism utilized magnets that help to secure a temporary and effective coupling between the transducers and the both surfaces of the bolt connection, such as a flange. Upon touching, one PZT transducer mounted on one end of clamping device generates stress waves that propagate across the connection interface, and the other PZT transducer mounted on the other end of the clamp detects the propagating stress wave. Experimental studies validated the potential of the proposed touch-based inspection approach for identifying the status of bolted connection under the different applied torques in air and in salt water in laboratory.

Finally, to advance the touch-based inspection method in undersea environment, an undersea ROV with robotic manipulator was leveraged to improve the touch-based inspection capacity of conducting a remote undersea inspection of subsea bolted connections. A robotic manipulator model was designed and fabricated. The fingertip of the manipulator was integrated with piezoceramic transducers, which was therefore assembled with an underwater ROV device to function as an undersea robotic inspection system. The undersea operation of the ROV and the robotic manipulator can be remotely controlled on land. A field test was conducted to evaluate the inspection performance of the proposed ROV-enable remote undersea inspection method. The undersea field test demonstrated a promising undersea inspection technique to effectively evaluate the integrity of the subsea bolted connections subjected to different toques.

## 1.3 Organization

This dissertation includes eight chapters. Chapter one introduces the background, motivation and objectives of this dissertation. The rest of the dissertation is organized as follows.

Chapter two provides the background of the bolted flange connections and the cutting edge monitoring technologies, including piezo-based active sensing method, electromechanical impedance measurements, FBG-enabled strain monitoring and acoustic emission leak detection system.

Chapter three investigates the characteristic changes over the bolted flange connection under the internal pressure loads using piezo-based impedance technique. Results reveal that a near-linear relationship between the resonant frequencies and the corresponding internal pressure

Chapter four describes the detection studies of the pressure-induced leakage on the bolted flange joint assembly by implementing acoustic emission system, pressure transducer, and FBG-enabled smart bolts. Results clearly illustrated that the strain changes over bots correlated with the internal pressure and that the pressure-induced leaks can be readily detected and identified by AE system.

Chapter five presents the proposed comprehensive integrity monitoring system of a bolted flange assembly under combined tensile loads and internal pressure. The characteristic variations of the flange connection under the tensile loads and combined tensile and internal pressure loads were both studied by the piezo-based active sensing method and electromechanical impedance measurement, respectively. In addition, the real-time FBG-enabled strain monitoring of bolts, internal pressure and AE acoustics enabled to determine the leakage failures of the flange connections.

Chapter six explores a new touch-based inspection mechanism using magnets that help to secure a temporary and effective coupling condition between the transducers and the bolted connections. Experimental studies validate the feasibility of the proposed touch-based inspection approach for evaluating the status of bolted connection under the different applied torques in air and in salt water in laboratory.

Chapter seven shows the further development of the touch-based inspection method with an undersea ROV and a sensing manipulator to perform subsea remote inspections for bolted structures. The undersea field tests demonstrate that the proposed ROV-enabled robotic inspection manipulator is capable of executing a remote touch-based inspection task for effectively evaluating the integrity of the bolted connections in a local marine environment.

Chapter eight concludes this dissertation and recommends future works.

# 2. Structural Integrity Monitoring Systems

## 2.1 Piezo-based Active Sensing Method

Piezoelectric materials generate electrical charges in response to mechanical stress in the direct manner. Conversely, a mechanical strain is produced when an electrical filed is applied to the piezoelectric materials [86]. Based on direct piezoelectric effect, piezoelectric materials can be used to detect dynamic responses as a sensor, while the converse effect can be worked as an actuator [87]. With the advantages of dual sensing and actuation, piezoceramic transducers, especially PZT (Lead Zirconate Titanate) transducers, have been widely explored for structural health monitoring applications [41, 59, 75].

In the active sensing tests, as demonstrated in Fig. 2-1, one PZT transducer, acting as an actuator, generates a stress wave that propagates across the bolted specimen as stress waves. The stress waves are received by the second transducer as a sensor.

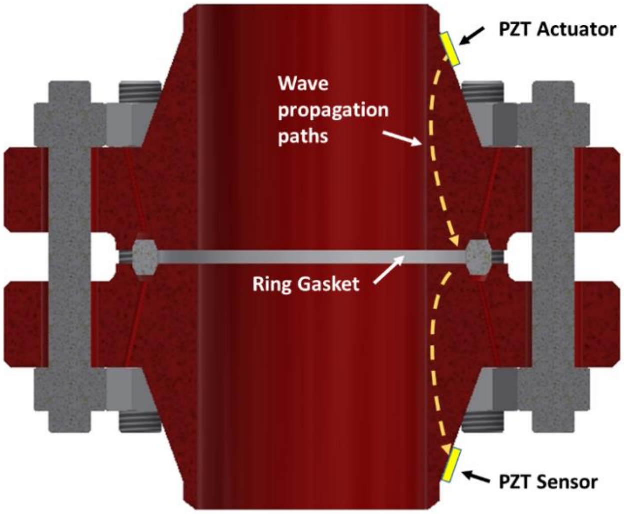

Figure 2-1 Demonstration of active sensing measurements

A linear swept-sine wave within a wide frequency range is actuated as a reference signal for the active sensing measurements. The function of the generated swept sine wave signal can be presented as [88]

$$y(t) = A\sin\left[\omega(t)\cdot t\right], \tag{2-1}$$

where $A$ is amplitude of the signal and $\omega(t)$ is the instantaneous frequency that can be expressed as

$$\omega(t) = \frac{1}{2}C\cdot t + 2\pi f_{start}, \tag{2-2}$$

where $f_{start}$ is the start frequency of the swept-sine wave; and $C$ is the rate of frequency change. Since the frequency of the swept-sine signal increases linearly with time, so it can be defined as

$$C = 2\pi\frac{f_{end} - f_{start}}{T}, \tag{2-3}$$

where $f_{end}$ is the end frequency of the swept-sine wave; $T$ is the time duration of the signal.

Therefore, the time-domain function of the swept sine wave, equation (2-1), can be thus derived as

$$y(t) = A\sin\left[2\pi(\frac{f_{end} - f_{start}}{2T}\cdot t^2 + f_{start}\cdot t)\right]. \tag{2-4}$$

The received signal strength and its corresponding signal energy correlates with the characteristics of the interface between the bolted specimens, such as contact stress, interface profile and true contact area. In other words, any alterations in the characteristics of bolted connection interface under tensile loads or/and internal pressure can induce measurable changes in the received signal. Therefore, the status of the bolted connection can be inferred by comparing the features of the received signals at any instant to the measured baseline of the received signal. The active sensing results are primarily studied in the ways of time-domain responses, spectrogram representation and wavelet packet-based energy, which will all be discussed in the following sections.

### 2.1.1 Spectrogram

The short-time Fourier transform (STFT) is used to analyze the spectrum of frequencies the received signal as the signal changes over time [89, 90]. STFT provides a visual representation for data analysis [91-93]. Generally, the original signal is split into short periods of time segments through multiplying by a window function, $h(t)$, and then separately performing the Fourier transform for each short-time segment [94]. The Fourier transform helps describe the distribution of frequency changes over the time, and is described as [95],

$$F_t(\omega) = \frac{1}{\sqrt{2\pi}} \int_{-\infty}^{+\infty} e^{-i\omega\tau} f(\tau) h(\tau - t) d\tau \, , \tag{2-5}$$

where $f(t)$ is the sensor signal to be transformed; $t$ is the time of interest and $\tau$ is the running time. Each time segment has its own spectrum. The combination of the spectra forms the time-frequency distribution, $P_{sp}(t,\omega)$, or the spectrogram, which can be written as [95],

$$P_{sp}(t,\omega) = \left|F_t(\omega)\right|^2 = \left|\frac{1}{\sqrt{2\pi}} \int_{-\infty}^{+\infty} e^{-i\omega\tau} f(\tau) h(\tau - t) d\tau\right|^2 . \tag{2-6}$$

Therefore, the spectral intensity along with the excitation time and frequency can be influenced by changes in bolt preload. In addition, with increasing torque applied on the bolted plates, the true contact area between bolted plates can be increased to assist the transmission of the stress wave across the interface, while spectral power around resonant frequencies between the transducer and the bolted structure become more dominant or visible in the spectrograms.

### 2.1.2 Wavelet Packet-based Energy

The wavelet packet transformation (WPT) provides a level-by-level wavelet decomposition [96]. During wavelet packet analysis, a signal is split into an approximation and a detail coefficient and both are further decomposed into the next level [96, 97]. Illustrated in Fig. 2-2 is an example of a three-level wavelet packet decomposition. This process utilizes a recursive filter-decimation operation. Moreover, the WPT performs a complete decomposition at each level to achieve a higher resolution in frequency region [98, 99]. Hence, the wavelet packet analysis provides a better way for signal analysis. In this study, considering the accuracy, precision and computational complexity, a 5-level wavelet packet decomposition was selected. A 5-level WPT produces a total of 32 sub-bands with each frequency band covering 1/32 of the entire signal spectrum [100]. The total signal energy of the acquired signal from active sensing approach can be obtained by the summation of the energy from 32 wavelet packet components. Hence, the WPT-based energy method offers an alternative way to quantitatively present the acquired signals, which can clearly distinguish the variations from the active sensing results.

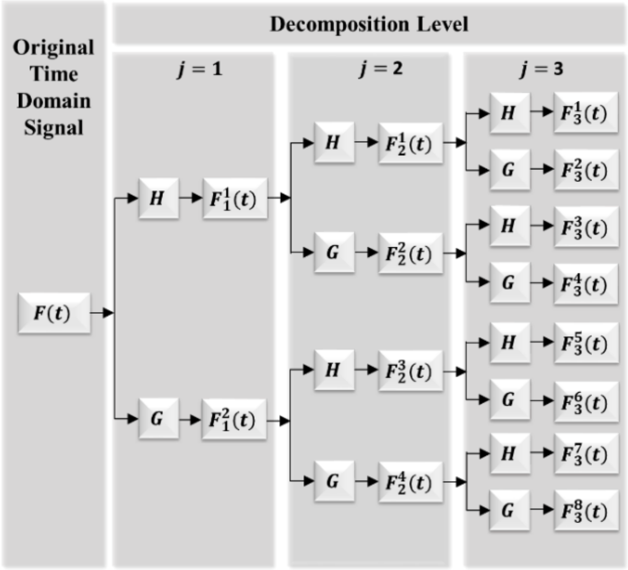

Figure 2-2 Illustration of a three-level wavelet packet decomposition

A wavelet packet $\psi_{j,k}^{i}(t)$ can be represented by [96, 97],

$$\psi_{j,k}^{i}(t) = 2^{-\frac{j}{2}} \psi^{i}\left(2^{-j} t - k\right), \tag{2-7}$$

where $i$ is modulation variable, $j$ is scale variable, and $k$ is translation variable. The first wavelet function is defined as the mother wavelet function as follows:

$$\psi^{1}(t) = \psi(t). \tag{2-8}$$

The wavelet function $\psi^{i}(t)$ can be derived by a recursive equation

$$\psi^{2i}(t) = \sqrt{2} \sum_{k=-\infty}^{+\infty} H(k) \psi^{i}(2t - k) \tag{2-9}$$

and

$$\psi^{2i+1}(t) = \sqrt{2} \sum_{k=-\infty}^{+\infty} G(k) \psi^{i}(2t - k), \tag{2-10}$$

where $H(k)$ and $G(k)$ are quadrature mirror filters. $H(k)$ is associated with the scaling function and $G(k)$ is associated with the mother wavelet function.

A time-domain signal, $F(t)$, can be decomposed into the $j$th level and be described as

$$F\left(t\right)=\sum_{i=0}^{2^{j}-1}F_{j}^{i}\left(t\right), \tag{2-11}$$

where $F_j^i$ is the $i$th order wavelet packet component signal at the $j$th level. Furthermore, $F_j^i$ can be structured by a linear combination of wavelet packet functions of $\psi_{j,k}^i(t)$.

$$F_{j}^{i}\left(t\right)=\sum_{k=-\infty}^{+\infty}C_{j,k}^{i}\left(t\right)\cdot\psi_{j,k}^{i}\left(t\right). \tag{2-12}$$

Here, $C_{j,k}^i(t)$ represents the wavelet packet coefficient, which can be described by

$$C_{j,k}^{i}\left(t\right)=\int_{-\infty}^{+\infty}F\left(t\right)\cdot\psi_{j,k}^{i}\left(t\right)dt. \tag{2-13}$$

The energy $E_j$ of the signal $F(t)$ at the $j$th level is defined as

$$E_{j}=\int_{-\infty}^{+\infty}F^{2}\left(t\right)dt=\sum_{m=0}^{2^{j}-1}\sum_{n=0}^{2^{j}-1}\int_{-\infty}^{+\infty}F_{j}^{m}\left(t\right)\cdot F_{i}^{n}\left(t\right)dt\ . \tag{2-14}$$

Since the wavelet functions are orthogonal, $\psi_{j,k}^{m}\left(t\right)\cdot\psi_{j,k}^{n}\left(t\right)=0,\left(m\neq n\right)$, and by substituting equation (2-14), we obtain

$$E_{j}=\sum_{i=0}^{2^{j}-1}E_{j}^{i}=\sum_{i=0}^{2^{j}-1}\int_{-\infty}^{+\infty}\left[F_{j}^{i}\left(t\right)\right]^{2}dt\ , \tag{2-15}$$

where $E_j^i$ is the component energy stored in the $i$th order of wavelet packet component signal at the $j$th level. $E_j^i$ is described by

$$E_j^i = \int_{-\infty}^{+\infty} \left[ F_j^i \left( t \right) \right]^2 dt \, . \tag{2-16}$$

Thus, the component energy $E_j^i$ is stored in a frequency band determined by the wavelet function $\psi_{j,k}^i(t)$. Furthermore, the total signal energy stored in the original signal can be decomposed into a superposition of wavelet packet component energies over different frequency bands [101].

## 2.2 Electromechanical Impedance (EMI)

Electromechanical impedance-based method has been developed to be one of promising nondestructive testing (NDT) techniques [51, 52], which has been wildly used to monitor structural integrity in mechanical and civil structures [53-55], including the bolted connection monitoring [56-58]. The impedance-based measurements take the advantages of the direct and converse piezoelectric effects of the transducer, which ensures the PZT patch simultaneously function as an actuator and sensor through an impedance analyzer system [59]. Through the surface-bonded between the piezoceramic patch and the monitored specimen, the electrical impedance signature of the piezoceramic path is straightforwardly correlated to the mechanical properties of the host structure, especially for the local area where the piezoceramic patch was mounted [60]. Therefore, any damages or characteristics changes in the host structure can be directly reflected on the electromechanical impedance signatures [61].

When the PZT patch is bonded to the host structure that is assumed as a single-degree-of-freedom (DOF) mass-spring system and the expression for the electro-mechanical admittance (reciprocal of electrical impedance of the PZT) can be described as [102]

$$\bar{Y} = G + Bi = i\omega \frac{wl}{t}[\bar{\varepsilon}_{33}^{T} - \mathrm{d}_{31}^{2}\bar{\mathrm{Y}}_{11}^{E} + (\frac{Z_{Str}}{Z_{PZT} + Z_{Str}})\,\mathrm{d}_{31}^{2}\bar{\mathrm{Y}}_{11}^{E}(\frac{\tan kl}{kl})], \tag{2-17}$$

where $w$, $l$ and $t$ is width, length and thickness of the PZT patch, respectively; $\mathrm{d}_{31}$ is the piezoelectric strain coefficient; $\bar{\varepsilon}_{33}^{T}$ is the complex electric permittivity of the PZT patch at the constant stress; $\bar{\mathrm{Y}}_{11}^{E}$ is the complex Young's modulus of the PZT patch at the constant field; $Z_{Str}$ and $Z_{PZT}$ respectively describes the mechanical impedance of the host structure and the PZT patch.

As can be seen from the equation, the electrical impedance is directly related to the mechanical impedance of the PZT patch and the bonded structure. Typically, the variation in mechanical property of the PZT patch is considered to be infinitesimally small as compared to the host structure. Therefore, any variations in the mechanical impedance of the host structure, such as stiffness or mass, change the PZT's electrical impedance-related signatures. For the electromechanical admittance, the real part is conductance (G) and imaginary part is susceptance (B). The imaginary part is more sensitive to the temperature because of the dielectric constant of the PZT patch. Thus, the real part, conductance (G), is primarily measured and used during the piezo-based impedance monitoring tests in the proposed research.

## 2.3 Acoustic Emission Leak Detection System

Acoustic emission (AE) technique is one of the most promising nondestructive evaluation methods that have been considerably applied to a broad variety of materials [62] and structures [63], including bridges monitoring [64-67], fatigue cracks [68, 69], and especially for leak detection of pipelines and pressure vessels [70-73]. AE describes a phenomenon of transient elastic stress waves that generated by a rapid release of energy from a localized source in a structure subjected to a sudden change of pressure, load or temperature. The waves propagate through the structure, and are then detected and converted to electrical voltage signals by an AE sensor that is directly mounted on the surface, as shown in Fig. 2-3. An AE sensor is primarily a piezoelectric transducer encapsulated in a protective housing, and an AE sensor can cover a wide frequency range of 1 kHz to 1 MHz depending on the nature of the sources.

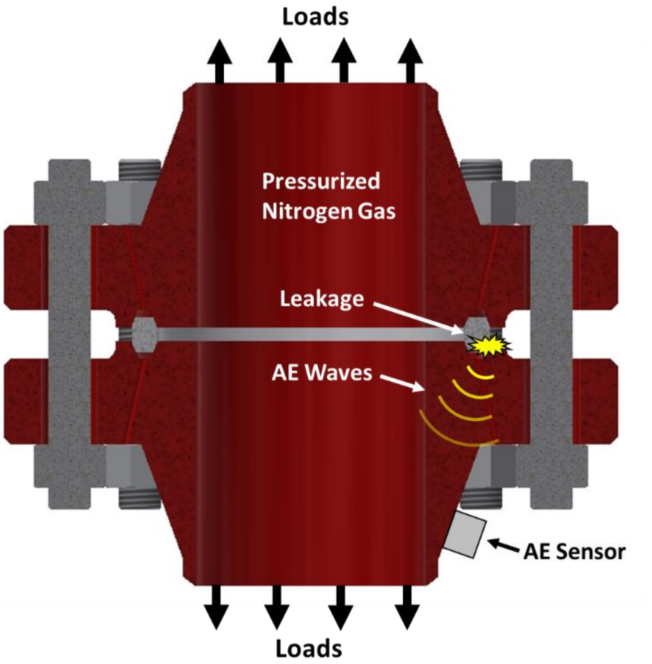

Figure 2-3 Demonstration of AE detection measurement

Detection and analysis of the AE signals can offer useful information to interpret the material behaviors or the structural integrity under real-time loading conditions. The AE signal features mainly include, hit, count, event, amplitude, rise time and energy [63]. The detailed illustration of each parameter is listed in Fig. 2-4.

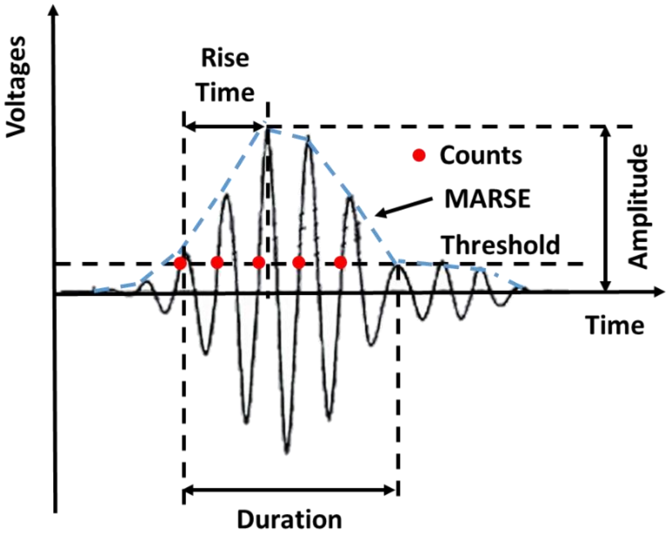

Figure 2-4 Illustration of parameters within an AE signal

AE hit, defined as the signal over the certain threshold, is the one of the most frequently used term. Amplitude is the peak value of the measured AE waveform and the unit is dB. Rise time describes the time interval between the first crossing against threshold and the peak amplitude. Duration time is the time interval between the first and the last crossing against the threshold. Counts define the number of peaks which are greater the threshold. MARSE is the measured area under the rectified signal envelop. Energy is the integral of squared amplitude over time of signal duration. In the proposed research, the acoustics generated by the sudden release of the escaping pressurized nitrogen gas are identified by the AE signal features of hits and energy.

## 2.4 FBG-enabled Bolt Strain Monitoring

Fiber Bragg grating (FBG) sensors are wavelength modulated fiber optic devices, the wavelength changes are produced by inscribing periodic variations in the refractive index of the core of the fiber optic cable [103]. With the outstanding advantages of lightweight, small physical size, high-resolution, immunity to electromagnetic interference, ability to be multiplexed [104], FBG sensors exhibit a great potential for structural health monitoring applications, including real-time monitoring of bridge-like structures [105-107], vibration and leakage measurements in pipelines [108, 109], relative humidity detection [110-112], and strain monitoring in steel rock bolts [113-115].

The dominant reflected wavelength, the Bragg wavelength, is defined by

$$\lambda_B = 2n_{eff}\Lambda\,, \tag{2-18}$$

where $\lambda_b$ is the Braff wavelength; $n_{eff}$ is the effective refractive index of the grating in the fiber core; and $\Lambda$ is the grating period, as shown in Fig. 2-5.

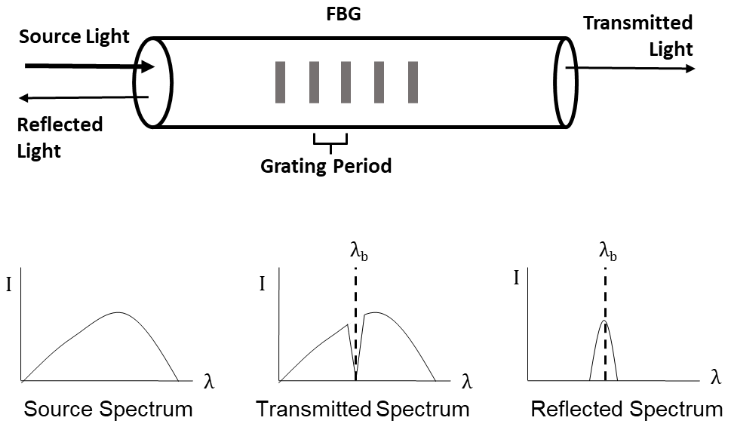

Figure 2-5 Principle of FBG sensors

The Bragg wavelength of reflected light can be changed by the external factors from temperature, strain, and pressure. A linear relationship can be presented as [104]

$$\frac{\Delta\lambda_B}{\lambda_B} = \alpha_T \Delta T + \alpha_\varepsilon \Delta\varepsilon + \alpha_P \Delta P \,, \tag{2-19}$$

where $\alpha_T$ , $\alpha_\varepsilon$ and $\alpha_P$ are coefficients of temperature, strain, and pressure, respectively.

In this proposed research, an FBG sensor (OD: ~250 μm) is installed via a tiny through hole (ID: ~1mm) along the length of a bolt with epoxy. The dominant wavelengths of four sets of FBG sensors are 1552 nm, 1561 nm, 1570 nm and 1576 nm. The detected resolution of the optical wavelengths is approximately 1 pm and the calibrated wavelength accuracy is about ±10 pm using an interrogator (Micron Optics sm 130) at a sampling frequency of 8 Hz. Therefore, FBG-enabled bolts can be used to directly and accurately measure the real-time strain changes along the bolts when the flange assemble subjected to the different loads, as shown in Fig. 2-6.

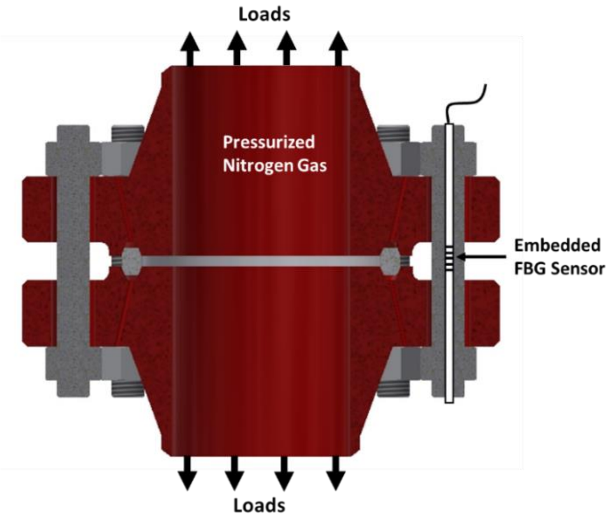

Figure 2-6 Demonstration of the FBG-enabled bolts strain monitoring

# 3. Monitoring of Bolted Flange Connections Using Electromechanical Impedance (EMI) Method

## 3.1 Introduction

Metal-to-metal seals have been commonly utilized in the bolted flange connections for linking the pressure vessels and piping system. Through tightening the bolts, the generated axial load compresses the mating surface of the ring gasket against the flange grooves and thus initializes a metal-to-metal seal of the flange connections to contain the internal contents under pressure. The ring-type gasket is one of the key components of the bolted flange joints for providing a seal and preventing leakage failures. The integrity of the ring gasket primarily consequently determines the sealing performance of the bolted flange joints.

Electromechanical impedance-based method has been developed to be one of promising nondestructive testing (NDT) techniques [51, 52], and has been wildly used to monitor structural integrity in mechanical and civil structures [53-55], including the bolted connection monitoring [56-58]. The impedance-based measurements take the advantages of the direct and converse piezoelectric effects of the transducer, which ensures the PZT patch simultaneously function as an actuator and a sensor through an impedance analyzer [59]. When a piezoceramic patch is bonded on a host structure, the electrical impedance signature of the PZT path is correlated to the mechanical impedance of the host structure, especially for the local area where the piezoceramic patch is mounted [60]. Therefore, damages or characteristics changes in the host structure can be directly reflected on the electromechanical impedance signatures [61].

In this study, the objective is to monitor the real-time characteristic changes in the bolted flange connection under the internal pressure loadings, including both pressurization and depressurization process. Since the ring gasket possesses a dominant effect on the sealing performance of the flange connection which typically represents a point of vulnerability that can induce leakages. Moreover, the internal pressure can generate end cap forces on the bolted flange assembly which can immediately change the axil force on the bolts, thereby influencing the compressive loads on the ring gasket. In other words, the ring gasket is highly sensitive to the internal pressure loadings. Therefore, in this study, one piezoceramic patch is directly bonded on the outer surface of the ring gasket to acquire its conductance signatures during the pressurization and depressurization process. Furthermore, a repeatability study is also conducted and summarized to verify the effectiveness of the proposed electromechanical impedance method in monitoring the pressure-induced variation on the bolted flange joints.

## 3.2 Experimental Setup and Procedures

The experimental setup is shown in the Fig. 3-1. One PZT patch is mounted on the outer surface of the ring gasket around the gap between two flange components, as shown in the zoomed-in view. The PZT patch is connected with an impedance analyzer system (Agilent 4294A) for measuring the impedance signatures. Among several impedance parameters, the electrical admittance is an inverse of the electrical impedance of the PZT transducer which coupled with the mechanical properties of the host structure. Since the imaginary part of the admittance is sensitive to the temperature variation due to the effect of dielectric constant of PZT patch, the real part of the admittance, conductance G, is selected as a key parameter to present the structural integrity.

The bolted flange assembly was connected with a pressurized nitrogen gas cylinder through a steel tubing and related fittings. The chamber of the bolted flange assembly was pressurized by injecting the nitrogen gas from 0 psi to 1000 psi with each increment of 200 psi. The real-time internal pressure can be checked by a pressure gauge. The internal pressure was record by the pressure transducer at a sampling frequency of 10 Hz. The depressurization process was conducted by adjusting the relief valve and releasing the nitrogen gas. During the each case, the conductance signatures from the PZT patch bonded with the ring gasket were acquired through a frequency range from 60 kHz to 240 kHz under a step of 225 Hz. The internal pressure induced variations in characteristics of the ring gasket concerning the sealing performance could be evaluated by analyzing the conductance signatures. Moreover, the measurements included pressurization and depressurization process, which was separately repeated three times as a repeatability study for result verification.

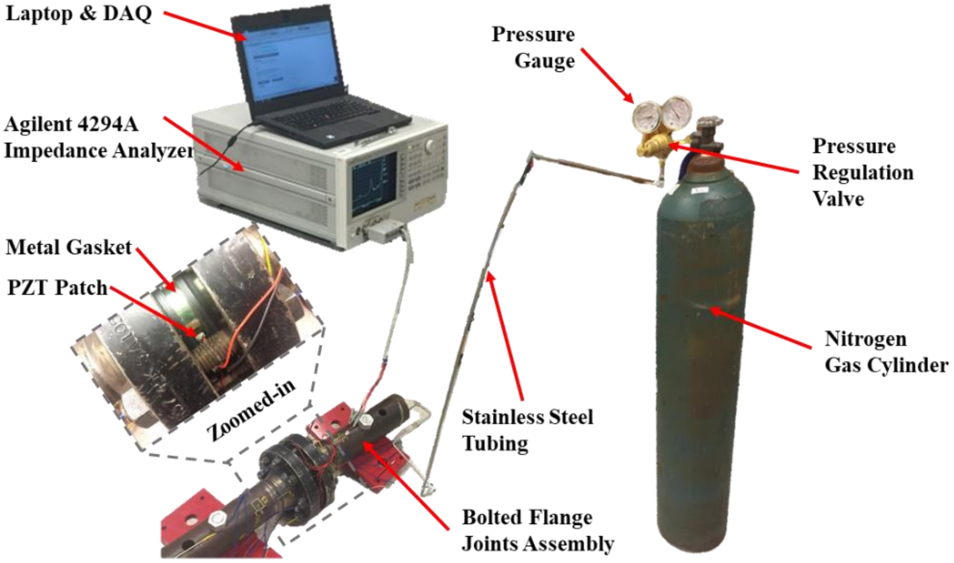

Figure 3-1 Experimental setup of the bolted flange joint using EMI technique

## 3.3 Results and Discussions

### 3.3.1 Results of Pressurization Process

The conductance signatures were acquired by the impedance analyzer from 60 kHz to 240 kHz to cover the responses over the two peak frequencies. The number of sweep points were 801 points for each measurement. As shown in Fig. 3-2, the raw data of the conductance signatures was recorded from the PZT patch bonded on the ring gasket corresponding to the different internal pressures from 0 psi to 1000 psi through injecting the nitrogen gas. A moving average filter with every 10 consecutive points was implemented to smooth the signals, as shown in Fig. 3-3. Two distinct peaks in frequency domain are observed, and are directly related to the certain resonant modes of the PZT patch bonded with the ring gasket. To better analyze the variations in conductance signatures, the selected distinct peaks are zoomed in two separated graphs.

For the first peak in Fig. 3-4, when the internal pressure was 0 psi, the peak frequency is around 119.30 kHz, however, it decreases to be about 112.40 kHz once the internal pressure increases to 1000 psi. A similar trend is also observed in the second peak, as shown in Fig. 3-5. The resonant frequency decreases from 181.80 kHz to 179.30 kHz while the internal pressure increases from 0 psi to 1000 psi. Overall, an obvious leftward shift of the peak responses is observed, which indicates that the peak frequency decreases during the pressurization process of the bolted flange joint. During the pressurization process, the increasing internal pressure induces a higher end cap stress acting on the flange components, which attempts to separate the bolted flange assembly as a result of relaxing the compressive stress on the ring gasket. The stress relaxation reduces the stiffness of the ring gasket and causes a leftward shift of the peak frequencies.

The frequencies of two selected peaks from three separately repeated measurements are summarized in Table 3-1 and Table 3-2, respectively. Results reveal a near-linear relationship between the peak frequencies and the internal pressure, as plotted in Fig. 3-6. In addition, both the equations and R-squared values of the linear trend-line for the two peaks are respectively presented. The comparison of the fitted linear trend-lines of two resonant frequencies illustrates that the first peak possessed a relatively larger change rate than the second peak due to the same effects of the pressurization process. The standard deviation results also indicate that the first peak is more sensitive to the pressure-induced changes on the ring gasket as a result of a higher standard deviation value than the second peak. Furthermore, the conductance of the second peak exhibits a more obviously growing trend than the first peak.

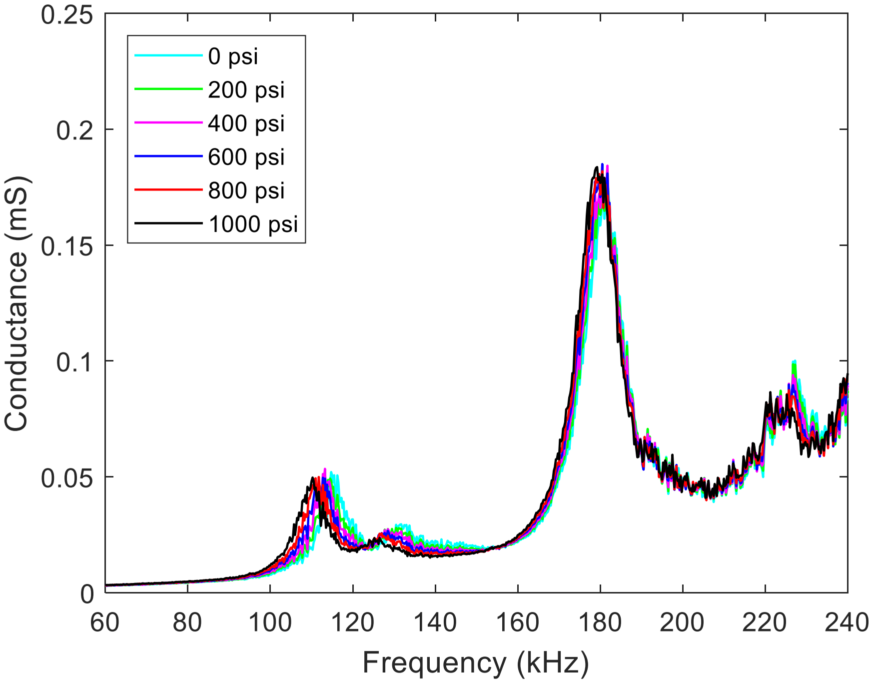

Figure 3-2 Raw date of the conductance signatures during pressurization process

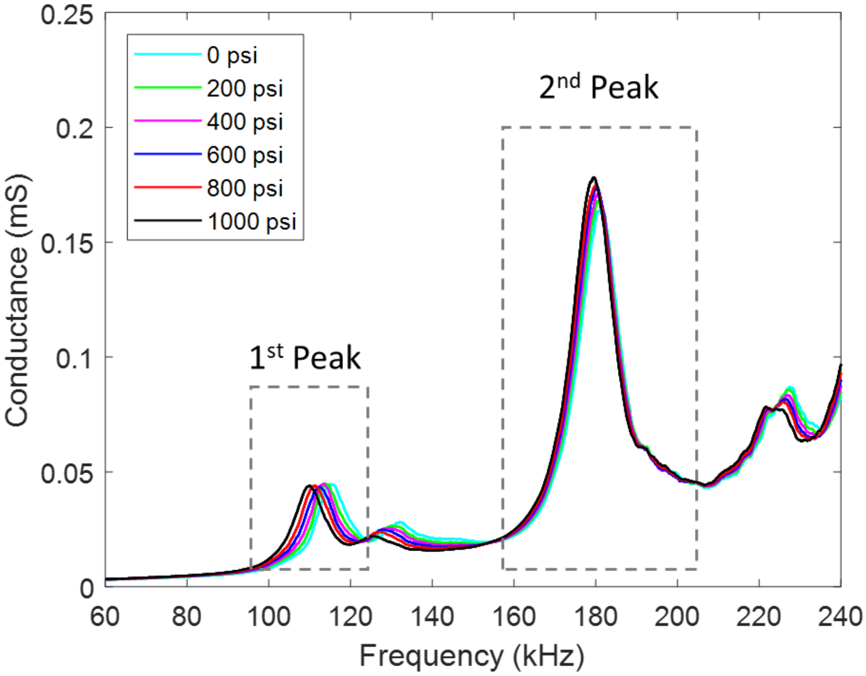

Figure 3-3 Processed date of the conductance signatures during pressurization process

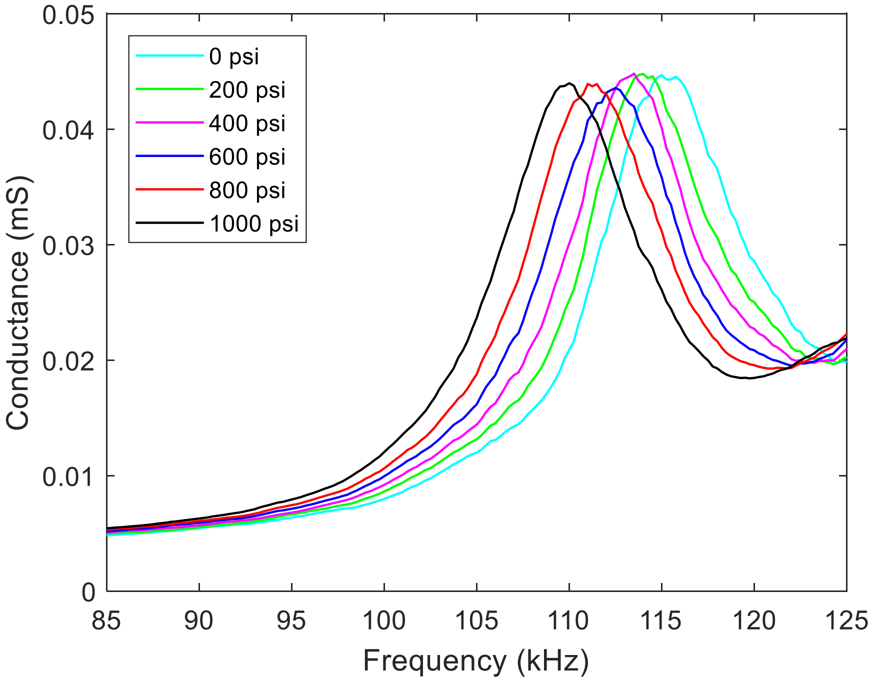

Figure 3-4 Zoomed-in view of the conductance signatures around the first peak frequency during pressurization process

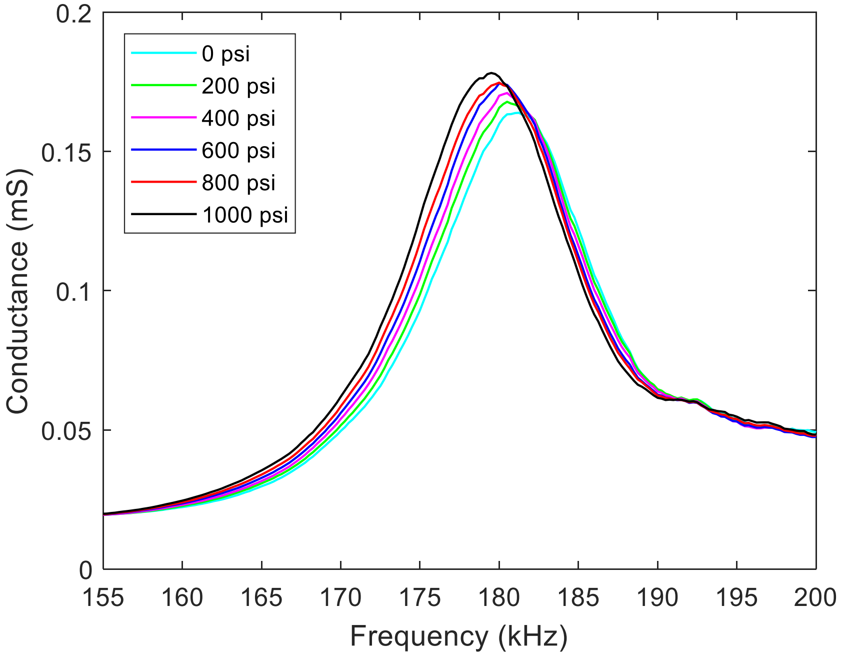

Figure 3-5 Zoomed-in view of the conductance signatures around the second peak frequency during pressurization process

Table 3-1 Summary of the first peak frequencies during pressurization process

| **No.** | **Pressure (psi)** | **1st Peak Frequency (kHz)** | | | | **Standard Deviation** |
|---|---|---|---|---|---|---|
| | | **Test-1** | **Test-2** | **Test-3** | **Average** | |
| 1 | 0 | 119.30 | 118.30 | 118.00 | 118.53 | 0.68 |
| 2 | 200 | 118.50 | 117.50 | 117.00 | 117.67 | 0.76 |
| 3 | 400 | 117.30 | 116.50 | 116.00 | 116.60 | 0.66 |
| 4 | 600 | 116.30 | 115.50 | 115.00 | 115.60 | 0.66 |
| 5 | 800 | 114.50 | 114.50 | 114.00 | 114.33 | 0.29 |
| 6 | 1000 | 112.50 | 112.50 | 112.30 | 112.43 | 0.12 |

Table 3-2 Summary of the second peak frequencies during pressurization process

| **No.** | **Pressure (psi)** | **2nd Peak Frequency (kHz)** | | | | **Standard Deviation** |
|---|---|---|---|---|---|---|
| | | **Test-1** | **Test-2** | **Test-3** | **Average** | |
| 1 | 0 | 181.80 | 181.50 | 181.50 | 181.60 | 0.17 |
| 2 | 200 | 181.30 | 181.00 | 181.00 | 181.10 | 0.17 |
| 3 | 400 | 181.00 | 180.80 | 180.50 | 180.77 | 0.25 |
| 4 | 600 | 180.50 | 180.30 | 180.30 | 180.37 | 0.12 |
| 5 | 800 | 180.00 | 179.80 | 179.80 | 179.87 | 0.12 |
| 6 | 1000 | 179.30 | 179.30 | 179.50 | 179.37 | 0.12 |

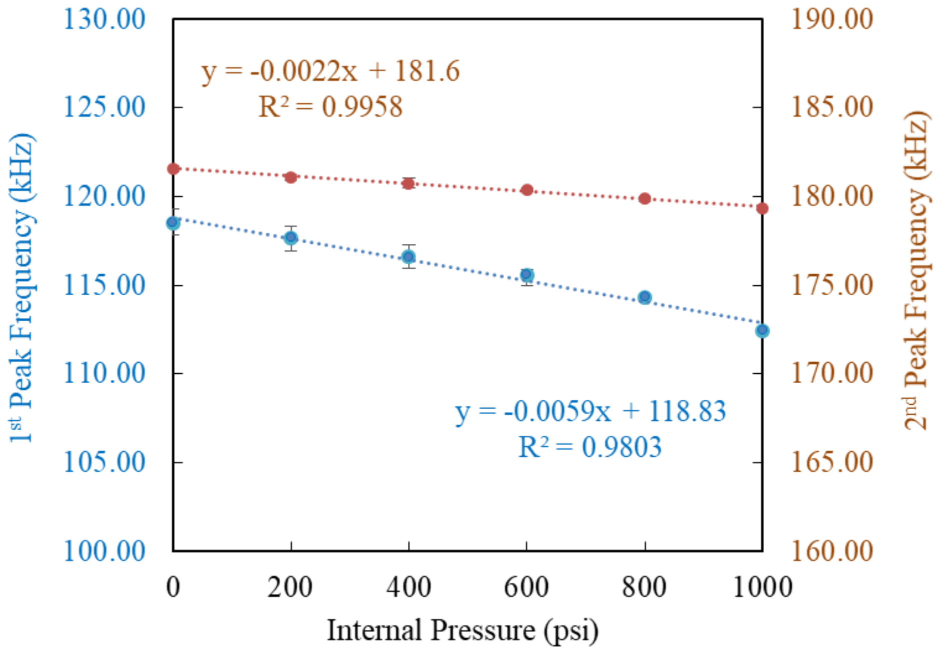

Figure 3-6 Relationship of the peak frequencies and the increasing internal pressure

### 3.3.2 Results of Depressurization Process

To investigate the effects of the depressurization process on the ring gasket, which were conducted through adjusting the relief valve to change the internal pressure of the bolted flange assembly from 1000 psi to 0 psi with a pressure interval of 200 psi. Under each step, the conductance signatures from the same PZT bonded on the ring gasket were acquired. The raw date, as shown in Fig. 3-7, was processed by a moving average filter in Fig. 3-8. Two of the same peaks were selected and zoomed into the different plots for a better data analysis of the results. As plotted in Fig. 3-9, when the internal pressure of the bolted flange assembly is successively decreased, a clear rightward shift of the first peak frequency becomes emerged. The similar behavior is also observed in the results around the second peak, as shown in Fig. 3-10. The decreasing internal pressure of the bolted flange assembly through releasing the nitrogen gas resumed the previous compressive loads acting on the ring gasket from the tightened bolts and consequently strengthened the stiffness of the ring gasket. The higher stiffness causes an increase in the peak frequencies corresponding to the decreasing internal pressure.

The summaries of the first and second frequency values during the depressurization process from a repeatability study are listed in Table 3-3 and Table 3-4, and plotted in Fig. 3-11, respectively. Similarly, a near-linear relationship between the resonant frequencies and the corresponding internal pressure is obtained. The associated equations and R-squared values are also presented in the curves. Compared the responses of the two peak frequencies during the depressurization process, the signatures around the lower resonant frequency are more sensitive in frequency shift, while the conductance signatures change are more obvious around the higher resonant frequency. Furthermore, when the internal pressurized nitrogen gas was completely released, the averaged first and second peak frequencies resumed to be 117.93 kHz and 181.37 kHz, respectively. As compared with results during the pressurization process in the last section, the initial peak frequencies were 118.53 kHz and 181.60 kHz without internal pressure. The minor difference in each peak frequency was within the standard deviation values from the repeatability study. Thus, a good agreement in results between the pressurization and depressurization process verifies the effectiveness of the proposed piezo-based impedance method in monitoring the real-time characteristic variations on the ring gasket caused by the internal pressure loads.

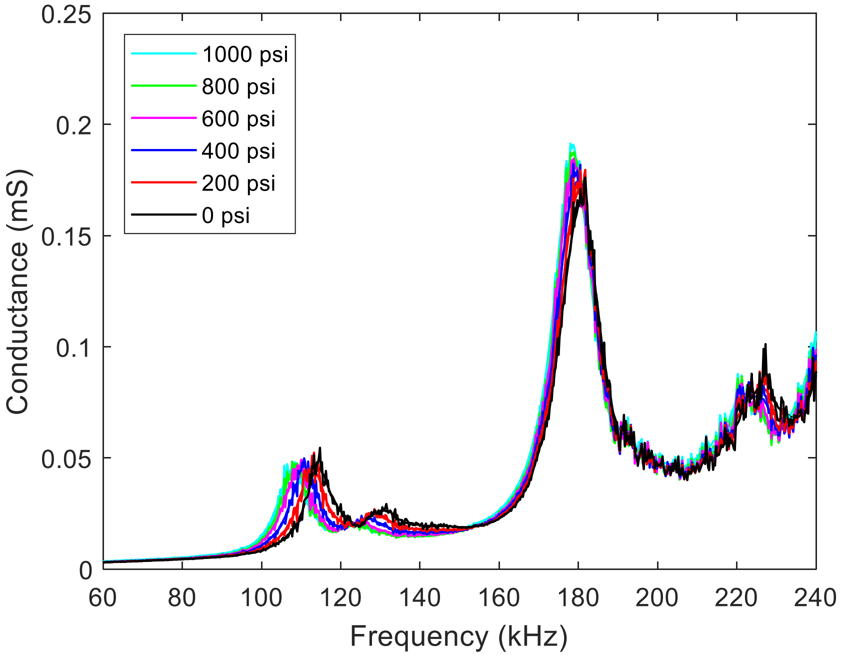

Figure 3-7 Raw date of the conductance signatures during depressurization process

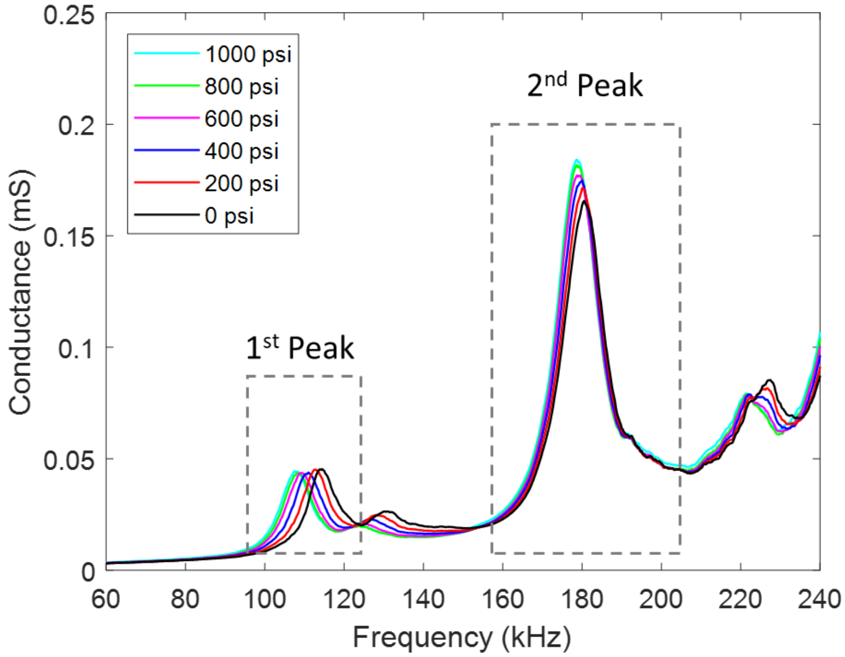

Figure 3-8 Processed date of the conductance signatures during depressurization process

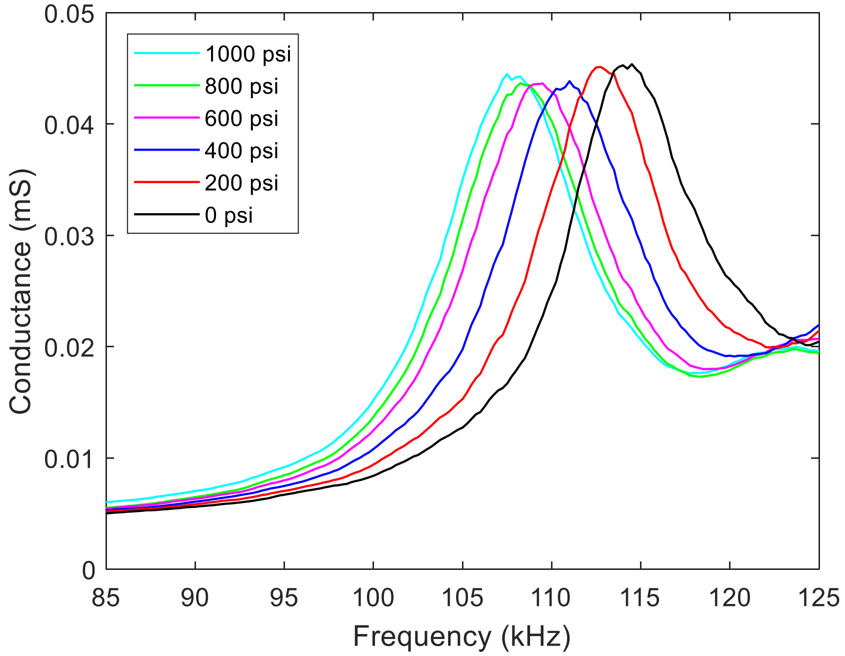

Figure 3-9 Zoomed-in view of the conductance signatures around the first peak frequency during the depressurization process

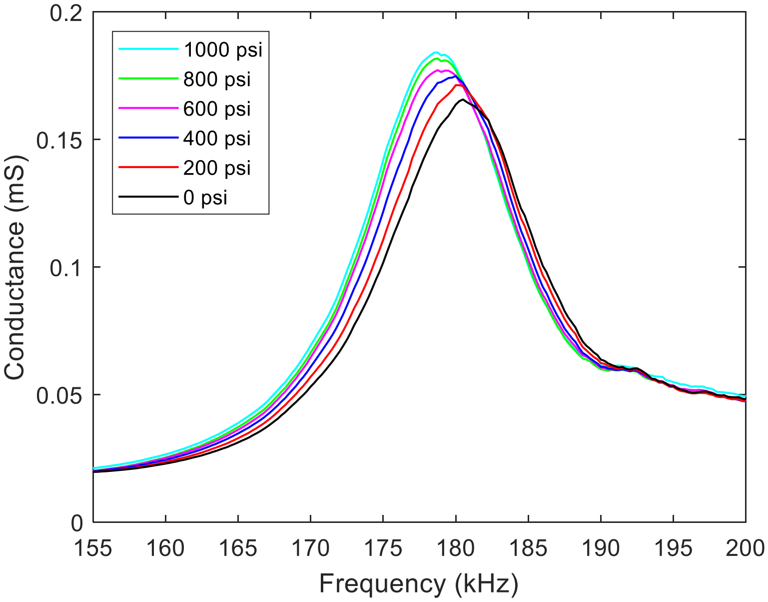

Figure 3-10 Zoomed-in view of the conductance signatures around the second peak frequency during the depressurization process

Table 3-3 Summary of the first peak frequencies during the depressurization process

| **No.** | **Pressure (psi)** | **1st Peak Frequency (kHz)** | | | | **Standard Deviation** |
|---|---|---|---|---|---|---|
| | | **Test-1** | **Test-2** | **Test-3** | **Average** | |
| 1 | 1000 | 112.50 | 112.50 | 112.30 | 112.43 | 0.12 |
| 2 | 800 | 113.50 | 113.30 | 113.00 | 113.27 | 0.25 |
| 3 | 600 | 114.30 | 114.00 | 113.80 | 114.03 | 0.25 |
| 4 | 400 | 115.50 | 115.00 | 114.50 | 115.00 | 0.50 |
| 5 | 200 | 116.80 | 116.80 | 116.00 | 116.53 | 0.46 |
| 6 | 0 | 118.00 | 118.00 | 117.80 | 117.93 | 0.12 |

Table 3-4 Summary of the second peak frequencies during the depressurization process

| **No.** | **Pressure (psi)** | **2nd Peak Frequency (kHz)** | | | | **Standard Deviation** |
|---|---|---|---|---|---|---|
| | | **Test-1** | **Test-2** | **Test-3** | **Average** | |
| 1 | 1000 | 179.30 | 179.50 | 179.50 | 179.43 | 0.12 |
| 2 | 800 | 179.80 | 180.00 | 180.00 | 179.93 | 0.12 |
| 3 | 600 | 180.10 | 180.30 | 180.20 | 180.20 | 0.10 |
| 4 | 400 | 180.50 | 180.80 | 180.50 | 180.60 | 0.17 |
| 5 | 200 | 181.00 | 181.00 | 180.80 | 180.93 | 0.12 |
| 6 | 0 | 181.80 | 181.30 | 181.00 | 181.37 | 0.40 |

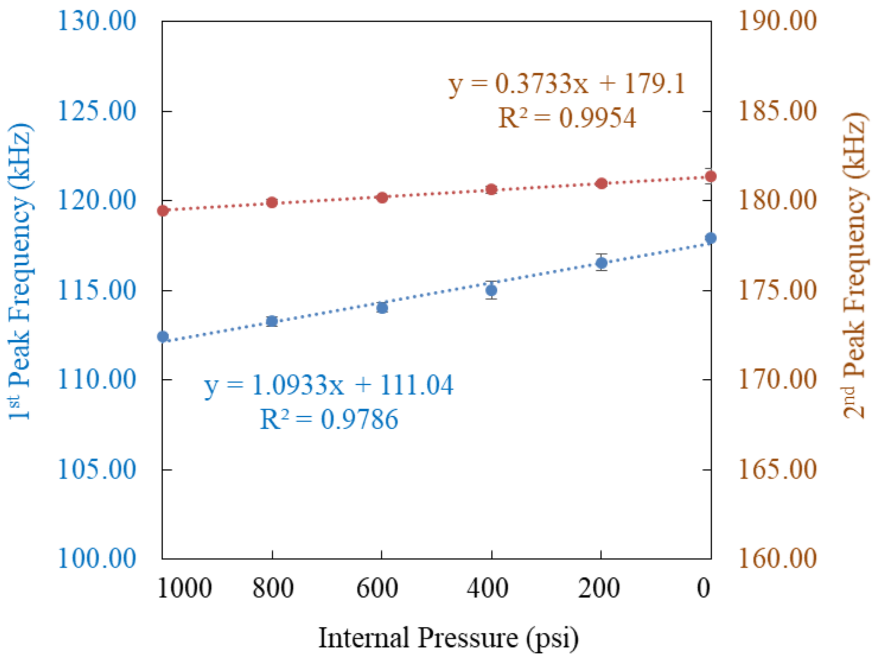

Figure 3-11 Relationship of the peak frequencies and the decreasing internal pressure

## 3.4 Summary

The ring gasket is one of the most important components for initializing a metal-to-metal seal of the bolted flange joints. In this study, the piezo-based electromechanical impedance technique was proposed and validated to monitoring the variations in characteristics of flange connection due to the different internal pressures loads. One PZT patch was directly bonded on the outer surface of the ring gasket to directly measure the electrical impedance to reflect variations in characteristics of flange connection. The experimental studies included both the pressurization process (from 0 psi to 1000 psi) and depressurization process (1000psi to 0 psi). The conductance signatures was acquired at a frequency range of 60 kHz to 240 kHz, which covered two modal frequencies. The changes of the internal pressure induced variations in characteristics of the flange connection were identified by analyzing the conductance signatures. Both the first and second peaks exhibited a leftward shift along a near-linear relationship with the internal pressure during the pressurization process, while this trend of each corresponding case was linearly resumed to the initial frequency, during the depressurization process, within the standard deviation values based on a repeatability study from three separate measurements. Therefore, a good agreement in results between the pressurization and depressurization process demonstrates that the proposed piezo-based impedance method is reliable to identify the pressure-induced variations on the ring gasket and thus offers a useful real-time measurement to evaluate the integrity of the flange connection under the pressure loads.

# 4. Leak Detection of Bolted Flange Joint under Internal Pressure Conditions

## 4.1 Introduction

Bolted flange joints are widely used in many engineering applications. Numerous onshore or offshore components in oil and gas industry, including pipeline systems, are connected through bolted flanges joints. The sealing conditions provided by the flange joints keep the systems intact and prevent disastrous leaking of pipe contents. However, each bolted connection actually represents a point of vulnerability that can suffer from leakages due to unpredictable loads, corrosion and erosion issues. Leakage can be more disastrous to environment in subsea applications. Therefore, one of the most pressing issues is the integrity of bolted flanges joints since the prevalent usage of bolted connections in practical engineering applications. Furthermore, to reduce these leak-induced issues, an effective and convenient monitoring system for leak detection of bolted flange joints becomes necessary.

In this chapter, leak detection was primarily investigated on the bolted flange joint using acoustic emission (AE) technique. The objective was to verify the effectiveness of the AE detection system in identifying the gas leak around the ring gasket. The leaks were induced by pressurizing the chamber of the bolted flange joint in the way of continuously injecting the nitrogen gas. The pressurized gas expanded the bolted flange as a result of relaxing the pre-stress on the gasket until connection seal failure. The adequate internal pressure for causing a leak around the ring gasket of the bolted flange joint primarily depended on the torque values applied on the bolts.

Considering the safety in laboratory, a relatively small torque value was applied on the bolts to forming an initial metal-to-metal seal condition over the ring gasket. This small torque ensured that the leak-requested pressure was acceptable and safe. During the experiments, the FBG-enabled bolts were installed on the flange joint to record the strain changes during the pressurization process. Meanwhile, the internal pressure of the bolted flange joint was recorded by a pressure transducer. Through data analysis, the pressure-induced leak from the ring gasket was clearly identified by acoustic signal features of AE hits and AE energy. Furthermore, the leak-related pressure value was also determined based on pressure signals, which offered valuable information for the comprehensive investigations of the bolted flange connections on the MTS test frame in Chapter 5.

## 4.2 Experimental Setup and Procedures

Two pieces of flange were assembled by eight sets of FBG-enabled bolts which were capable of monitoring the strain of the bolts using a Micron Optics sm 130 interrogator with a sampling frequency of 8 Hz. One acoustic emission (AE) transducer was bonded on the outer surface of the flange joint to capture the leakage induced AE signals through using Micro-II digital AE system. In addition, one pressure gauge was installed to directly show the inner pressure of the flange joint. Meanwhile, one pressure transducer was installed to simultaneously record the pressure signal through utilizing a signal conditioner, an N-I data acquisition board and a laptop with the LabVIEW-enabled application software.

The eight set of bolts were tightened by a torque of 15 ft-lb to initiate a metal-to-metal seal between the ring gasket and flange joint. This small torque value was applied on the bolts to ensure a possible leakage under an acceptable pressure in laboratory. The chamber of the flange joint was pressurized by injecting nitrogen gas until occurring leaks. The testing procedure includes three steps: pressurization, pressure-hold, and termination of pressurization. First of all, the internal pressure of the flange joint was gradually increased by a nitrogen gas cylinder. The maximum capacity of the nitrogen gas cylinder is 3500 psi. The increasing internal pressure of the chamber expanded the bolted flange joint and reduced the pre-stress on the ring gasket, thereby weakening the metal-to-metal sealing condition until a leak under a certain pressure. Once a pressure-induced leak occurred, the pressure was maintained for around 100 seconds under a constant gas injection rate. After that, the injection of the nitrogen gas cylinder was completely terminated. During this entire testing process, the signals of FBG sensors on bolts, internal pressure of chamber, and acoustic emission signals were simultaneously acquired by data acquisition systems, as shown in Fig. 4-1 and Fig. 4-2.

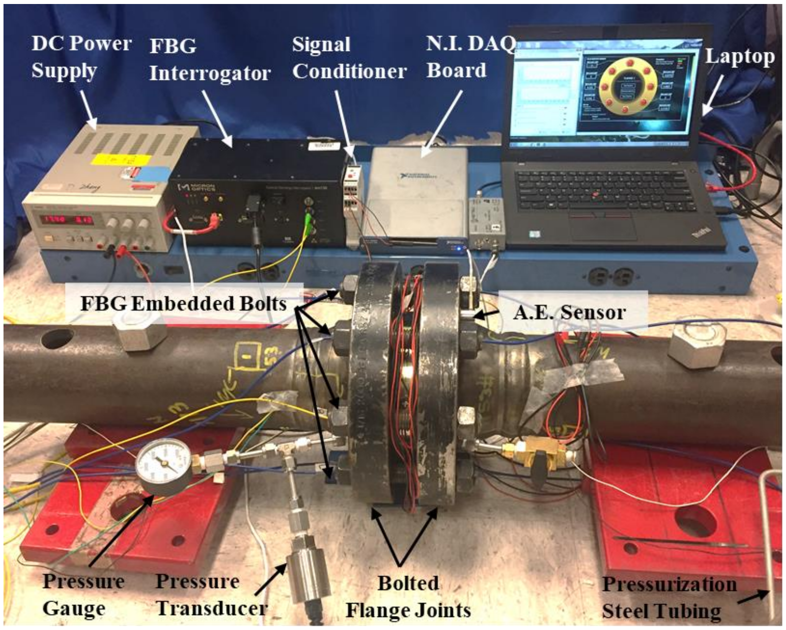

Figure 4-1 Experimental Setup and data acquisition system of leak detection investigation on the bolted flange assembly

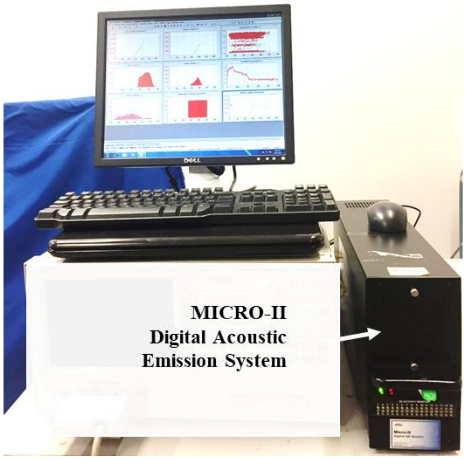

Figure 4-2 Micro-II digital acoustic emission data acquisition system

## 4.3 Results and Discussions

### 4.3.1 Results of FBG-enabled Strain Monitoring

Four sets of FBG-enabled bolts, as shown in red color in Fig. 4-3, were selected to represent the FBG signals over the bolts in four directions during the pressurization process. As shown from Fig. 4-4 to Fig. 4-7, the relationship between internal pressure and FBG wavelength over bolt # 1, #3, #5, and #7 was plotted, respectively. It clearly shows that wavelength changes of the FBG sensors correlated with the increasing internal pressure over the entire testing process. For the first step for pressurization, the wavelength of the fiber optic sensors was increased which indicated the bolts were elongated due to the increasing internal pressure. And when the internal pressure was maintained at the second step, the wavelengths of the fiber optic sensor were also constant. It is clear that the tension over four bolts were consistent under a pressure-hold status. In the final step, the wavelengths of the fiber optic sensors or the tension over the four bolted decreased with the internal pressure drop of the bolted flange joint. Hence, the effect of the internal pressure on the flange joint over the bolts can be directly demonstrated in FBG-enabled strain signals. The increasing internal pressure expands the bolted flange joint and elongates the bolts as a result of decreasing the pre-stress on the ring gasket. Thus, the increasing pressure weakens the metal-to-metal seal performance and ultimately induces leaks, which will be discussed in next section.

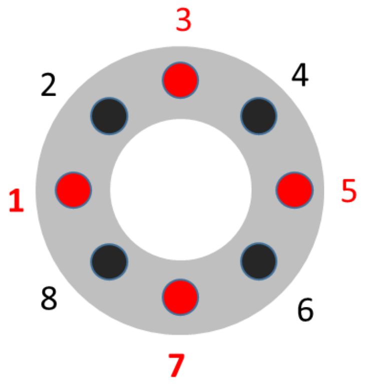

Figure 4-3 FBG-enabled Bolts with numbers on the flange assembly

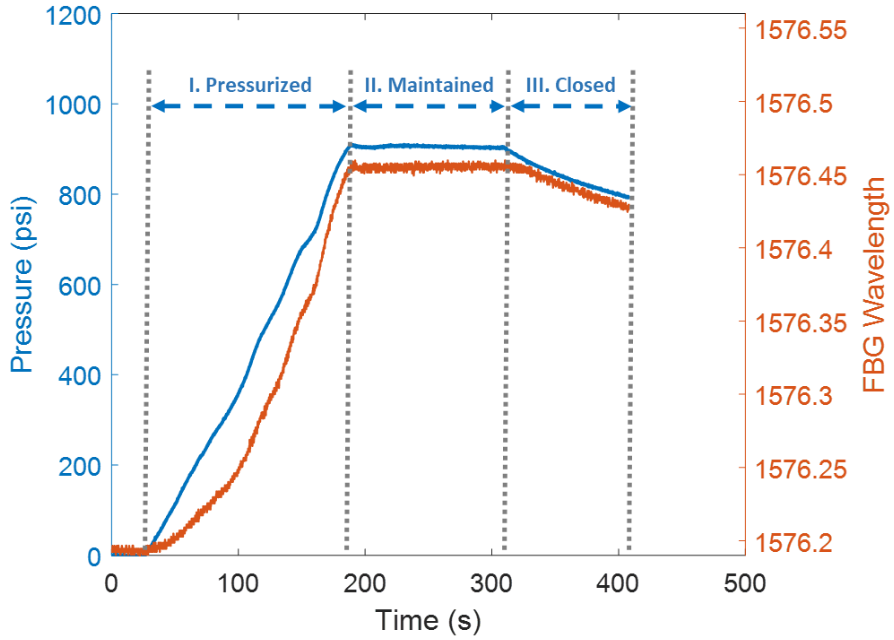

Figure 4-4 Pressure signals versus FBG-enabled strain monitoring on the Bolt-1

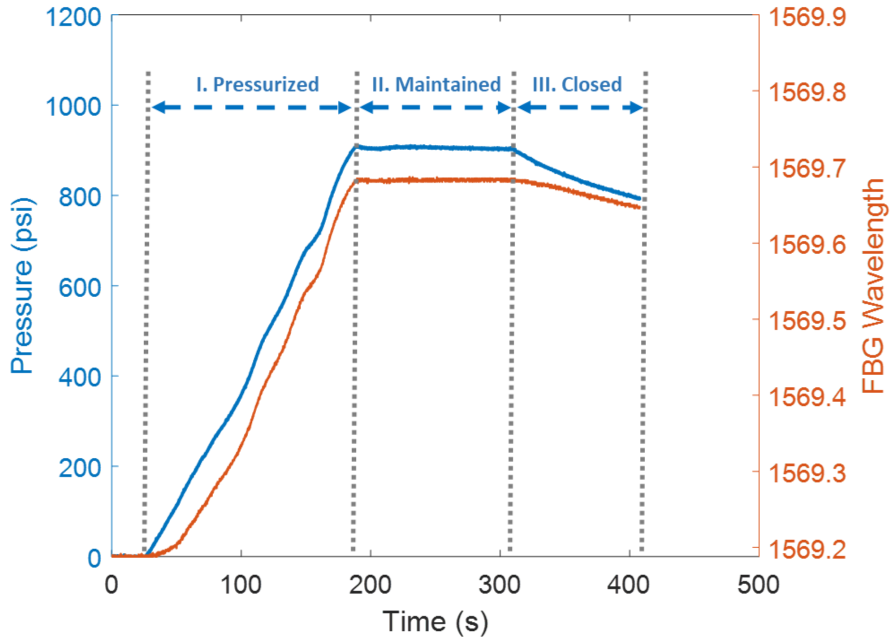

Figure 4-5 Pressure signals versus FBG-enabled strain monitoring on the Bolt-3

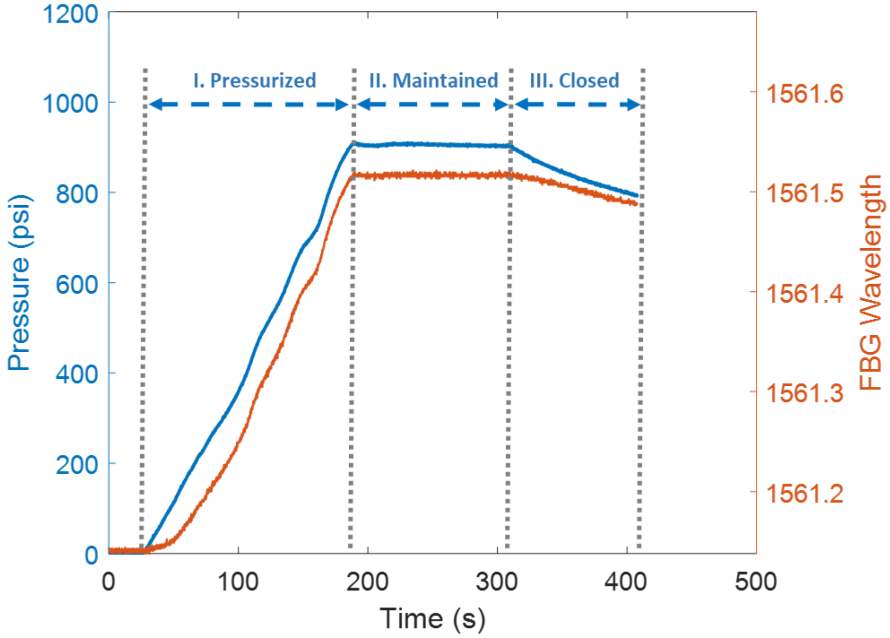

Figure 4-6 Pressure signals versus FBG-enabled strain monitoring on the Bolt-5

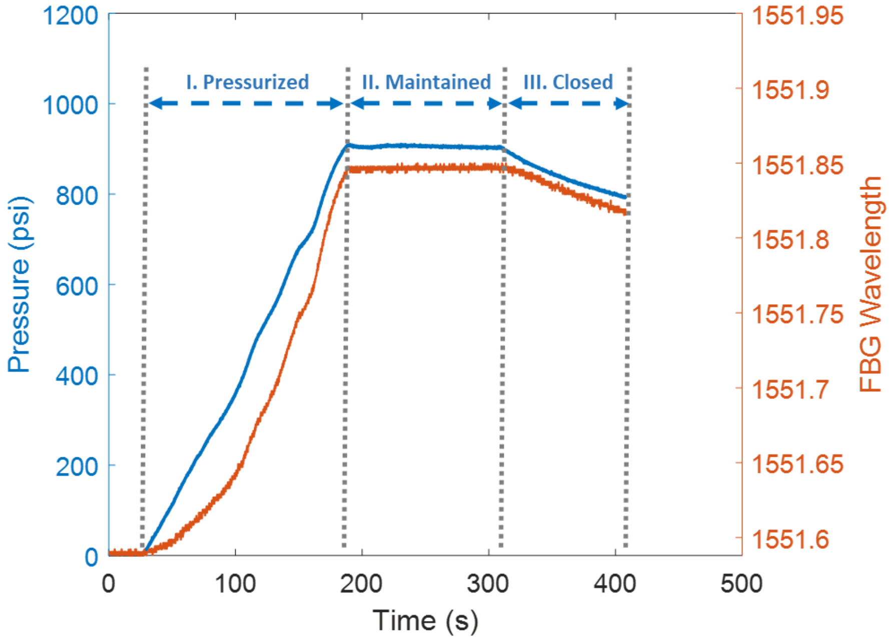

Figure 4-7 Pressure signals versus FBG-enabled strain monitoring on the Bolt-7

### 4.3.2 Results of Acoustic Emission Detection

In this section, acoustic emission signals were used to detect the pressure-induced leaks on the bolted flange joint and identify the leak-related pressure as compared with the pressure signal. The AE system consists of an AE sensor, a pre-amplifier and a data acquisition system. An AE sensor was installed on the outer surface around the flange neck. The bolted flange joint was pressurized by injecting nitrogen gas. Once a leak occurred, the acoustics generated by the sudden release of the pressurized gas were readily detected by the AE sensor in the form of elastic waves. The emitted sounds are associated with acoustic energy. During the experiments, AE signal features, AE hits and AE energy, were primarily selected to detect the leak signals. Both of them were presented in cumulative curves and transient histogram bars. The cumulative curves show the overall trend or activity over the test time, while the transient histogram bars illustrate the distribution of the signal strengths during the certain period of time.

As shown in Fig. 4-8 and Fig. 4-9, AE hits are plotted in cumulative curve and in histogram bars. Both of them show that there is none AE signal from 0 to 188.5th second and a sudden appearance of AE hits at the 188.5th second. The corresponding internal pressure is 908.8 psi, as compared with the pressure signals. When the internal pressure was maintained by constantly injecting nitrogen gas, the signal strength of AE hits started to build up during this pressure-hold period because of the constant rate of the gas injection. Once the injection of nitrogen gas was terminated at the 311.5th second, the internal pressure dropped as a result of weakening the strength of the escaping gas, thereby decreasing the growing rate of AE hits signals. Furthermore, a certain amount of pressure drop at the 311.5th second also validated the initial leak detection at the 188.5th second because of the same internal pressure of the bolted flange joint during this period of pressure-hold process.

AE energy results are presented in Fig. 4-10 and Fig. 4-11, and a similar signal behaviors are observed as a comparison of pressure signal and AE energy signals in cumulative curve and histogram bars, respectively. AE energy was the sum of the acoustic energy release from escaping gas that was captured by the AE sensor. It provided an alternative way to present the results of acoustic emissions. At the 188.5th second, it can be obviously observed that the flat cumulative AE energy curve tends to raise and the first AE energy histogram bar shows up at the same moment. This behavior correlates well with the signal feature of AE hits due to a pressure-induced leak. Under the second stage of constant internal pressure, the higher amount of AE hits illustrate the corresponding higher AE energy. When the valve of nitrogen gas was closed, the decreasing amount of AE hits was associated with the similar trend in AE energy results. Thus, results of AE hits and AE energy demonstrate the feasibility of AE system in detecting the pressure-induced gas leaks on the bolted flange joint.

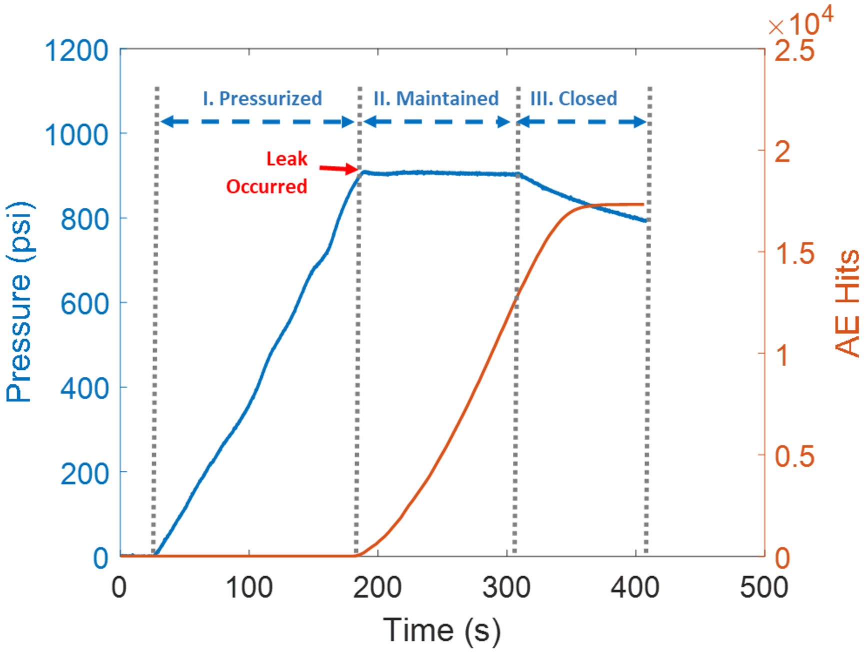

Figure 4-8 Pressure signals versus cumulative AE hit signals

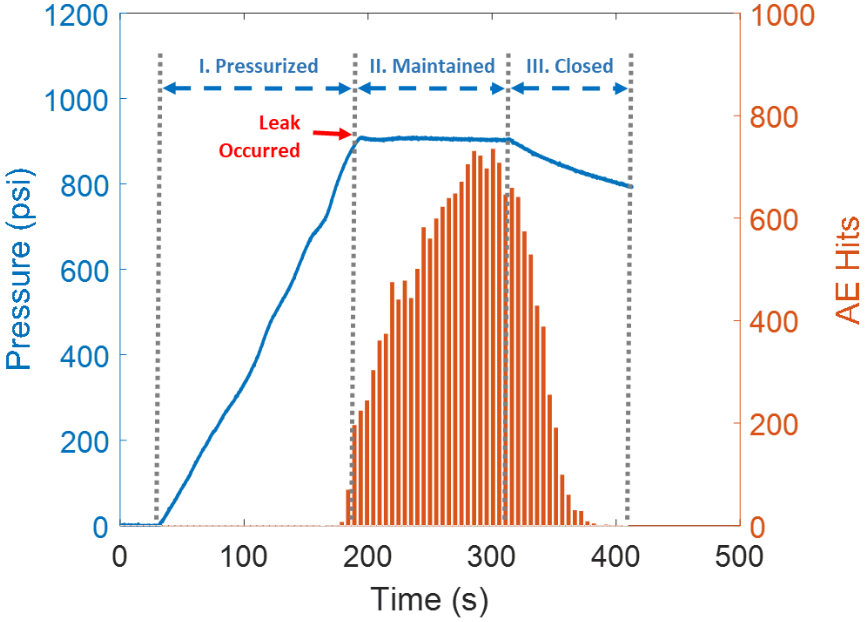

Figure 4-9 Pressure signals versus transient AE hit signals in histogram bar

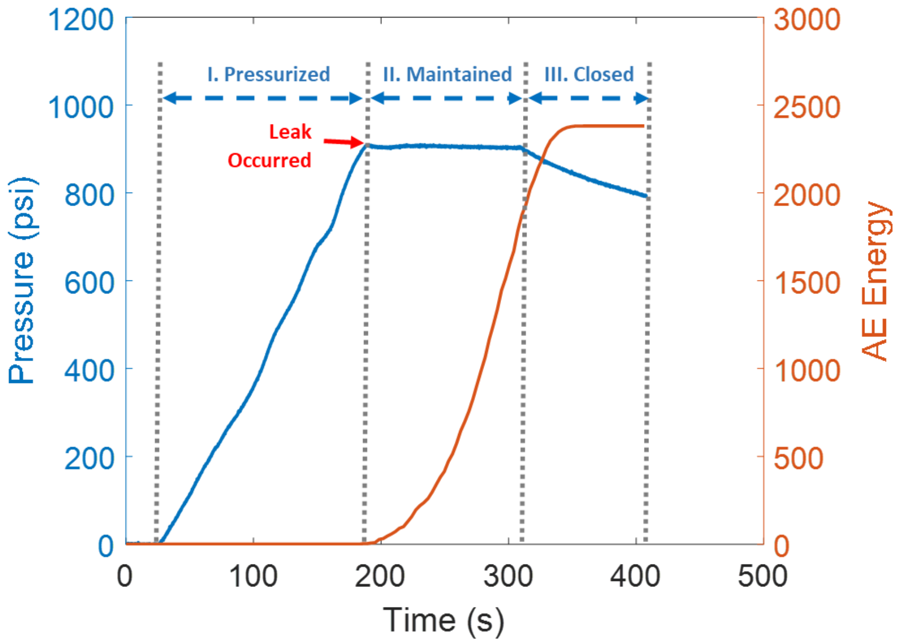

Figure 4-10 Pressure signals versus cumulative AE energy signals

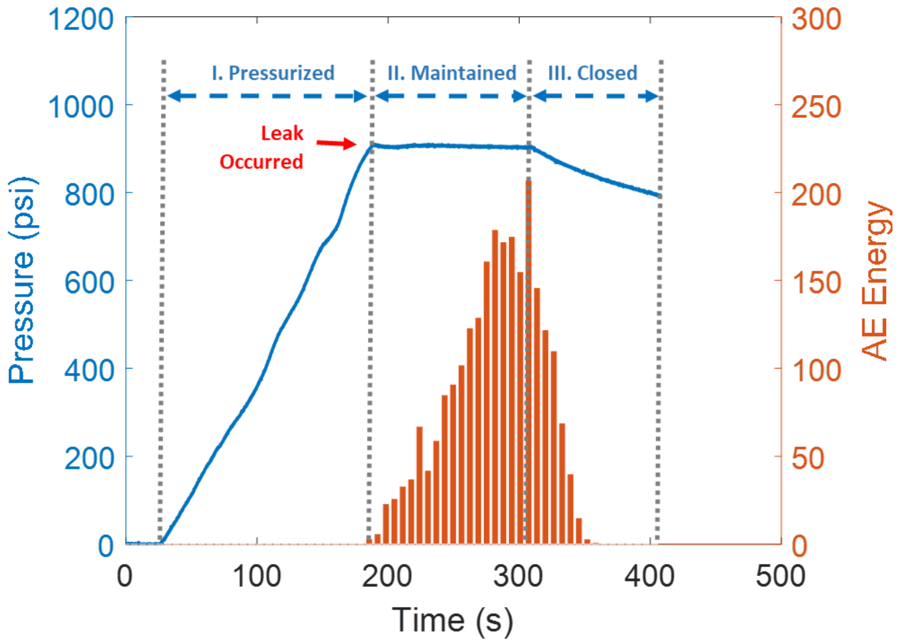

Figure 4-11 Pressure signals versus transient AE energy signals in histogram bar

## 4.4 Summary

Bolted flange joints with ring-shaped gaskets are wildly used to connect pipes, valves and other equipment in pressure vessel and pipeline systems. A prime concern of bolted flange connections is leakage failure. The development of leak detection methods for the flanged connections has been more essential to minimize the leakage issues of the bolted connections in general. In this chapter, leak detection was investigated on the bolted flange joint assembly by implementing acoustic emission system, pressure transducer, and FBG-enabled bolts. The leak around the ring gasket was artificially induced by continuously injecting nitrogen gas. As results, FBG sensor signals clearly illustrate that the real-time tension/strain changes during pressurization process and acoustic signals identify the moment of the pressure-induced leak in the features of AE hits and AE energy; and the leak-related pressure value was determined by the pressure signals. Thus, the effectiveness of AE system was verified for reliably detecting the leak of the flange joints subjected to internal pressure loads.

# 5. A Comprehensive Integrity Monitoring of Bolted Flange Joint under Combined Tensile Loads and Internal Pressure

## 5.1 Introduction

In this chapter, a comprehensive monitoring system was proposed and conducted through the implementation of all the proposed sensing technologies to investigate the integrity of the flange assembly under tensile loading and combined tensile and internal pressure loads. The transducers included Fiber Bragg Grating (FBG) sensors, acoustic emission (AE) sensors, piezoelectric transducers, and pressure transducers. The sensing methods primarily focused on FBG-based strain monitoring, piezo-based active sensing method and electromechanical impedance measurement, AE-based leak detection, and internal pressure monitoring. FBG sensor are wavelength modulated fiber optic sensors, which are sensitive to properties of strains, temperatures and pressures. The proposed strain measuring approach was designed as embedding FBG sensors into a tiny pre-drilled hole (about 1 mm) in the center of the bolts with cyanoacrylate adhesives. This FBG-enabled bolts offered a direct measurement of the strains along the bolts of the flange assembly subject to combined tensile loads and internal pressure. Piezoceramic transducers were mounted around each flange neck for performing active sensing measurement. One piezoceramic transducer was acting as an actuator, which generated stress wave as a reference signal that propagates across the interfaces of ring gasket. The propagated stress waves were received by another piezoceramic transducer as a sensor. The received signal strength and its corresponding signal energy relates with the characteristics of the contact interface between the ring gasket and the v-shaped groove on the flanges, such as contact stress and true contact area. In other words, any alterations in the characteristics of the ring gasket can induce measurable changes in the received signal, thereby evaluating the pressure-energized seal conditions of the ring gasket under combined tensile loads and internal pressure. Since the gasket possesses a dominant effect to seal flange connection, any prosperity changes caused by combined tensile loads and internal pressure can have a direct influence on the integrity of the flange connections. One piezoceramic patch was proposed to be directly bonded on the outer surface of the ring gasket in the flange joint to acquire its conductance signatures through utilizing the advantages of the direct and converse piezoelectric effects of the PZT patch. Through the surface-bonded between the PZT patch and the host specimen, the electrical impedance signature of the piezoceramic path is straightforwardly related to the mechanical properties of the host structure, especially for the local area where the piezoceramic patch was mounted. Moreover, the AE detection system has been verified to be effective to detect the gas leaks on the bolted flange joint subjected to the internal pressure in the previous study. Similarly, the combined internal pressure and tensile loads elongated the bolts on the flange joint assembly and reduced the compressive loads on the ring gasket. Once a leak occurred, the acoustics generated by the sudden release of the escaping pressurized gas could be captured by the AE sensor in the form of elastic waves. The emitted sounds were associated with acoustic energy. Therefore, two signal features of AE hits and AE energy were proposed to be used to identify the gas leaks.

As can be seen that each technology has advantages for specific aspect to exhibit the integrity of bolted flange joint. However, these multiple sensing technologies have never been implemented together to comprehensively investigate the bolted flange joint. Therefore, in this chapter, the proposed comprehensive integrity monitoring system was conducted to investigate the integrity of the bolted flange joint under tensile loads and combined tensile and internal pressure loads. The proposed studies can provide a better understanding of flange connections behaviors beyond the current design codes and specifications and further offer potential solutions of real-time monitoring technologies for effectively evaluating and assuring the integrity of the bolted flange joints.

## 5.2 Experimental Setup and Procedures

To evaluate the characteristic changes and leak detection of the bolted flange joint subject to combined tensile loads and internal pressure, two pieces of API standard flanges (4-1/16", API 6A Type 6B, 2000 psi) were specifically designed for the purpose of tensile testing as shown in the Fig. 5-1. Each end of the flange neck was welded with a plate to form a closed chamber to contain the pressure when a pair of flanges were assembled together. One threaded hole was drilled on the bottom plate for the installation of a tubing adapter for connecting with a nitrogen gas cylinder. The pressure capacity of the nitrogen gas cylinder was 3500 psi. Another threaded hole was made for a pressure relief valve on the top plate. As demonstrated in Fig. 5-2, to accommodate the flange joint assembly for the hydraulic wedge grip on the MTS testing frame, two short steel pipes (outer diameter of 4.50 inch and inner diameter of 4.00 inch) were welded to each flange neck, while one vertical steel bar coupled with two horizontal steel pins was designed to ensure the entire flange assembly feasible to be mounted into the grip system. The length and diameter of the steel bar was 18.50 inch and 2.50 inch, respectively. The diameter of the two pin holes was 1.38 inch on the steel bar. For the hydraulic wedge grip system, it allowed a maximum operation pressure of 62 MPa and a force capacity of 500 kN. Furthermore, two ring-shaped spacers were fabricated and added between the steel bar and the short steel pipe to align the steel bar throughout the short welded pipe on the flanges, which ensured vertical loading force and minimized the bending strains on flange joint assembly.

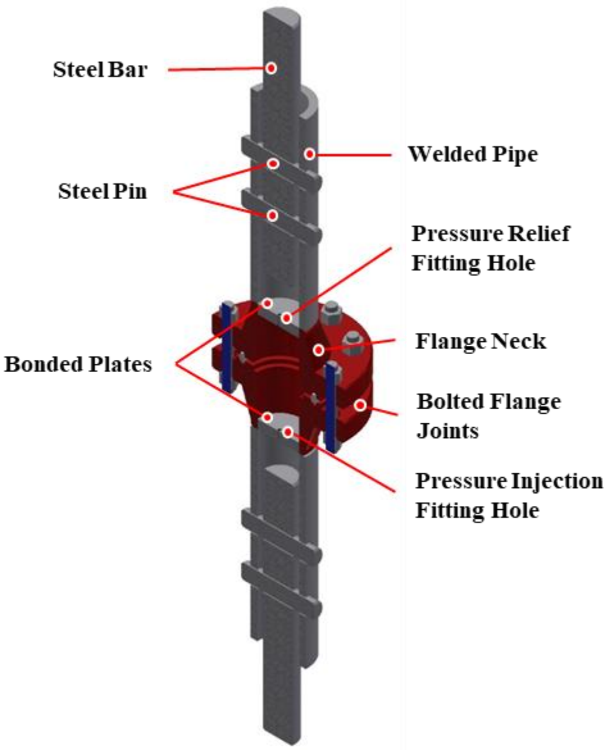

Figure 5-1 3D modeling of the bolted flange joint for tensile testing

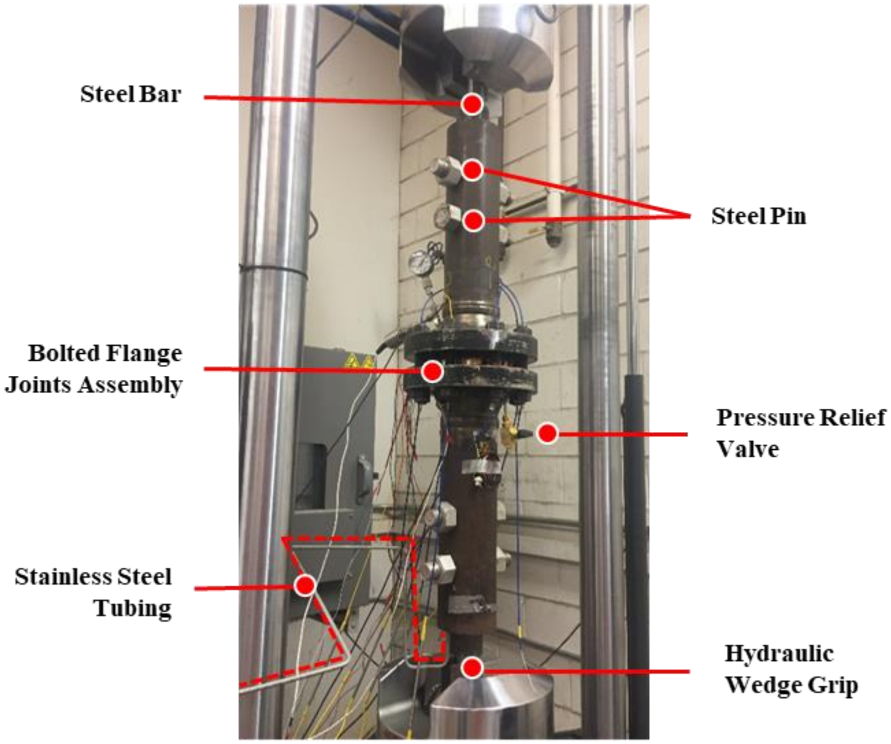

Figure 5-2 Demonstration of the bolted flange joint on MTS test frame

Once the flange assembly was installed onto the MTS test frame, the proposed monitoring systems, including Fiber Bragg Grating (FBG) strain monitoring system, acoustic emission (AE) leak detection system, piezo-based active sensing system, piezo-based electromechanical impedance analyzing system and internal pressure monitoring system, were installed on the flange assembly as shown in Fig. 5-3. During the experiments, each bolt was uniformly torqued by 30 ft-lb, which compressed two flanges together against the ring gasket causing the deformation of the mating surfaces between the ring gasket and flange grooves and thus formed a metal-to-metal seal. Then, the internal chamber of the bolted flange joint was pressurized through injecting the nitrogen gas to check the seal of flange connection. The sealing performance was determined by the pressure containment that was capable of withstanding an initial pressure of 1000 psi. After that, the tensile load was generated and applied on the flange assembly on the MTS test frame from 0 to 200 kN with an operation rate of 20 kN/min. The increasing tensile load attempted to gradually counteract the compressive load acting on the ring gasket due to the tightened bolts, thereby weakening the metal-to-metal seal until a leak occurred.

As shown in Fig. 5-4, pressure gauge and transducer were installed on the flange to show the real-time internal pressure and to acquire the pressure signal of the bolted flange joint simultaneously; FBG-enabled bolts were used to provide a direct measurement of the strain changes along the bolts of the flange assembly subjected to combined tensile and internal pressure loads; AE sensor was installed on the outer surface around the flange neck. Once a leak occurred, the acoustics generated by the sudden release of the escaping pressurized gas could be captured by the AE sensor in the form of elastic waves. The emitted sounds were also associated with acoustic energy. Therefore, AE hits and AE energy were acquired to identify the gas leaks.

As can be see that the ring gasket is one of the most important components for assuring a seal between flange connections, however, it is also one of the most common factors leading to seal failure of the bolted flange connections. During the tensile loading, two piezoceramic patches were mounted on the surface near the flange neck to conduct piezo-based activing sensing measurements, as shown in Fig. 5-5. The length, width and thickness of the PZT patch was 15mm, 5mm, and 1mm, respectively. The frequency range of the actuated swept-sine wave was from 10 kHz to 650 kHz at a sampling frequency of 2 MHz. Alterations in the characteristics of the ring gasket on the bolted flange joint under the applied loads can be observed in the form of signal strength and the corresponding signal energy from the piezo-based active sensing results. Additionally, one more piezoceramic patch was directly bonded on the outer surface of the ring gasket for conducting electromechanical impedance (EMI), as shown in Fig. 5-6. The stress relaxation between the ring gasket and the flange groove altered the mechanical properties of the ring gasket, which consequently changed the PZT's electrical impedance signatures in the way of the peak frequency and conductance.

During the experiments, to avoid conflicts of electrical signals between the piezo-based monitoring system and AE leak detection system, step-tensile loading tests were conducted, which meant the MTS operation was paused for 300 seconds at each increment of 40 kN from 0 to 200 kN. During this period of time, measurements of piezo-based active sensing, electromechanical impedance, and AE system were conducted, respectively. However, strain monitoring signals from FBG-enabled bolts, internal pressure signals, and tensile loads from the MTS test frame were continuously recorded. After the test with step loads, a series of continuous tests without interruption were conducted under different torques applied on the bolts. Therefore, the characteristic variations of the flange connection under the tensile loads and combined tensile and internal pressure loads were both studied by the piezo-based active sensing method and electromechanical impedance measurement, respectively. In addition, the real-time monitoring of FBG enabled bolt strain, internal pressure and AE acoustics enabled to determine the leakage failures of the flange connections subjected to the increasing tensile and internal pressure loads. Furthermore, the leak-related tension limit was preliminarily obtained under different tightened torques on the bolts, which offered a useful leakage failure envelope to potentially mitigate the future failures in service.

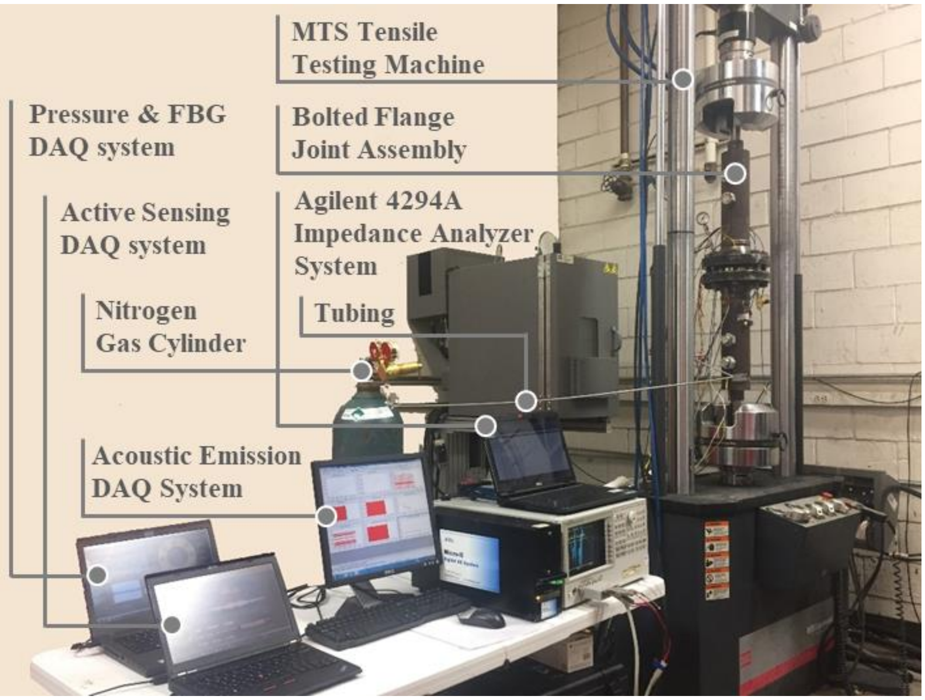

Figure 5-3 A comprehensive monitoring system for flange joint on the MTS test frame

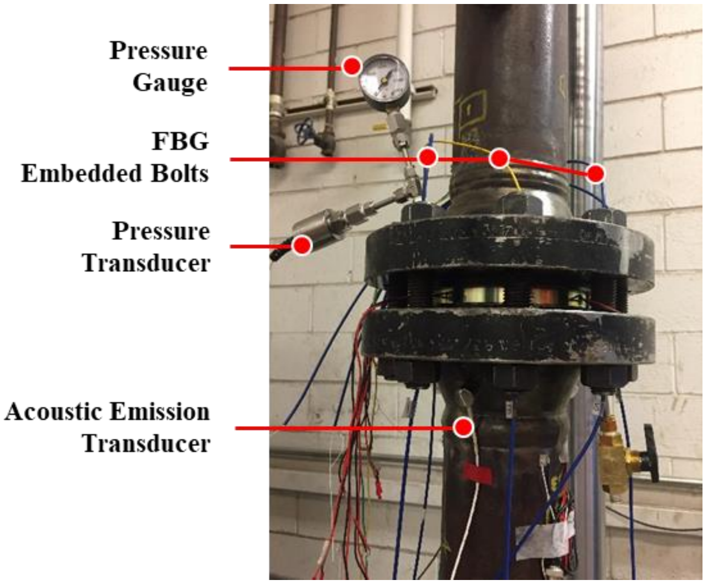

Figure 5-4 Experimental setup of transducers on the bolted flange joint

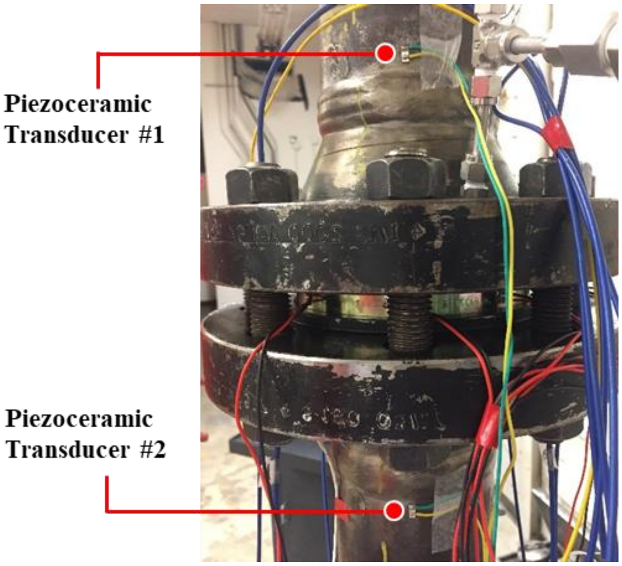

Figure 5-5 Demonstration of active sensing measurement

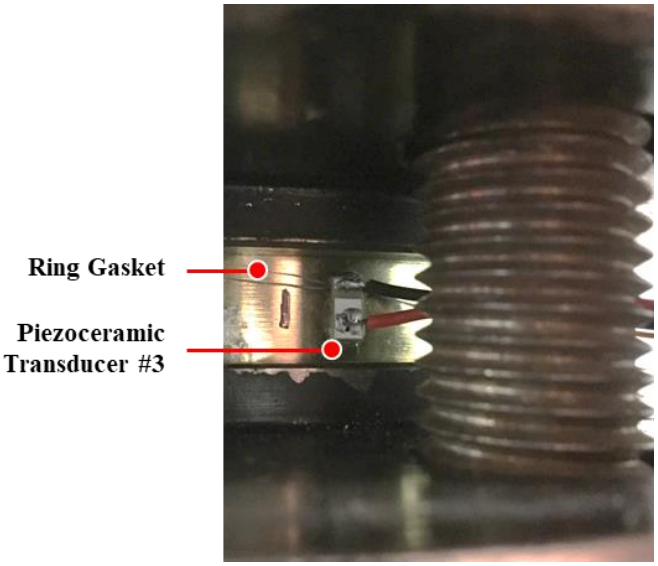

Figure 5-6 Demonstration of electromechanical impedance Measurement

## 5.3 Results and Discussions

### 5.3.1 Results of FBG-enabled Bolt Strain Monitoring

As discussed in the prior section, the step-tensile loads were cumulatively generated and applied on the flange assembly from 0 to 200 kN with each increment of

40 kN, as shown in the relationship between the tensile loads and time in the Fig.5-7 (a). In other words, when the operation of the MTS test frame was paused for 300 seconds, the measurements of piezo-based active sensing, electromechanical impedance and AE leak detection were conducted, respectively, while the strain monitoring signals from FBG-enabled bolts, internal pressure signals were continuously recorded at the beginning of the test. Four FBG-enabled bolts were selected to present the strain monitoring results for the bolted flange joint, as shown in Fig. 5-7 (b). And the results of strains along the bolts under tensile loads were plotted in Fig. 5-7 (c), Fig. 5-7 (d), Fig. 5-7 (e), and Fig. 5-7 (f) for bolt-1, bolt-3, bolt-5 and bolt-7, respectively. Similar behaviors in the strains results over the four FBG-enabled bolts were observed. When one of them was compared with the tensile loads generated from the MTS test frame, as shown in Fig. 5-8, the strains along the bolt closely correlated with the tensile load applied on the flange assembly. However, once the tension increased from 160 kN to 200 kN, a sudden reduction occurred in the strain signals. One more comparison between the FBG strain result and internal pressure was presented in Fig. 5-9, which revealed that the internal pressure started to drop at the same place where a sudden FBG strain reduction occurred. This phenomenon indicated a leak of the flange joint due to combined tensile load and internal pressure. The escaping gas immediately caused a sudden drop of the internal pressure that directly reduced the end cap forces acting on the flange joint in axial direction, thereby resulting in the strain reduction along the bolts. Therefore, the gas leak was determined by the indications of a sudden internal pressure drop and FBG enabled strain reduction over the results.

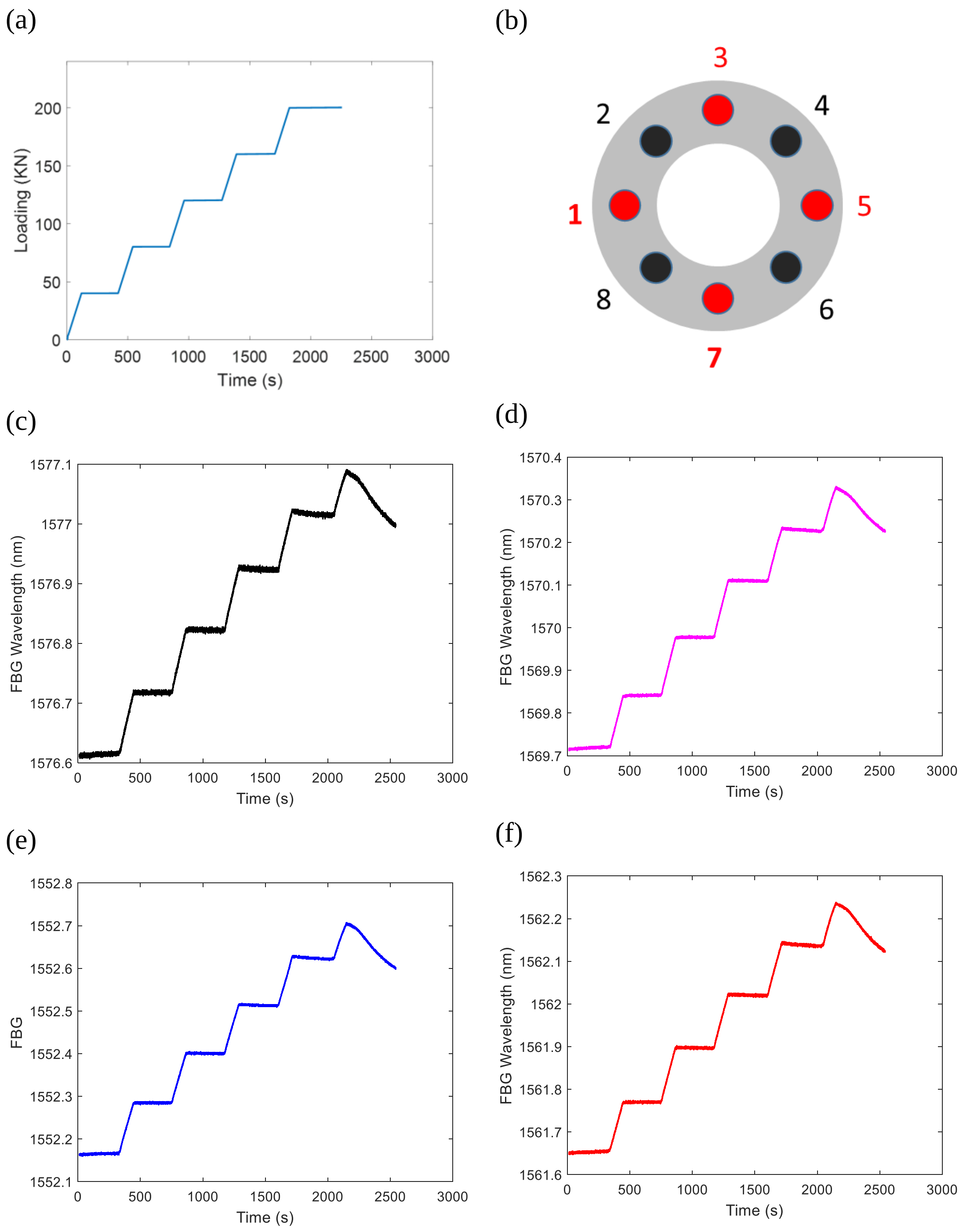

Figure 5-7 Experimental Results: (a)tensile loading from the MTS test frame, (b) FBG-enabled bolts numbering on the flange, (c) FBG strains on bolt-1, (d) FBG strains on bolt-3, (e) FBG strains on bolt-5, (f) FBG strains on bolt-7

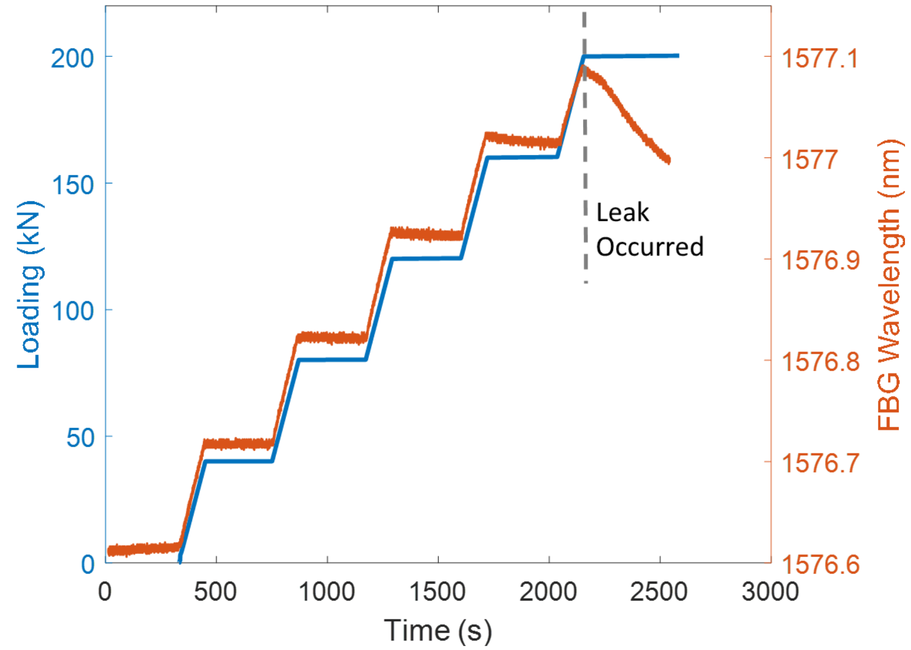

Figure 5-8 Comparison of MTS loadings and FBG strains on bolt-7

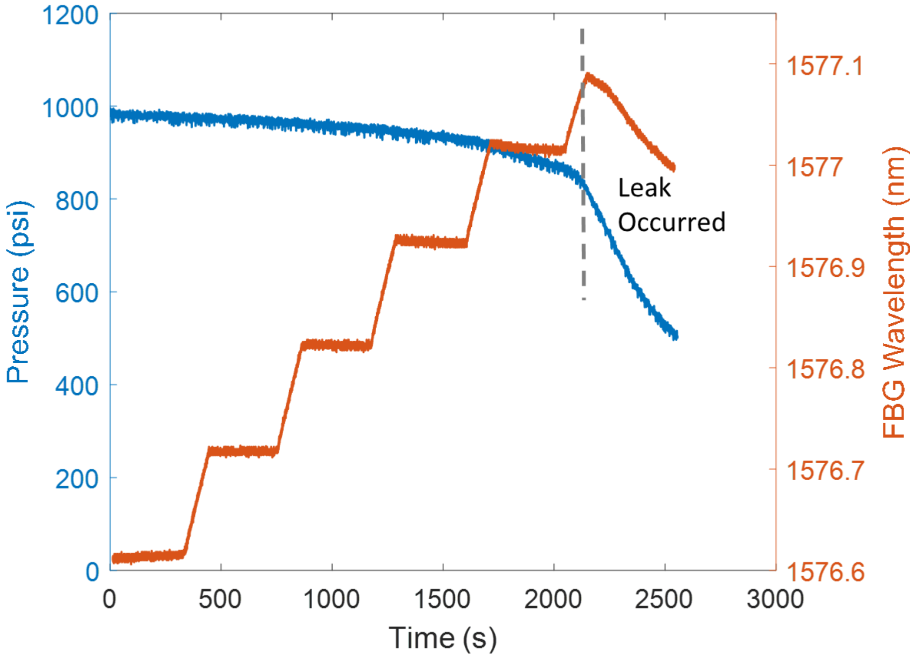

Figure 5-9 Comparison of internal pressure and FBG strains on bolt-7

### 5.3.2 Results of AE Leak Detection System

AE sensor is sensitive to capture the acoustics generated by the sudden release of the escaping pressurized gas, in the form of elastic waves. And the AE system has been verified to effectively detect the pressure-induced gas leaks in the Chapter 4. In this experiment, the AE leak detection system was utilized to identify the leaks on the bolted flange joint due to the combined effect of the tensile and the internal pressure loads. In this section, the AE leak detection signals were compared with the internal pressure and FBG strains along the bolts to confirm the leaks. FBG strains were compared with the transient AE energy signals and the cumulative AE energy signals, in the Fig. 5-10 and Fig. 5-11, respectively. The appearance of a sudden increase in transient AE energy at the 2099th second definitely demonstrated the leakage occurred, which also coincided with the strains reduction along the bolts. A similar phenomenon was observed as compared the strains with the cumulative AE energy signals, as shown in Fig. 5-11. Some minor AE energies before the leakage were acquired due to the clamping and tensile loads from the interface between the steel bar and the hydraulic grip system. A comparison between the internal pressure and AE energy was exhibited in Fig. 5-12 and Fig. 5-13. At the moment of a sudden pressure drop, the transient AE energy also rapidly accumulated as a result of acquiring more acoustic signals due to the escaping pressurized gas. The abrupt changes of the internal pressure and the AE energies were in a good agreement. Therefore, the FBG-based strain monitoring and internal pressure monitoring results were verified by the AE detection results for effectively monitoring the leak detection of the bolted flange joint.

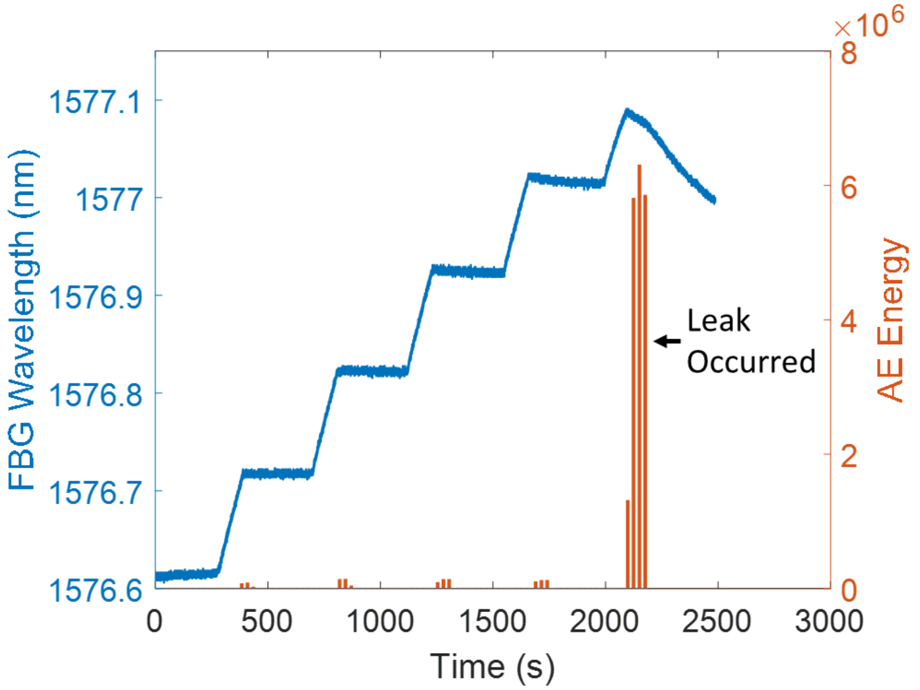

Figure 5-10 Comparison of FBG strains and the transient AE energy signals

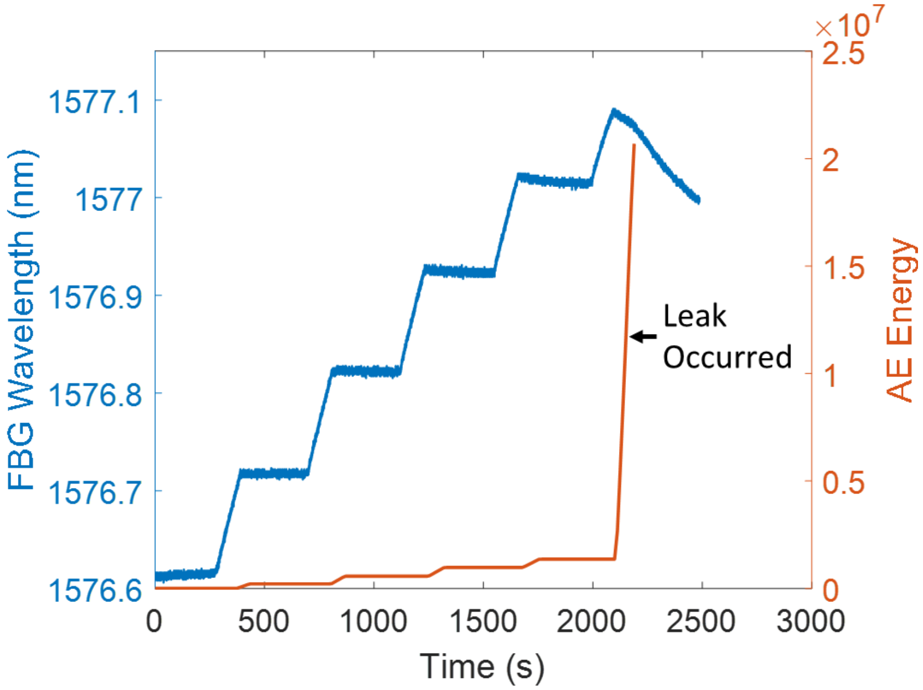

Figure 5-11 Comparison of FBG strains and the cumulative AE energy signals

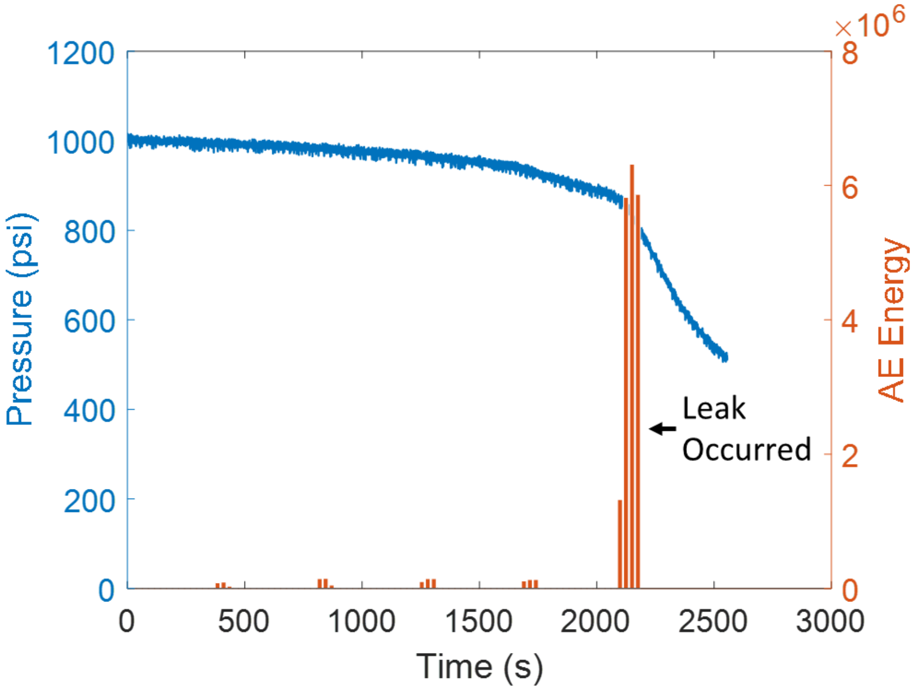

Figure 5-12 Comparison of internal pressure and the transient AE energy signals

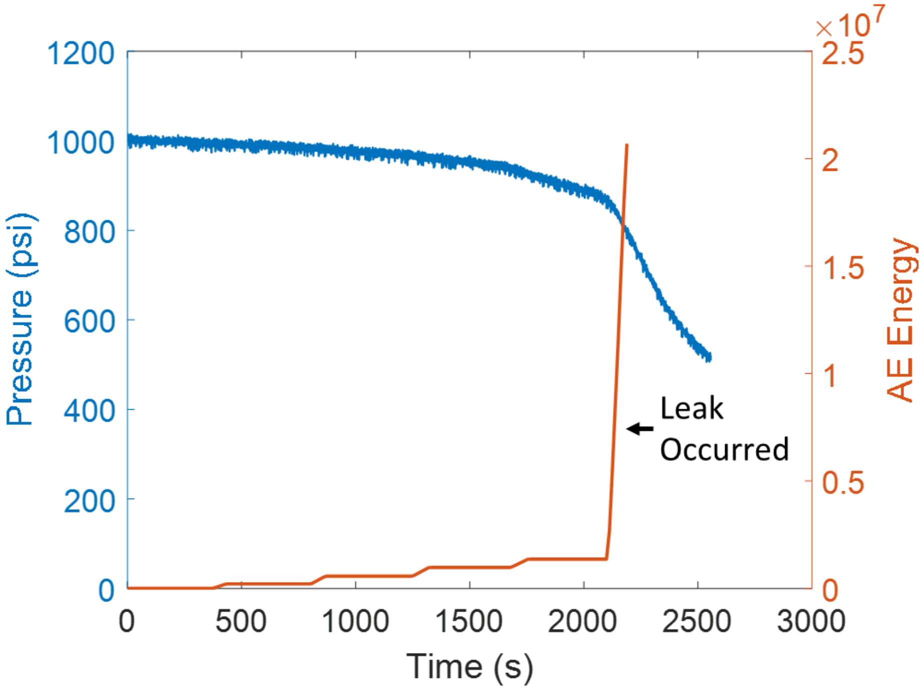

Figure 5-13 Comparison of internal pressure and the cumulative AE energy signals

### 5.3.3 Results of piezo-based Active Sensing

In this section, the characteristic variations of the flange connection under tensile load condition and combined tensile loads and internal pressure were both monitored and investigated through the active sensing method. For the piezo-based active sensing measurement, a swept-sine signal with an amplitude of 10 volts and excitation frequency range from 10 kHz to 650 kHz within 1 second was generated by DAQ board (National Instruments USB-6361), while the acquired signal strength of the PZT sensor directly depend on the characteristics of the wave propagation path. The changes around connection interface could readily alter the acquired signal feathers of signal amplitudes and signal energies. The received signals, corresponding to the different tensile loads from 0 kN to 200 kN with each increment of 40 kN, are plotted in Fig. 5-14. Through comparing the results, the signal amplitudes do not change obviously, but the signal strength is slightly weakened as observed in the comparison result in Fig. 5-15 (a). When wavelet packed transform method is utilized to compute the signal energy, as plotted in Fig. 5-15 (b). It is clear to see the smooth declining trend associated with a higher tensile load which directly reduces the stress against the contact interface between the gasket and groove as a result of signal attenuation in wave propagation.

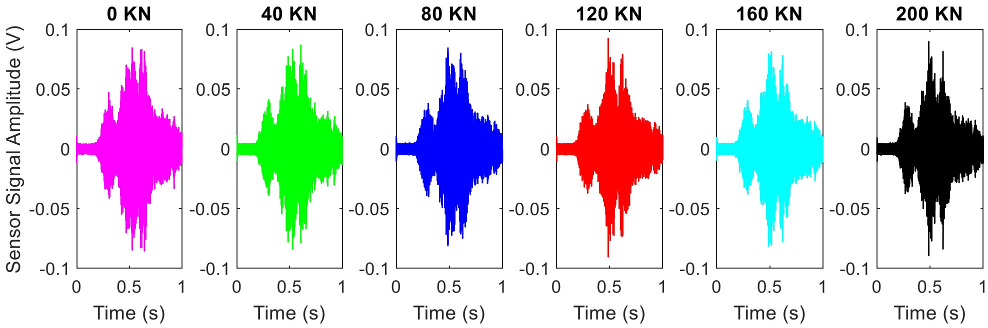

Figure 5-14 Active sensing results under different tensile loads

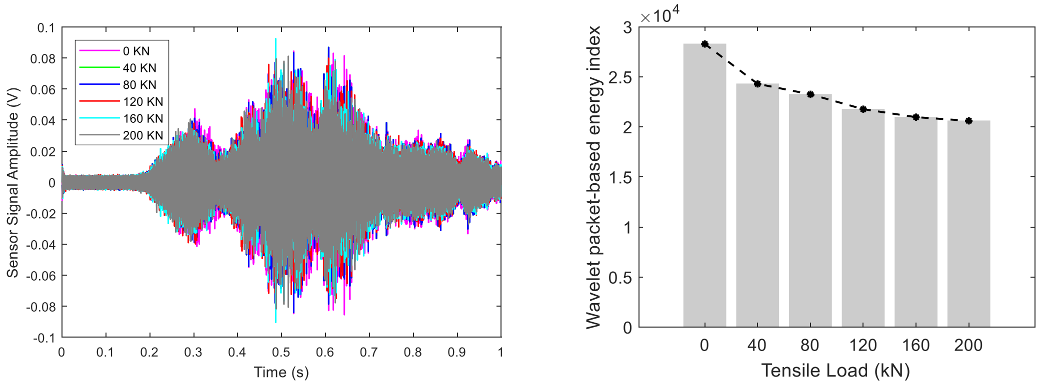

(a) (b)

Figure 5-15 Comparison of each piezo-based active sensing results under tensile loads (a) time-domain response and (b) wavelet packet-based energy index

When the bolted flange join was pressurized with 1000 psi, the same test procedure of active sensing measurements was repeated. Fig. 5-16 shows the active sensing results of the bolted flange joint subjected to combined tensile loads and internal pressure. The time-domain responses slightly changed in signal amplitude and peak strength, as shown in Fig. 5-17 (a). When the corresponding wavelet packet-based energy indices are plotted in Fig 5-17 (b), a similar declining trend is observed, however a continued decrease of signal energy at 160 kN and 200 kN is observed, which actually indicates the occurrence of the gas leaks as compared with the other detected results.

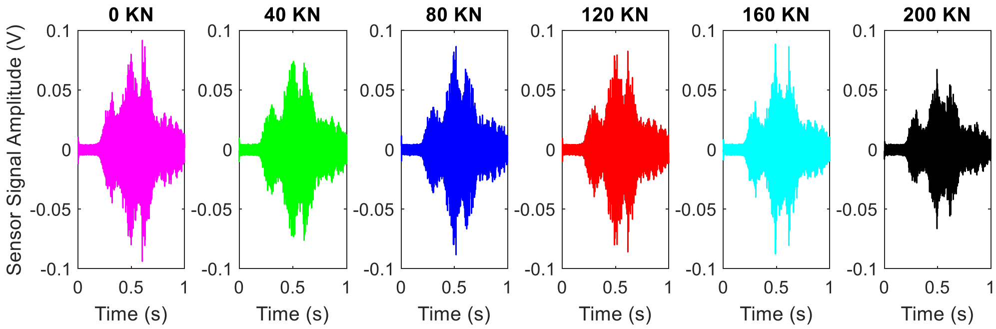

Figure 5-16 Active sensing results under combined tensile loads and internal pressure

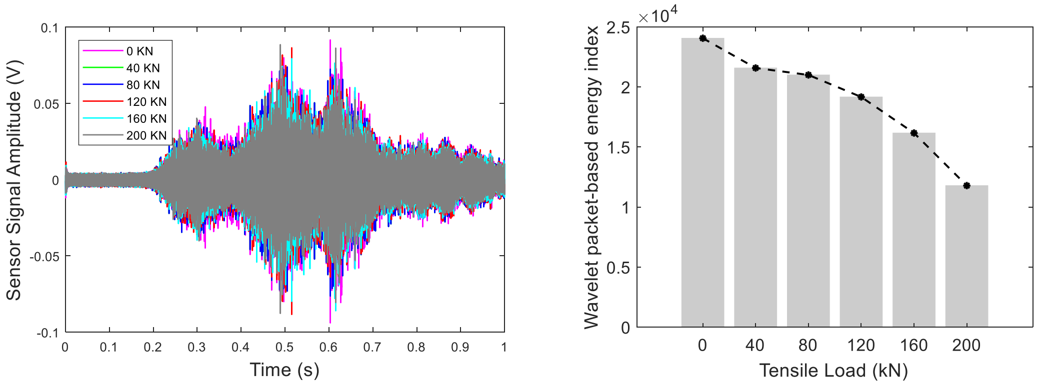

(a) (b)

Figure 5-17 Comparison of active sensing results under combined tensile loads and internal pressure (a) time-domain response and (b) wavelet packet-based energy index

### 5.3.4 Results of Electromechanical Impedance (EMI)

EMI signatures were measured from one piezoceramic patch bonded on the outer surface of the ring gasket under both conditions of tensile loadings and combined tensile loadings and internal pressure. The externally applied tensile load on the bolted flange assembly directly changes the stress between the ring gasket and the flange groove and altered the mechanical properties of the ring gasket. Consequently, these mechanical variations can be reflected on the electrical impedance signatures, such as the peak frequency and conductance. As shown in Fig. 5-18, the conductance signatures from a frequency range between 100 kHz and 200 kHz are acquired from the flange connection subjected to the tensile loadings. And a zoomed-in view is presented in Fig. 5-19. Each measurement of conductance was repeated by a separate test. The peak frequencies and the corresponding conductance signatures under the different tensile loads are summarized in Table 5-1, Table 5-2, and plotted in Fig. 5-20, respectively. Both peak frequency and the corresponding conductance decrease with the applied tensile loads from 0 kN to 80 kN, and then reverse to an increasing trend from 80 kN to 200 kN. This behavior may need to be further investigated. However, when the bolted flange assembly was pressurized to 1000 psi and the same impedance-based measurements was repeated. As shown in Fig. 5-21 and Fig. 5-22, both the peak frequency and the corresponding conductance consistently increase with the higher tensile loads. The measured results of the repeated tests are summarized in Table 5-3 and Table 5-4. And a near-linear growing trend line illustrates the relationship of the peak frequency and the corresponding conductance of the bolted flange assembly under combined tensile load and internal pressure, as shown in Fig. 5-23.

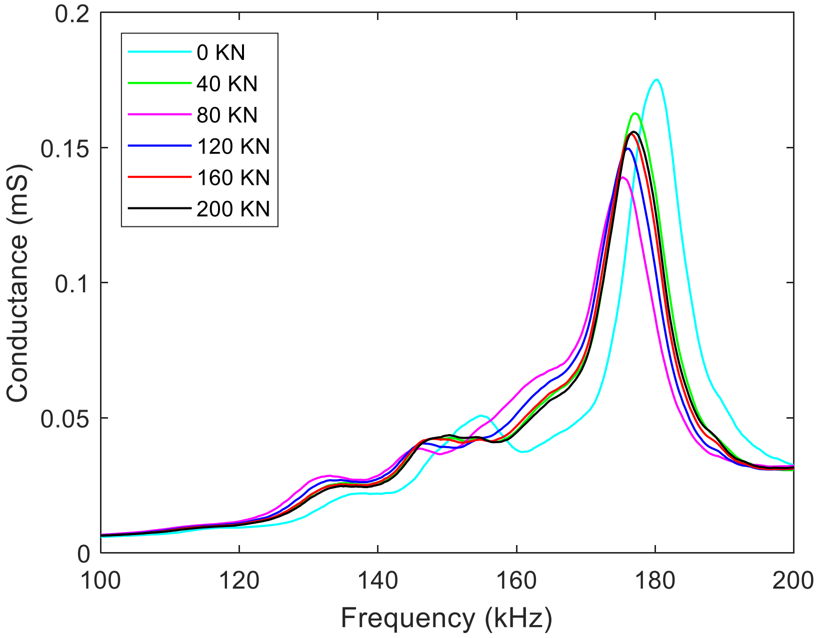

Figure 5-18 Conductance signatures of the flange assembly under tensile loads

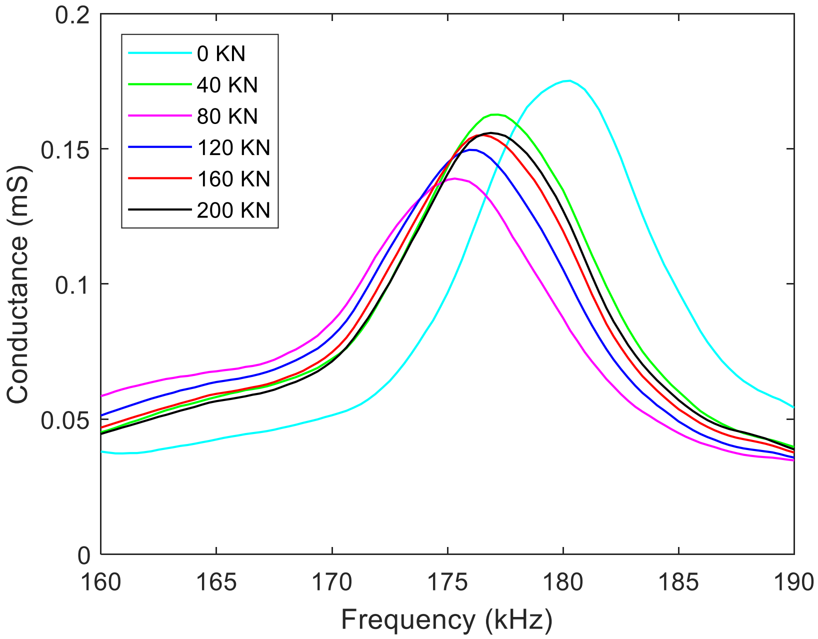

Figure 5-19 Zoomed-in view of conductance signatures of the flange assembly under tensile loads

Table 5-1 Summary of peak frequency of the flange assembly under tensile loads

| **No.** | **Tensile Loads (kN)** | **Peak Frequency (kHz)** | | | **Standard Deviation** |
|---|---|---|---|---|---|
| | | **Test-1** | **Test-2** | **Average** | |
| 1 | 0 | 180.000 | 179.400 | 179.700 | 0.424 |
| 2 | 40 | 177.200 | 176.900 | 177.050 | 0.212 |
| 3 | 80 | 175.300 | 175.000 | 175.150 | 0.212 |
| 4 | 120 | 175.900 | 175.900 | 175.900 | 0.000 |
| 5 | 160 | 176.600 | 176.300 | 176.450 | 0.212 |
| 6 | 200 | 176.900 | 176.900 | 176.900 | 0.000 |

Table 5-2 Summary of conductance of the flange assembly under tensile loads

| **No.** | **Tensile Loads (kN)** | **Conductance (mS)** | | | **Standard Deviation** |
|---|---|---|---|---|---|
| | | **Test-1** | **Test-2** | **Average** | |
| 1 | 0 | 0.175 | 0.171 | 0.173 | 0.003 |
| 2 | 40 | 0.163 | 0.159 | 0.161 | 0.003 |
| 3 | 80 | 0.139 | 0.136 | 0.137 | 0.002 |
| 4 | 120 | 0.150 | 0.146 | 0.148 | 0.003 |
| 5 | 160 | 0.156 | 0.154 | 0.155 | 0.001 |
| 6 | 200 | 0.156 | 0.155 | 0.155 | 0.001 |

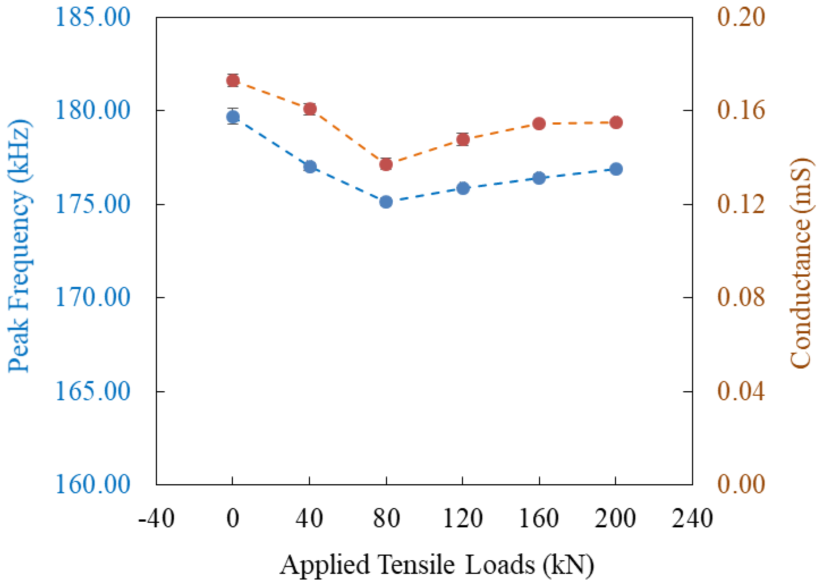

Figure 5-20 Summary of peak frequency and conductance under the tensile loads

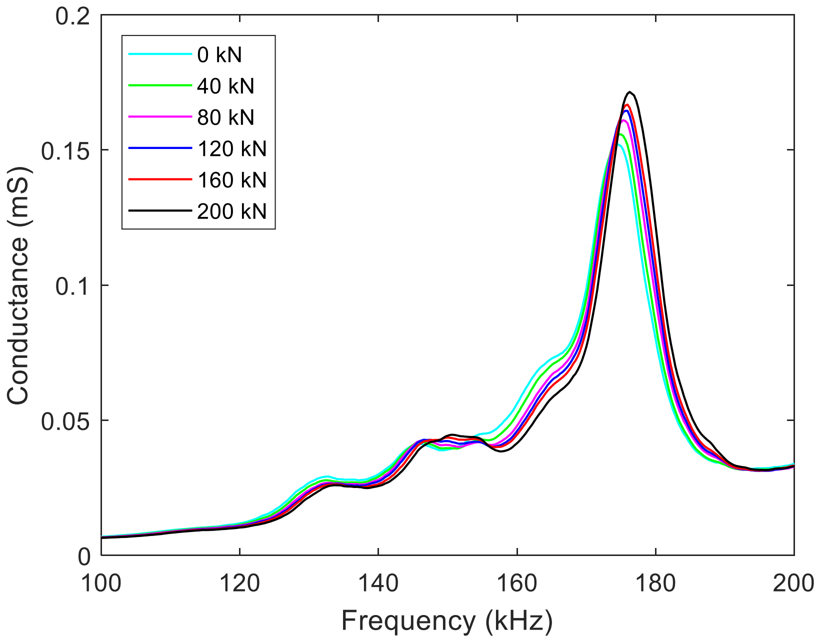

Figure 5-21 Conductance signatures of the flange assembly under combined tensile and internal pressure loads

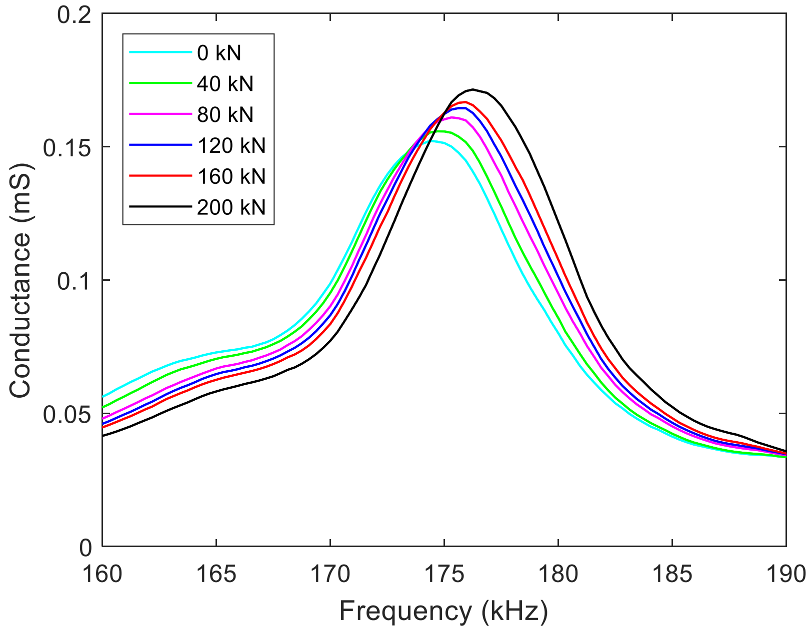

Figure 5-22 Zoomed-in view of conductance signatures of the flange assembly under combined tensile and internal pressure loads

Table 5-3 Summary of peak frequency of the flange assembly under combined tensile and internal pressure loads

| **No.** | **Tensile Loads (kN)** | **Peak Frequency (kHz)** | | | **Standard Deviation** |
|---|---|---|---|---|---|
| | | **Test-1** | **Test-2** | **Average** | |
| 1 | 0 | 175.900 | 174.400 | 175.150 | 1.061 |
| 2 | 40 | 176.200 | 175.000 | 175.600 | 0.849 |
| 3 | 80 | 176.300 | 175.300 | 175.800 | 0.707 |
| 4 | 120 | 177.200 | 175.600 | 176.400 | 1.131 |
| 5 | 160 | 178.100 | 175.900 | 177.000 | 1.556 |
| 6 | 200 | 178.800 | 176.300 | 177.550 | 1.768 |

Table 5-4 Summary of conductance signatures of the flange assembly under combined tensile and internal pressure loads

| **No.** | **Tensile Loads (kN)** | **Conductance (mS)** | | | **Standard Deviation** |
|---|---|---|---|---|---|
| | | **Test-1** | **Test-2** | **Average** | |
| 1 | 0 | 0.161 | 0.152 | 0.156 | 0.006 |
| 2 | 40 | 0.163 | 0.156 | 0.160 | 0.005 |
| 3 | 80 | 0.164 | 0.161 | 0.162 | 0.002 |
| 4 | 120 | 0.171 | 0.165 | 0.168 | 0.005 |
| 5 | 160 | 0.178 | 0.167 | 0.172 | 0.008 |
| 6 | 200 | 0.194 | 0.171 | 0.183 | 0.016 |

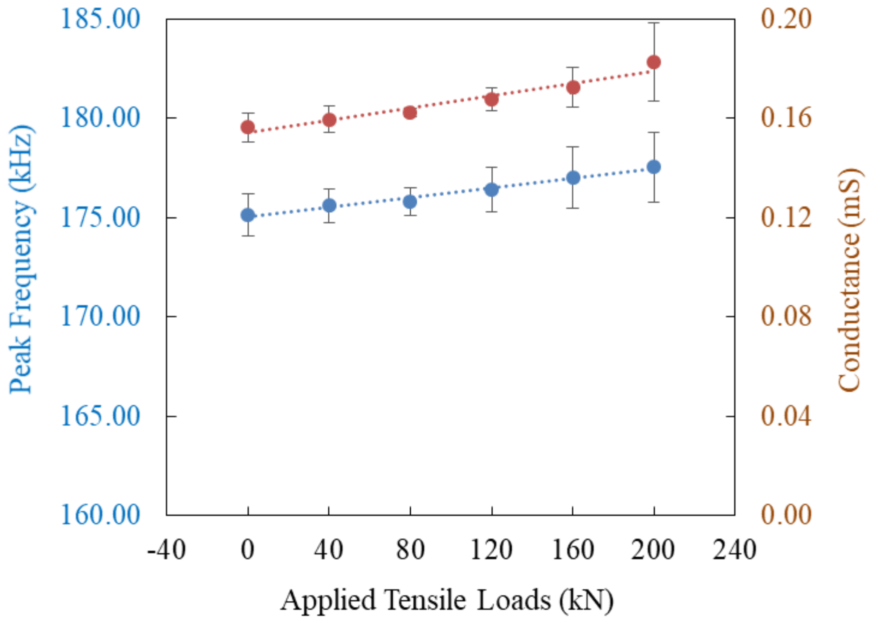

Figure 5-23 Summary of peak frequencies and conductance signatures under the applied tensile and internal pressure loads

### 5.3.5 Results of leak-related Tension Limit

The adequate tensile load for causing a leak around the ring gasket of the bolted flange joint primarily depended on the torque values applied on the bolts. In this section, studies of leak related tension limit under combined condition of tensile loads and internal pressure were conducted to determine and summarize the leak-related tension limits corresponding to the different applied torque on the bolted flange joint. During each experiment, the bolted flange joint was initially pressurized to 1000 psi and the tensile load was continuously generated and applied on the flange assembly until leak occurred by using the MTS test frame. Due to the limited capacity of the MTS test frame of 500 kN, the maximum tightened torque applied on the bolts for a leakage failure was 40 ft-lb. Therefore, the torque range was tested between 20 ft-lb to 40 ft-lb with an increment of 5 ft-lb. The internal pressure and FBG enabled strain monitoring along bolts are plotted from Fig. 5-24 to Fig. 5-28 corresponding to the applied tensile loadings on the bolted flange joint under the tightened torque value of 20, 25, 30, 35, and 40 ft-lb, respectively. Both the internal pressure and strain curves experience a linear trend before the leakages, as the illustrated in dash line. Once the leakage occurred, the internal pressure clearly tends to drop and consequently reduced the compressive load on the bolts as well as the strains reduction on the bolts. Based on this phenomenon of a sudden pressure drop and strain reduction on bolts, the leak-related tensile loads can be accordingly determined from both curves. Each case was tested twice and the corresponding results are summarized in Table 5-5. The results are also plotted in Fig. 5-29. It is clear that the preliminary results exhibit a near-linear relationship between the bolt torque and the leak-related tensile load, which directly provide a useful insight to understand the leakage failure envelope considering the applied tensile loading the tightened torques on the bolts and thus offer a potential solution to avoid the future leakage failures of the bolted flange connections.

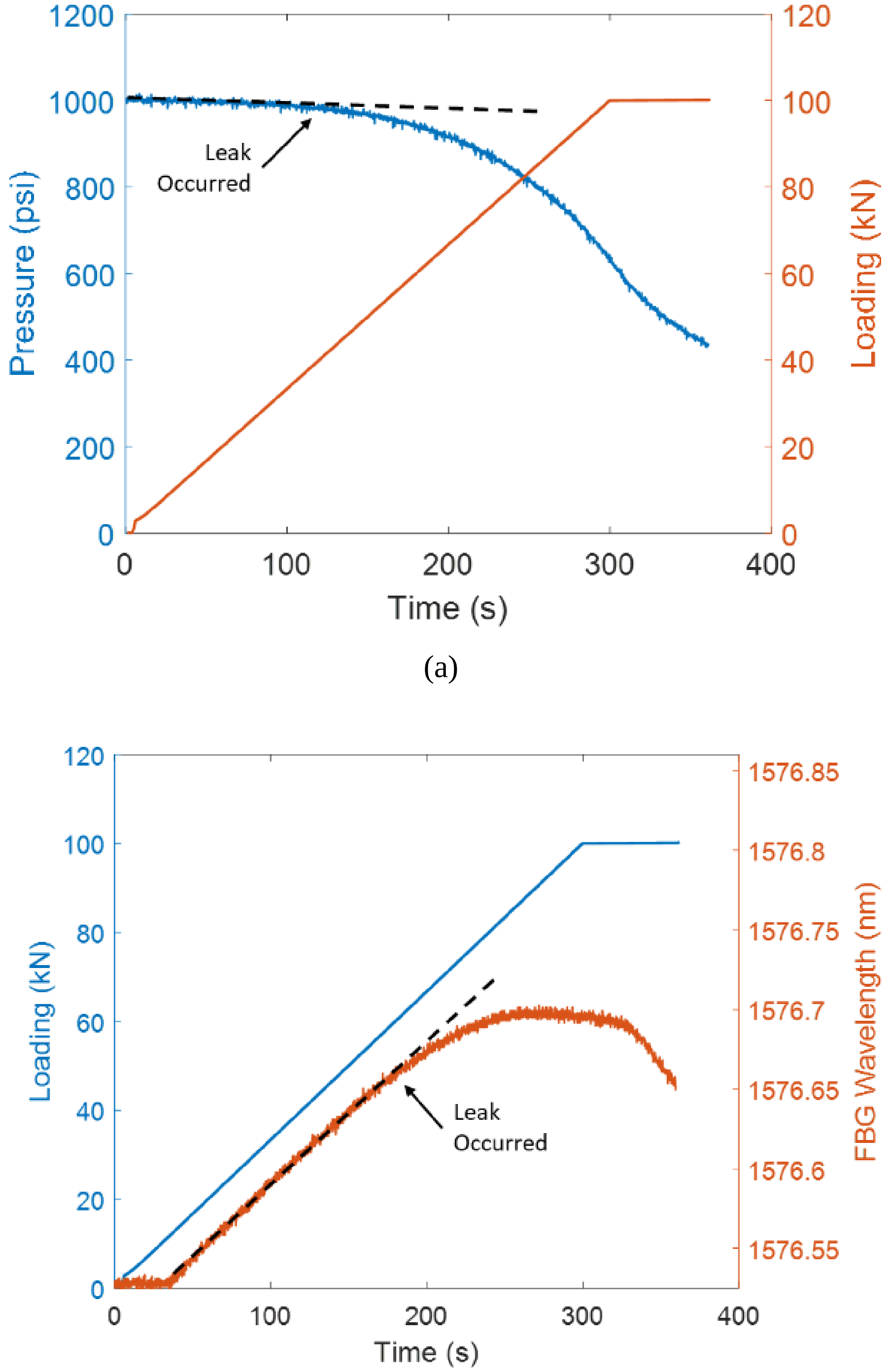

(a)

(b)

Figure 5-24 Leak-related tension test results of the bolted flange joint under tightened torque of 20 ft-lb (a) internal pressure and (b) FBG strains

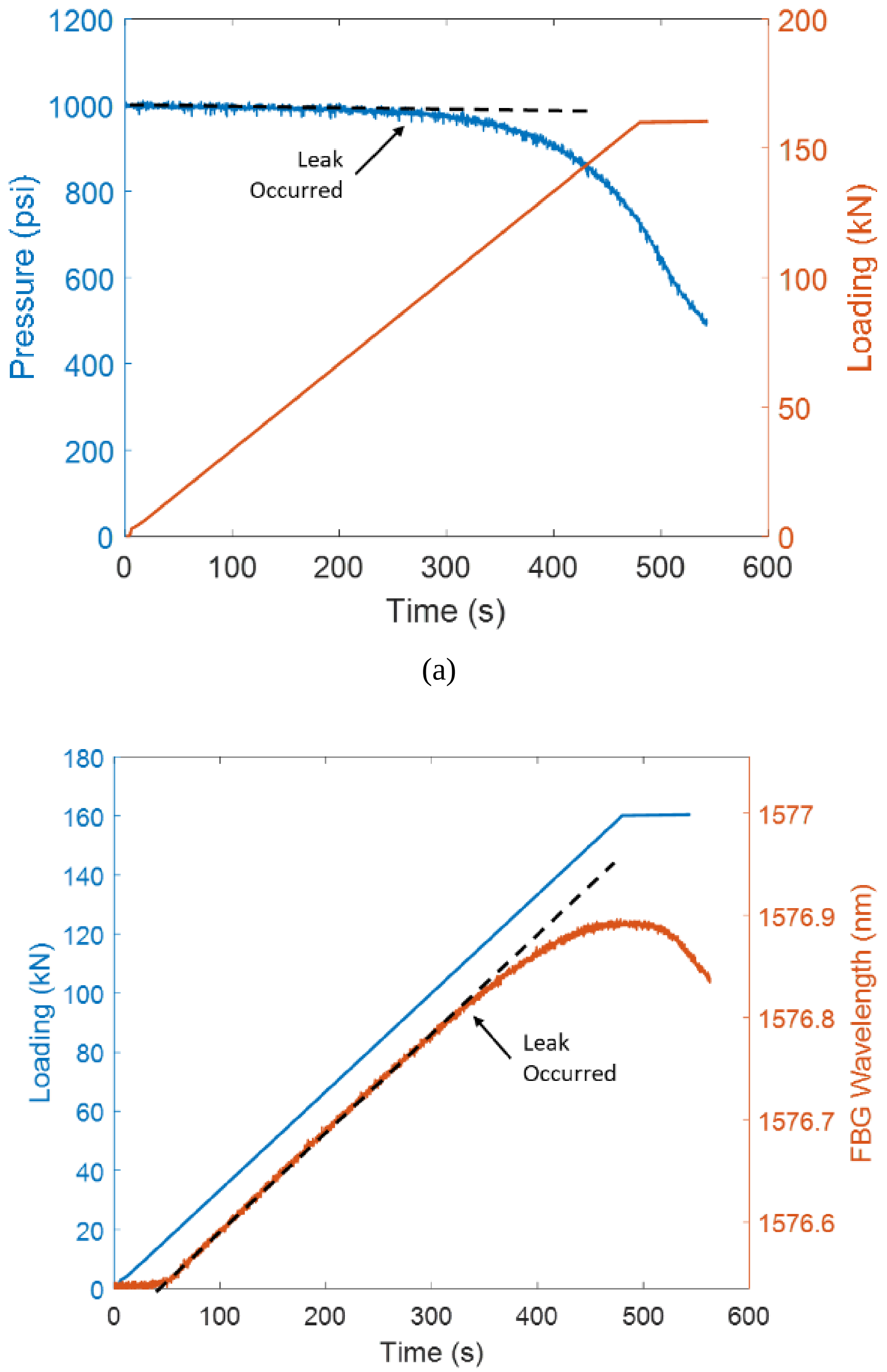

(a)

(b)

Figure 5-25 Leak-related tension test results of the bolted flange joint under tightened torque of 25 ft-lb (a) internal pressure and (b) FBG strains

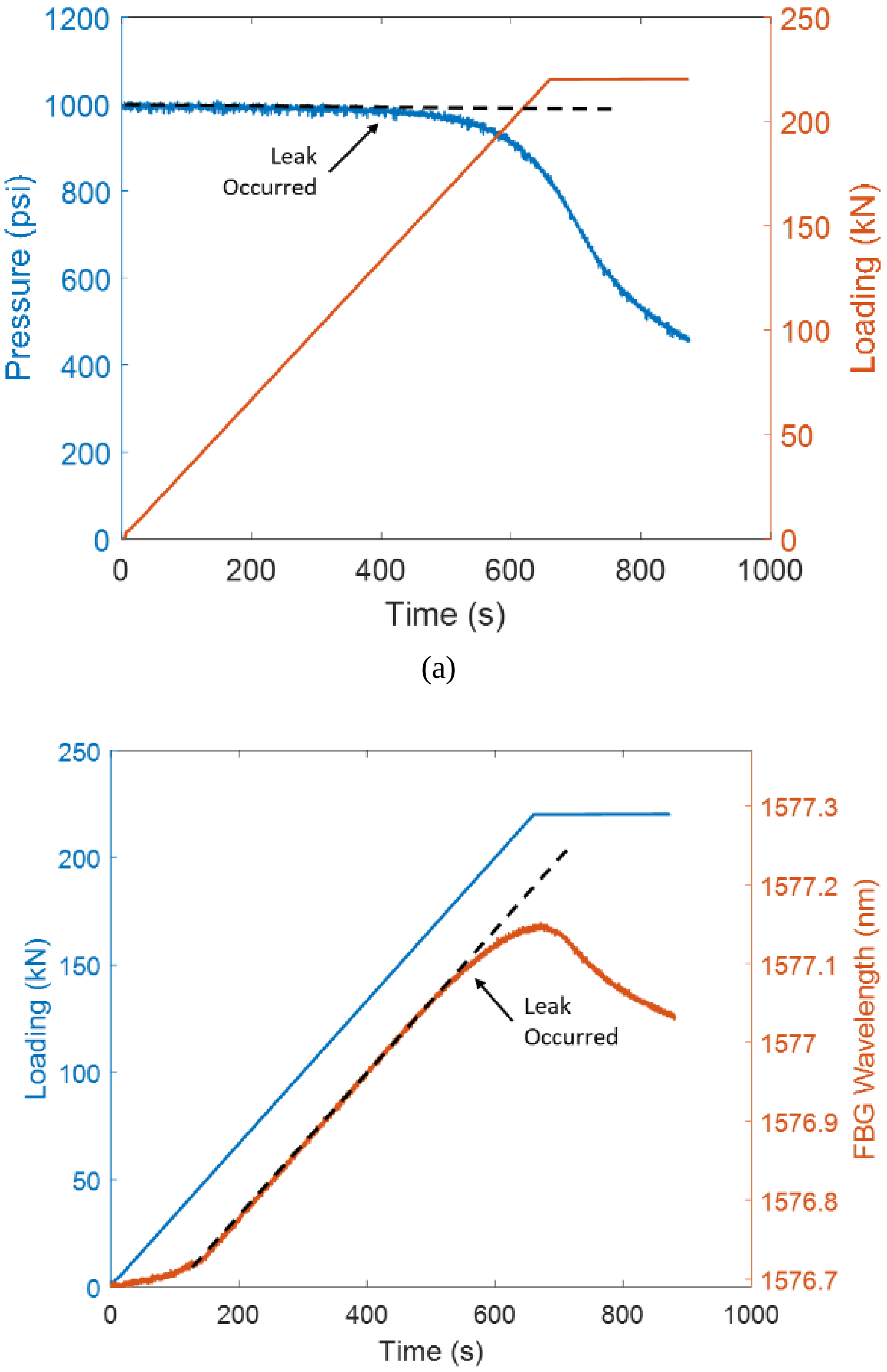

(a)

(b)

Figure 5-26 Leak-related tension test results of the bolted flange joint under tightened torque of 30 ft-lb (a) internal pressure and (b) FBG strains

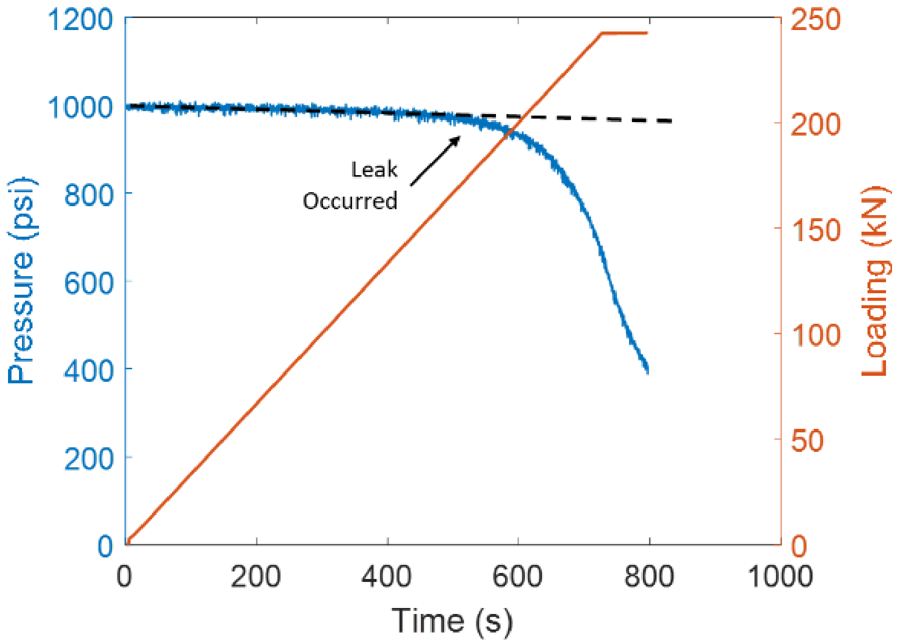

(a)

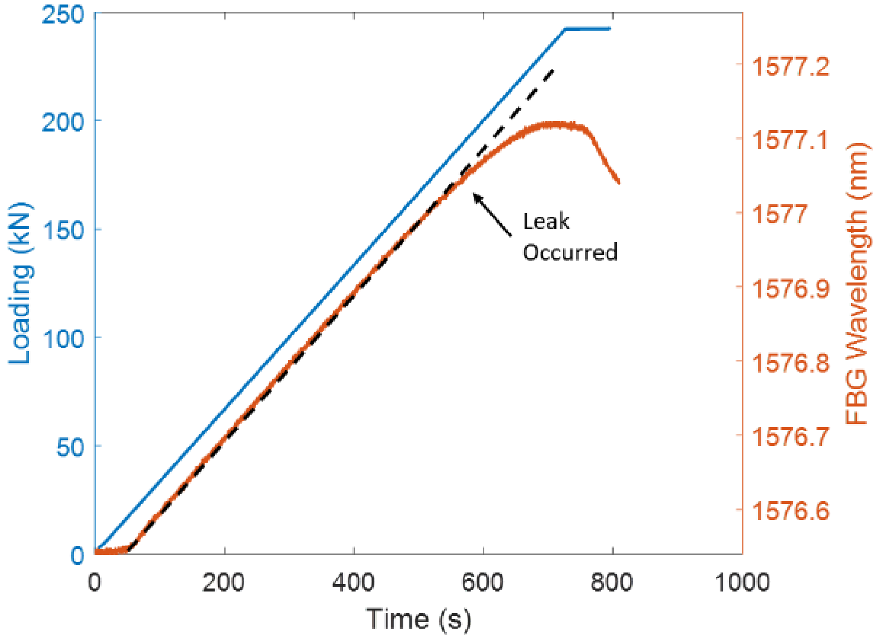

(b)

Figure 5-27 Leak-related tension test results of the bolted flange joint under tightening torque of 35 ft-lb (a) internal pressure and (b) FBG strains

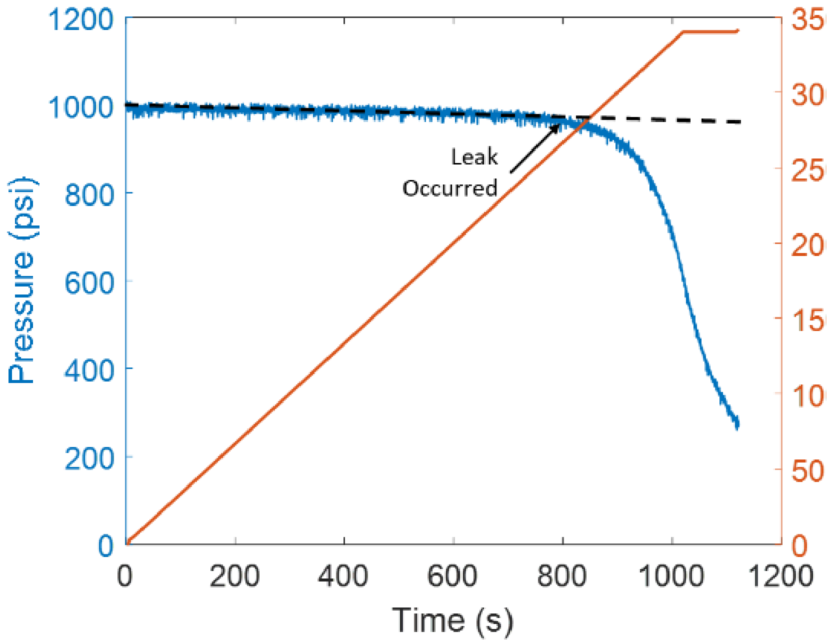

(a)

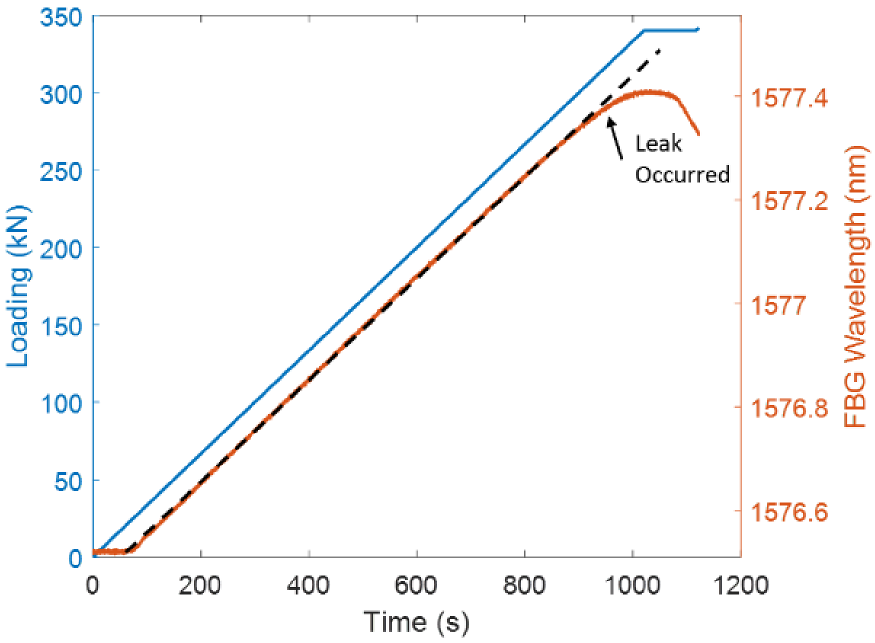

(b)

Figure 5-28 Leak-related tension test results of the bolted flange joint under tightening torque of 40 ft-lb (a) internal pressure and (b) FBG strains

Table 5-5 Summary of leak-related tensile loads based on the results of internal pressure and FBG enable strain monitoring on bolts

| Torque (ft-lb) | Leak -related Tensile Loads (kN) | | | | |
|---|---|---|---|---|---|
| | Test-1 | | Test-2 | | Average |
| | FBG Strain | Pressure | FBG Strain | Pressure | |
| 20.00 | 58.74 | 54.07 | 57.97 | 53.65 | 56.11 |
| 25.00 | 111.40 | 114.30 | 108.30 | 101.20 | 108.80 |
| 30.00 | 172.70 | 164.10 | 157.10 | 151.50 | 161.35 |
| 35.00 | 193.70 | 192.40 | 179.20 | 176.20 | 185.38 |
| 40.00 | 271.10 | 274.40 | 263.80 | 271.60 | 270.23 |

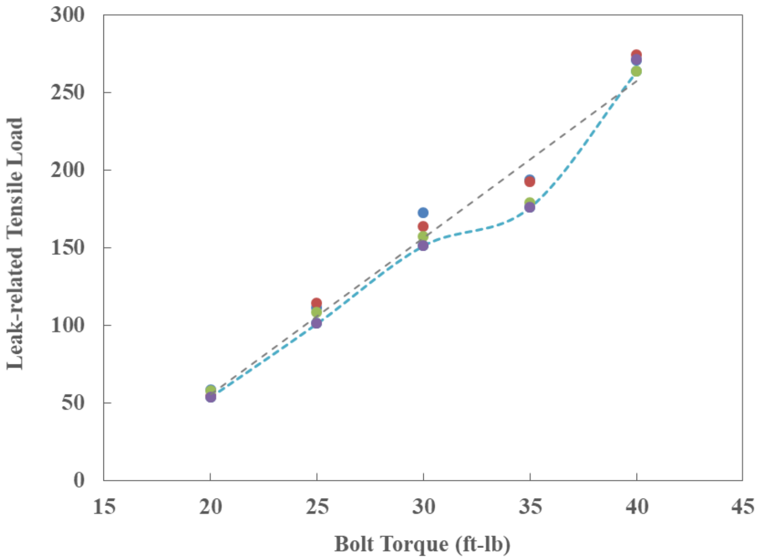

Figure 5-29 Relationship between the bolt torques and the leak-related tensile loads

## 5.4 Summary

In this chapter, the bolted flange assembly was installed on the MTS test frame to perform a thorough integrity investigation of the flange connection under the tensile loads and combined tensile and internal pressure loads based on the proposed comprehensive monitoring system. The characteristic variations of the flange connection under the tensile loads and combined tensile and internal pressure loads were both studied by the piezo-based active sensing method and electromechanical impedance measurement. In addition, the real-time monitoring of FBG enabled bolt strain, internal pressure and AE acoustics enabled to detect and identify the leakage failures of the flange connections subjected to the increasing tensile and internal pressure loads. Furthermore, the leak-related tension limits were preliminarily obtained under a variety of tightened torques on the bolts, which offered a useful leakage failure envelope to potentially mitigate the future failures of the flange connections in the field.

# 6. A Touch-enabled Inspection Approach for Subsea Bolted Connections

## 6.1 Introduction

Monitoring of bolted connections on land has been received much attention, however, few literature can be found on the same topic in subsea environment. Due to the harsh subsea environment, most of the aforementioned methods cannot be directly applied to the subsea bolt monitoring. The transition of these methods to the subsea situation needs further research. Among the reviewed bolted connection monitoring methods on land, the PZT-based approaches hold a great promise because of the advantages, such as small size, light-weight, cost-effectiveness, and robustness. However, the typical PZT based methods require permanent installation of transducers onto or near the bolted connections, which may be difficult for subsea applications. Therefore, an approach to inspecting bolt connection without the permanent installation of PZT transducers should be developed. Since stress waves can be transmitted upon touching or contact, it is possible to integrate PZT transducers with the fingers of a robotic manipulator to enable the touch-based active sensing method for bolted connection inspection. Considering the difficulty of accessing subsea pipelines by human divers, this potential monitoring or inspection method shall be easily integrated with a subsea robotic system, such as a remotely operated vehicle (ROV), for the further development of this subsea inspection system.

Therefore, the objective of this chapter is to develop a touch-enabled bolted connection inspection approach that can be easily integrated with a robotic system without the requirement of permanent installation of sensors. In this chapter, an active sensing approach using PZT transducers mounted on a proof-of-concept clamping device that mimics two robotic fingers is designed and investigated for inspecting bolt connections. Basically, the tip of each robotic finger is equipped a flat PZT patch transducer. The clamping mechanism also uses magnets that help to secure a temporary and effective coupling between the transducers and the both surfaces of the bolt connection, such as a flange. Upon touching, one PZT transducer mounted on one end of clamping device generates stress waves that propagate across the connection interface, and the other PZT transducer mounted on the other end of the clamp detects the propagating stress wave. Experimental studies are carried out in this research to validate the feasibility of the proposed approach. Experimental investigations demonstrate that the proposed approach has the advantages of non-invasiveness, ease of use and effective coupling, allowing the touch-enabled active sensing for inspection of submerged bolted structures. The envisioned implementation of the proposed touch-enabled active sensing with a subsea robotic vehicle, such as a ROV for inspection of a subsea bolted connection is illustrated in Fig. 6-1.

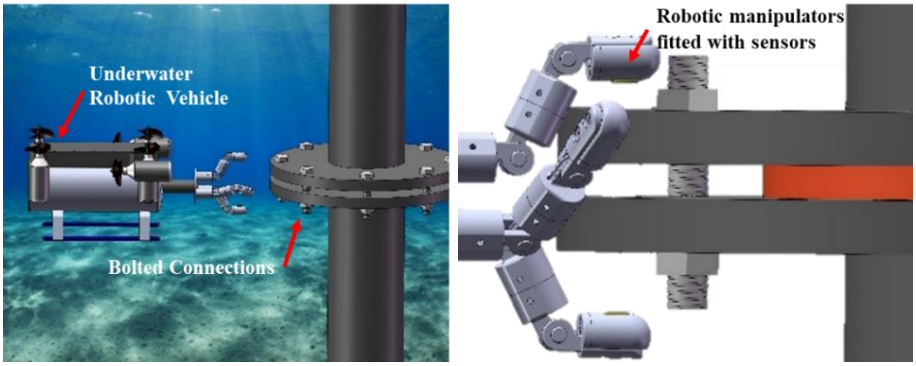

Figure 6-1 Envision of an underwater robotic vehicle incorporated with the piezo-based portable sensing approach for the inspection of subsea bolted connections.

## 6.2 Design for the Touch-enabled Sensing

Typically, the implementation of piezoceramic transducers for bolt connection monitoring requires the permanent installation of the transducers onto the target structure, and often a suitable adhesive (e.g., epoxy) is used to bond the transducers onto the structure. However, in some cases, where the working environment is harsh (e.g. high temperatures and high pressure in deep sea applications), the adhesive layer may be peeled off or the sensors may be deformed to such an extent that the sensor is destroyed. Overall, permanent bonding complicates monitoring applications in remote or harsh environments, especially for undersea applications.

In this chapter, a proof-of-concept clamp-on fixture is designed to enable the touch based active sensing using PZT transducers. The design is composed of a C-shaped steel fixture, a pair of linear ball bearings and sliding shafts, enabled PZT transducer assembly (Fig. 6-2), rubber pads, and permanent magnets, as shown in Fig. 6-3. The C-shape clamp design mimic a pair of robotic fingers whose surfaces are integrated with PZT transducers. In this C-shape clamp design, the bearing-shaft assembly with springs can be pulled back (effectively widening the “jaw” of the fixture) to accommodate different thicknesses of inspected structures. At the same time, the magnets constantly compress the transducers against the inspected structure and help to provide a uniform load distribution across the transducer-structure interface. The two layers of rubber pads help minimize the transmission of the actuator’s stress waves that may travel through the body of the fixture and towards the other transducer. The enabled transducer assembly was built by embedding a piezoelectric disc into a copper housing, which ensures the transducer housing is waterproofed. One side of the piezoelectric patch and the entire copper housing are grounded through one lead wire. The ungrounded side of the piezoelectric patch is isolated from the copper housing and is soldered to a lead wire. During each measurements, the proposed touch-based inspection device was properly clamp to the pre-drawn circular marker on the surface of the plates. This pre-drawn marker ensured the same location and secured a reliable measurement for each point-to-point inspection. The properties of PZT patch are listed in Table 6-1.

Table 6-1 Properties of PZT Transducers

| **Dimension** | **Density** | **Young's Modulus** | **Piezoelectric Coefficients** | | **Dielectric Coefficients** | |
|---|---|---|---|---|---|---|
| | | | $d_{31}, d_{32}$ | $d_{33}$ | $\varepsilon_{11}, \varepsilon_{22}$ | $\varepsilon_{33}$ |
| $\emptyset 15 \times 1$ mm | 7450 kg m$^{-3}$ | 46 Gpa | -185 pC/N | 720 pC/N | 0.151 nF/m | 660 nF/m |

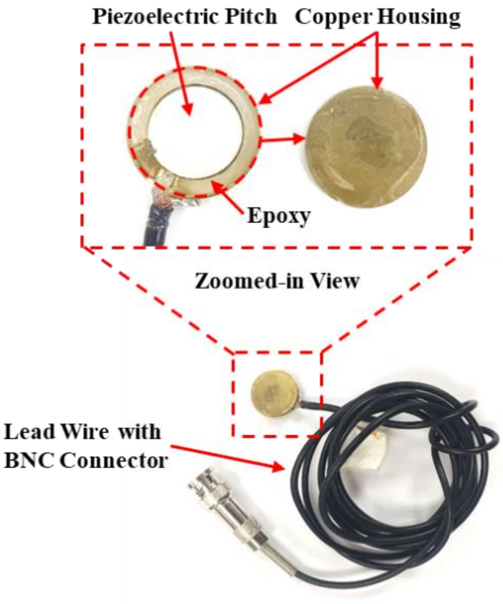

Figure 6-2 Configuration of an enabled PZT transducer assembly

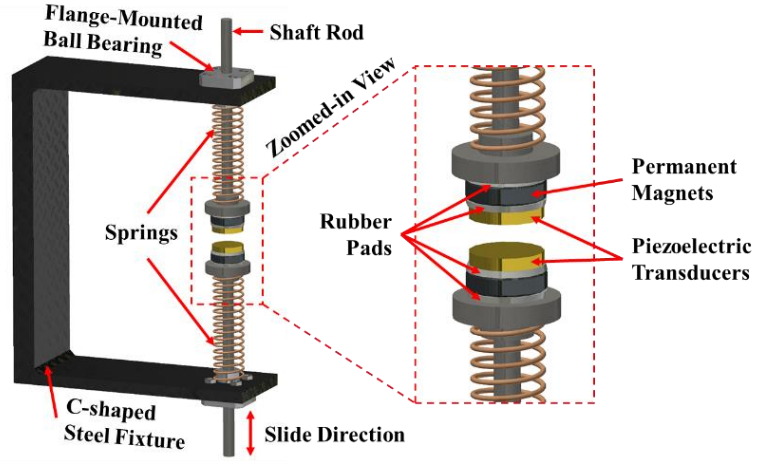

Figure 6-3 A proof-of-concept design of the touch-based sensing device

## 6.3 The Touch-enabled Active Sensing Method

In this chapter, the proposed touch-enabled inspection approach uses a portable version of the active sensing method to inspect two steel discs bolted together with a threaded rod and two nuts (see Section 4). During the experiments, one PZT transducer, acting as an actuator, upon touching, generates a stress wave that propagates across the bolted plates as stress waves. The stress waves are received at the second transducer, also through touching. The received signal strength and its corresponding signal energy correlates with the characteristics of the interface between the two plates, such as contact stress, interface profile and true contact area. In other words, any alterations in the characteristics of bolted plates interface can induce measurable changes in the received signal. Therefore, the status of the bolted connection can be inferred by comparing the features of the received signals at any instant to the measured baseline of the received signal.

## 6.4 Experimental Setup and Procedures

Two steel discs (diameter of 127.00 mm and thickness of 12.70 mm) with a steel threaded rod (7/8”-9 thread size, 6” long) and two nuts (7/8”-9 thread size) served as a target subject for inspection. After clamping the proof-of-concept clamp onto the discs, the two PZT transducers were in touch with the flange of two mating discs. One PZT transducer (actuator) generated a stress wave upon receiving an excitation signal and the other PZT transducer (senor) detected the propagated stress wave across the interface of the discs. The excitation signal (amplitude of 10 volts from 1 kHz to 350 kHz over 1 second) was generated by a DAQ board (National Instruments USB-6361) connected to a laptop (Fig. 6-4). The DAQ system continuously generated the signal every second during the experiment. The sensor signal was recorded every second after running the DAQ system with a sampling frequency of 2 MHz.

The bolted metal plates were tightened by a digital torque wrench (Craftsman 913918) from 0 to 50 ft-lb in increments of 10 ft-lb (1ft-lb = 1.356 N-m). As shown in Fig. 6-5, the same experimental procedure was repeated in air and in salt water. The salinity of the salt water was artificially made to be about 3.5%, which imitated the salt concentration of the sea water. Furthermore, ultrasonic couplant was applied at transducer-structure interface to enhance the transmission of signal across the interface between the sensors and the surface of the structure. For consistency, the ultrasonic couplant was applied for both air and underwater tests. Note that the active sensing method still performs well even when ultrasonic couplant is not applied; however without the couplant, the signal strength is relatively moderated.

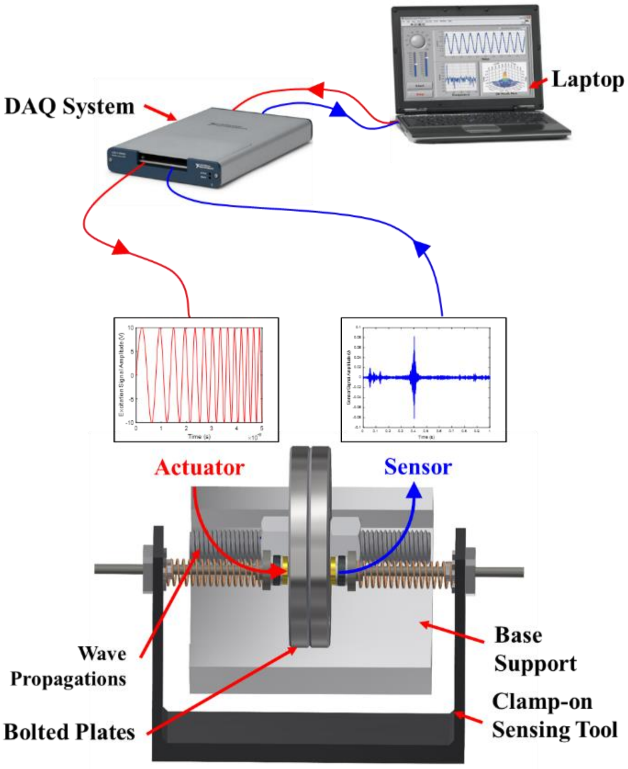

Figure 6-4 Method of active sensing measurement using the proposed touch-based inspection approach

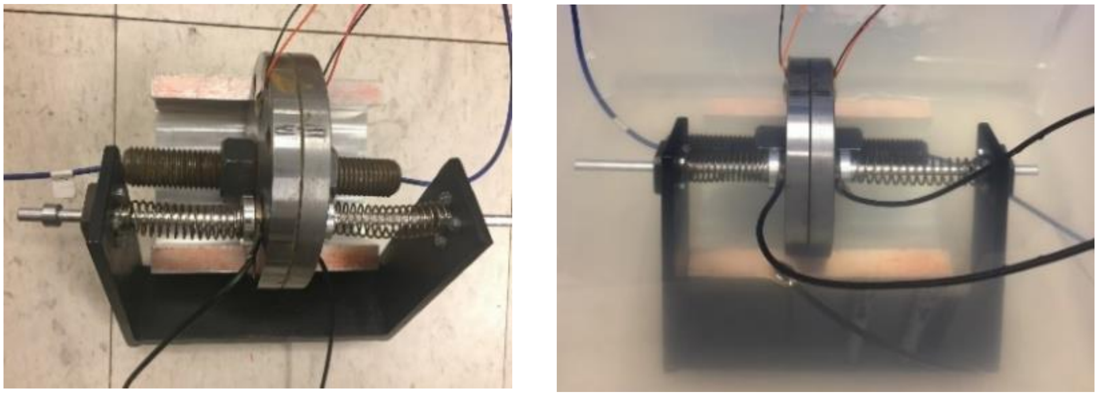
(a) (b)

Figure 6-5 Test specimen in different environments: (a) in air and (b) in salt water.

## 6.5 Results and Discussion

### 6.5.1 Time-domain Analysis of Active Sensing Results

In the experiment, the received signals were compared to a baseline, and thus deviations from the current received signal are indicative of changes in the inspected structure (e.g. changes in preload due to applied torque). When the inspection was conducted in air, the amplitude of the received signals increased with torques (Fig. 6-6). Once the entire experimental specimen was submerged in saltwater, a similar trend was observed (Fig. 6-7), however, the entire signal strength was diminished as compared with the signals in air. This phenomenon may be attributed to the stress wave attenuation caused by the surrounding saltwater. The stress wave cannot transmit in air, however it can propagate in salt water environment. Therefore, when the entire setup was merged in saltwater, the partial signal of stress wave could propagate from the specimen to the surrounding saltwater, thereby weakening the acquired signal strength from the sensor. However, the effect of the different torque on the signal strength still can be discerned. Therefore, the active sensing method, as demonstrated by the results in time domain, validates the effectiveness of the touch-based mechanism for piezo-based inspection for both dry and saline conditions.

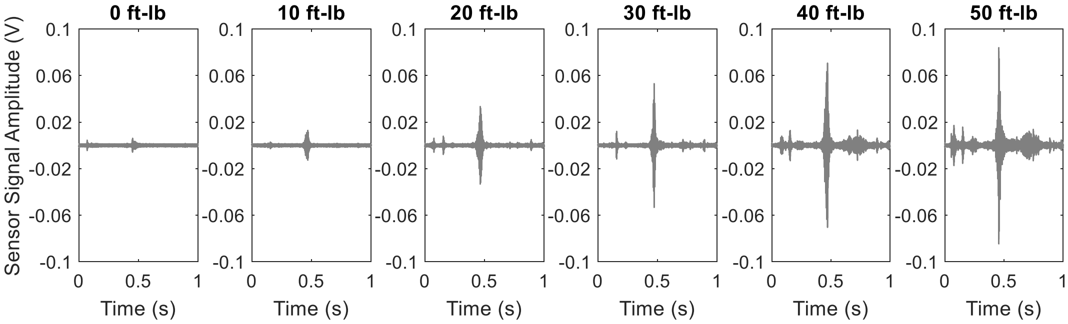

Figure 6-6 Time-domain active sensing responses in air

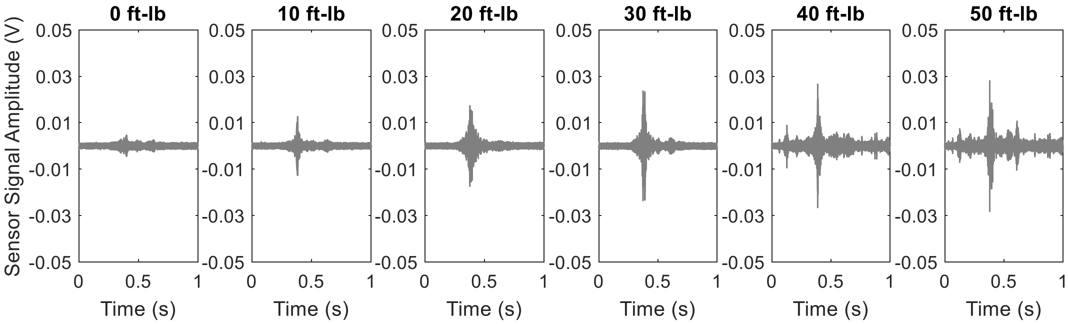

Figure 6-7 Time-domain active sensing responses in salt water

### 6.5.2 Spectral Analysis of Active Sensing Results

Time-frequency representations (i.e., spectrograms) of the received signals are shown in Fig. 6-8 and Fig. 6-9. The horizontal axis and the left vertical axis represent time and frequency, respectively. The power intensity of the signal across its spectrum is indicated by its colors (right vertical axis). The color changes from blue to red, indicating an increasing spectral power. In Figs. 6-8 and Fig. 6-9, since the frequency of the swept-sine wave shifts linearly from 1 kHz to 350 kHz within one second, the corresponding spectral distribution is concentrated around a diagonal line. The figures show that the spectral power increases as the applied torque changes from 0 ft-lb to 50 ft-lb (1ft-lb = 1.356 N-m) in air and in salt water. However, one pronounced difference is the first case with 0 ft-lb, where the in-saltwater results had higher intensity than for the in-air results. This difference can be attributed to the filling of the interfacial gap with saltwater, which facilitated stress wave propagation from one plate to another. Furthermore, the red spots in the spectrogram indicate the resonant frequencies of the bolted specimen when coupled with the PZT transducers, resulting in a horizontal line (constant frequency) pass across the spectrogram and intersecting at the red spot. This phenomenon can be clearly observed when the torque ranges between 10 ft-lb to 50 ft-lb (Fig 6-8). However, when the specimen is submerged in saltwater, this phenomenon is visible when the applied torque reached beyond 40 ft-lb (Fig. 6-9). Moreover, the stiffness of the entire bolted structure increases under the higher applied torque, as a result, can induce a higher mode of structural resonant frequencies. As shown in Fig. 6-8 and Fig. 6-9, the second resonant frequency (another red spot) is excited when the torque changes from 30 ft-lb to 40 ft-lb and its corresponding spectral intensity is further enhanced till the applied torque of 50 ft-lb Therefore, spectrograms of the received signals can distinguish the status of the bolted specimen under different torques.

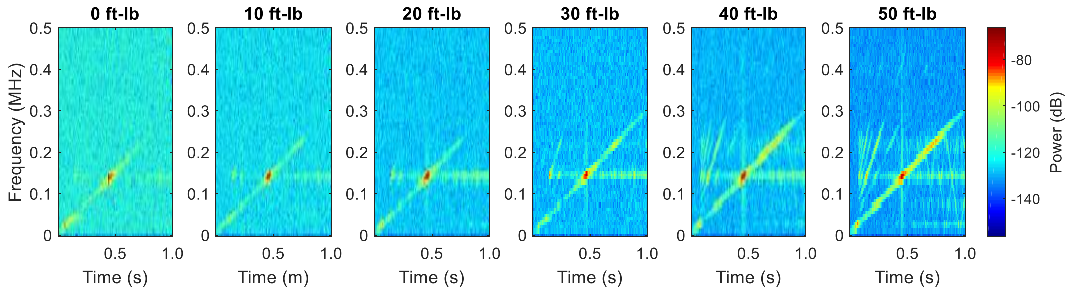

Figure 6-8 Spectrograms of active sensing results in air

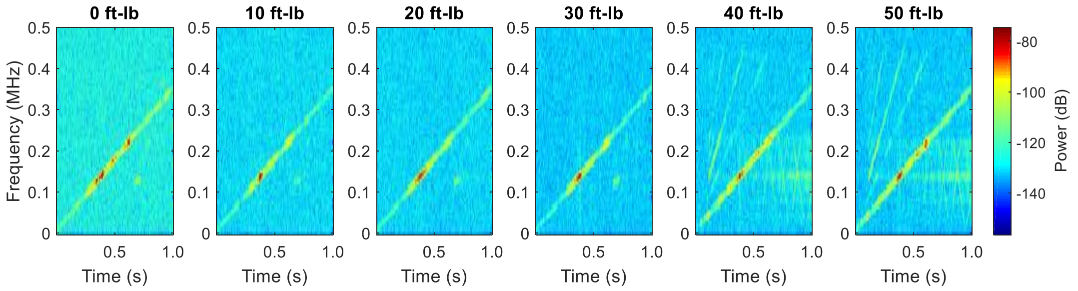

Figure 6-9 Spectrograms of active sensing results in saltwater

### 6.5.3 Results of Wavelet Packet-based Energy Method

To further analyze the results from active sensing results, the wavelet packet transform method was used to evaluate the total signal energies for the different cases. The WPT based energy indexes for three tests of each case, in air and in saltwater, are computed and plotted in Fig. 6-10 (a) and (b), respectively. In Fig. 6-10 (a), the WPT based signal energy exhibits a growing trend according to the incrementally applied torque, and an upsurge of the signal energy occurs when the torque changes from 10 ft-lb to 30 ft-lb and from 30 ft-lb to 40 ft-lb (1ft-lb = 1.356 N-m) for the measurements in air. When the specimen was submerged in saline water, the energy indices follow a smooth and upward trend with increasing torque applied on the bolted plates, as shown in Fig. 6-10 (b). Additionally, the WPT based signal energy of each case indicates a good agreement with active sensing results, and further demonstrates a correlation between the tightness of the bolted plates. Thus, the WPT energy index shows a valid, alternative way to quantitatively differentiate the status of a bolted connection when the bolted connection subjected to different applied torques.

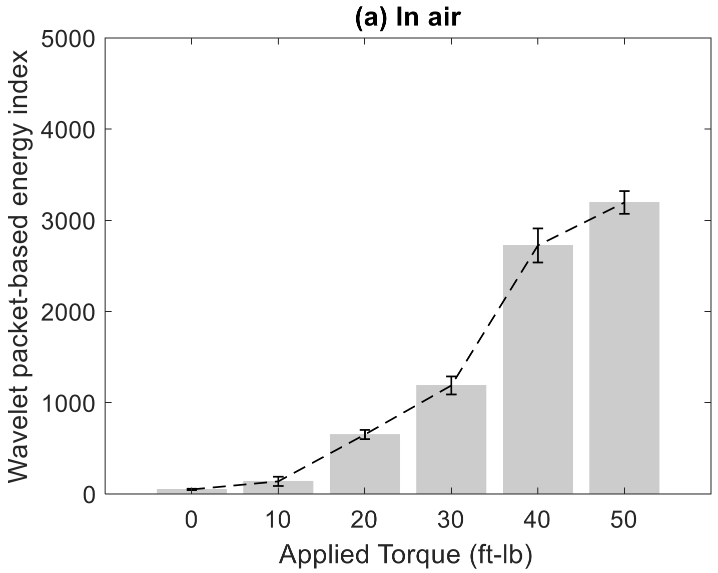

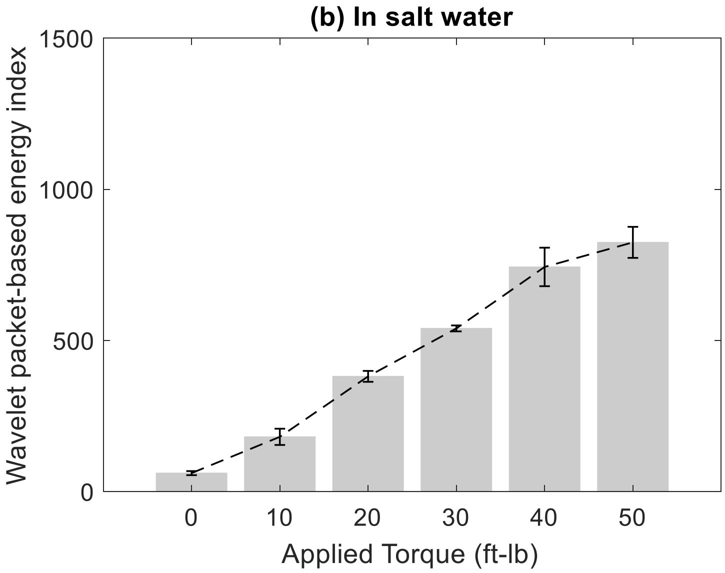

Figure 6-10 Results of wavelet packet-based energy index (a) in air, (b) in salt water.

## 6.6 Summary

Despite the availability of many monitoring or inspection methods, there is still a need for a new design that can rapidly, effectively and non-invasively inspect the integrity of subsea bolted connections. In this research, a touch based active sensing approach enabled by PZT (Lead Zirconate Titanate) transducer is proposed to inspect subsea bolted connections without the need of permanent installation of sensors on the structures. The proposed touch-enabled sensing method transforms piezoceramic based monitoring techniques into conveniently portable and reusable inspection methods that can be easily integrated with a subsea robotic system, such as a remotely operated vehicle (ROV). For the feasibility study, in this chapter, the proposed approach using PZT transducers mounted on a proof-of-concept C-shaped clamping device that mimics two robotic fingers is designed and investigated for inspecting bolt connections. Two PZT patch transducers are mounted on the fingertips of the two mimicked robotic fingers. To help to secure an effective coupling between the PZT transducers and the surfaces of the bolt connection upon touch, a pair of permanent magnets are used in the clamping mechanism. This design enables the touch based active sensing for bolt connection inspection. Upon touching, one PZT transducer generates stress waves that propagate across the connection interface, and the other PZT transducer detects the propagating stress wave. With the proposed method, inspection of a bolted connection of different pre-loads in both air and salt water is carried out. Experimental results illustrate a clear correlation between the magnitude of the received time-domain signals from the PZT sensor and the level of applied torque for the bolt connection in both air and in saltwater. The spectrograms also visualize the effects of applied torque on changes of spectral power and resonant frequencies. Furthermore, the results from the wavelet packet transformation (WPT) -based energy agree well with the active sensing results, and is able to clearly track the change in the applied torque of the bolt connection in the two test environments. Therefore, three methods of analyzing the results in different views thoroughly demonstrate the effectiveness of the proposed touch-based approach. In future, impedance-based health monitoring approach will be further investigated for the inspection performance of the proposed touch-based inspection method. Furthermore, we will design a more advanced touch-based inspection device that accommodates higher degrees of freedom and can be mounted onto a remotely operated vehicle for inspecting bolted structures in a real subsea environment.

# 7. Remotely Operated Vehicle (ROV) Assisted Robotic Inspection for Undersea Bolted Connections

## 7.1 Introduction

Pipeline systems are essential infrastructures for delivering oil and natural gas from the onshore/offshore reservoirs to markets [5]. However, over the past 20 years, more than 334 fatalities and $7 billion losses due to 11,769 pipeline accidents were reported. Investigations reveal that failures from bolted connections directly cause pipeline production shutdown and leakages induce serious environmental issues, especially in subsea environment. Therefore, the integrity monitoring of the offshore pipeline system has been drawn more attention. However, a regular monitoring system, requiring a permanent mounting condition of transducers onto the host structure, can be challengeable in subsea applications due to the harsh environment and remote location [15]. The primary issue is that the bonding interface between the transducers and the inspected structures can hardly be secured in deep water over time, which adversely affect the measurements. Therefore, a desirable sensing method in subsea environment is envisioned to conducting a remote inspection without requiring a permanent bonding of sensing devices.

To avoid the permanent bonding condition between the transducer and the inspected structure, a touch-based sensing device using a pair of PZT transducers have been proposed and studied in air and in salt water [116]. The touch-based sensing device utilized magnetic forces to provide a temporary and effective coupling condition between the transducers and the bolted specimen. To further expand the touch-based inspection method to undersea environment in this chapter, an undersea ROV with a manipulator is leveraged to improve its inspection capacity of a remote undersea inspection, which has not been explored yet. Therefore, the main objective of this chapter is to design a robotic manipulator equipped with a pair of PZT transducers and assemble with an underwater ROV device to function as a remote inspection system for subsea bolted connections. The undersea operation of the ROV and the robotic manipulator can be remotely controlled. Furthermore, this proposed ROV-enabled robotic inspection method is evaluated through a field test for remotely inspection of a bolted structure in local marine environment.

## 7.2 Characterization of ROV-enabled Undersea Robotic Inspection

### 7.2.1 Waterproof Design of Piezoceramic Transducers

The piezoceramic effect enables PZT material to function as actuators or sensors, which allow that piezoceramic transducers have been wildly utilized in structural health monitoring applications. However, the most implementations are to adhesively bond the piezoceramic transducers onto the host structure. This permanent coupling method is impractical to perform the remote measurements in deep sea applications. To expand the breadth of piezoceramic transducer’s application undersea, the piezoceramic transducer assembly is designed to be waterproof through embedding a circular-shaped piezoceramic patch in a copper housing, as shown in Fig. 7-1. The dimension and properties of PZT patch are listed in Table 6-1.

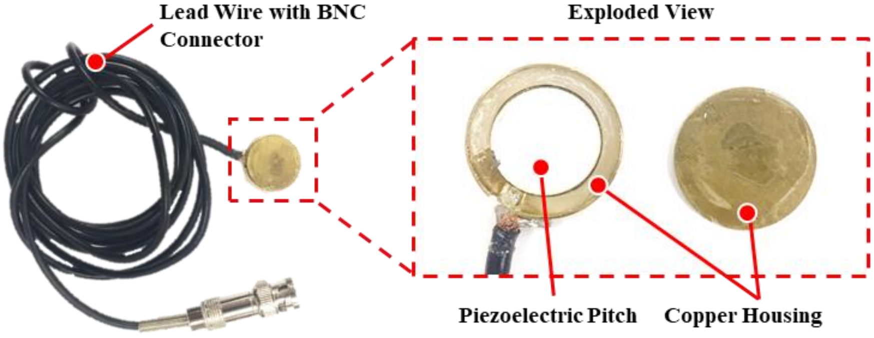

Figure 7-1 Configuration of an enabled piezoceramic transducer

### 7.2.2 Touch-enabled Sensing Design of a Manipulator Model

The portable coupling mechanism, compressing the transducer on the host structure surface with a uniform magnetic force, has been verified in the previous study. The previous reliable measurements in laboratory stimulate an advanced development of the inspection tool design from a manually operated C-shaped device to a linear actuator operated manipulator model. As shown in Fig. 7-2(a), this new design features a one-degree-freedom manipulator, integrated with the piezoceramic transducers, allowing to adjust the clamping width to accommodate the inspected objects via a remote control. The cutaway view, as shown in Fig.7-2(b), clearly illustrates that the piezoceramic transducers are bonded with rubber pads and a permanent magnet. The rubber pads can attenuate the actuated signal from the back side of the manipulator to minimize the impact on the sensor to acquire the stress waves. The permanent magnet provides a constant and uniform compression force to hold the transducer against the host structure as well as providing an effective coupling between the transducer and object. The bearing-shaft assembly offers a smooth movement of the transducer part. In addition, a certain path of the shaft is limited by a shaft collar, which also indicates the user properly operate the linear actuator once the transducers approaches the inspected object.

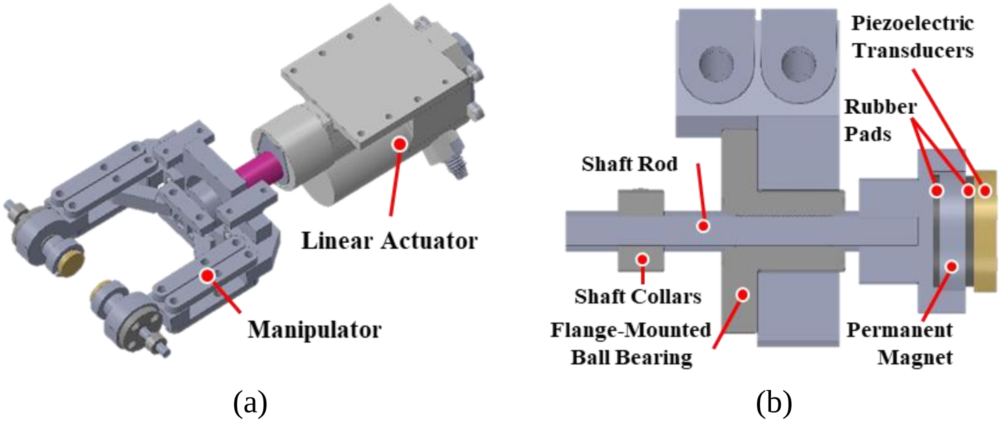

(a) (b)

Figure 7-2 Design of a robotic sensing manipulator: (a) a manipulator integrated with piezoceramic transducers; (b) a cutaway view of the transducer assembly.

### 7.2.3 Design of ROV-enabled Robotic Inspection Tool

ROV is one type of unmanned underwater robots/vehicles. It is typically tethered with an umbilical cable that allows the operator to stay in a safe place and to remotely operate the vehicle in a hazardous environment, such as undersea applications. The type of AC-ROV 100, developed by AC-CESS manufacturer, was used in this study, as shown in Fig. 7-3(a). This ROV is equipped with 4 horizontal and 2 vertical thrusters to enable 5 degrees of freedom underwater with the operation of a 3D hand controller. In addition, an integrated camera on the ROV device also provides a real-time underwater view through the onboard display. To achieve a remotely robotic inspection for the undersea bolted connections, a specifically designed manipulator coupled with piezoceramic transducers are fabricated and assembled with the ROV in this study, as shown in Fig. 7-3(b). The platform has total length of 332.10 mm, total height of 383.35 mm, and total width of 152.40 mm, as illustrated in Fig. 7-3(c). The workspace of the manipulator is 53.43 mm × 59.02 mm which is sufficient for inspection of the bolted specimen. During the undersea inspection, the ROV maneuvered the robotic manipulator to reach the target structure undersea. Furthermore, the onboard real-time display from the ROV's camera can assist the operator to adjust the propellers for aligning the manipulator and clamping the sensing assembly on the test specimen by the actuation controller of the manipulator.

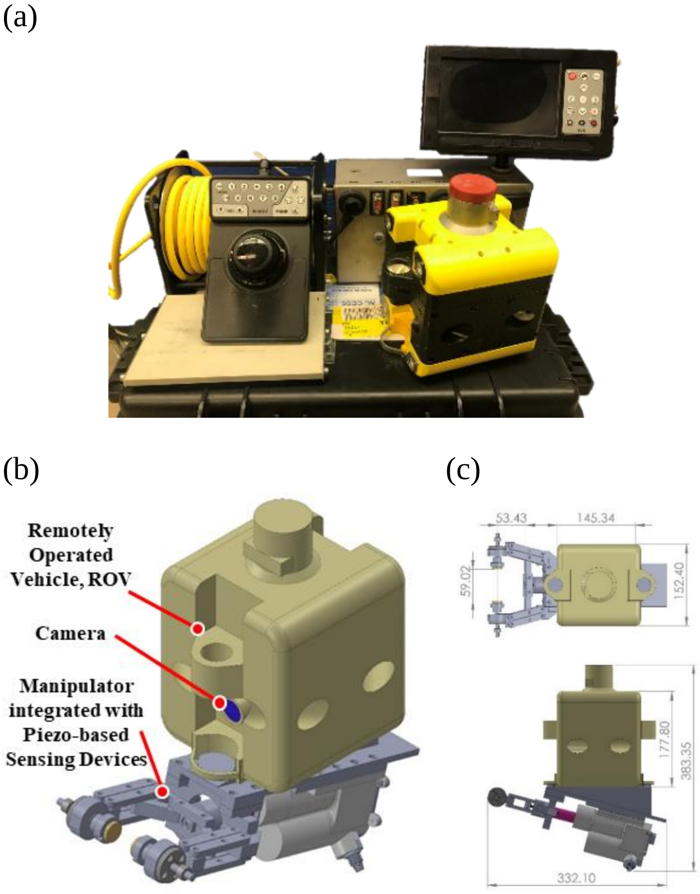

Figure 7-3 Illustration of the ROV enabled robotic inspection tool: (a) the ROV; (b) the integration of the ROV with the PZT-based sensing manipulator; (c) the main dimension of the entire ROV enabled robotic inspection tool.

## 7.3 Principles for Undersea Bolted Connections Inspection

### 7.3.1 Active Sensing Principle

To verify the effectiveness of the proposed ROV-enabled robotic inspection device, the piezo-based active sensing method is conducted on a bolted specimen, as illustrated in Fig. 7-4. The specimen is composed by two pieces of steel disks and four pairs of bolt-nut assemblies. Once the manipulator integrated with the piezoceramic transducers approaches the bolted connections through the operation of its controller, the transducers are held against the surface of the specimen through the magnetic force. There are one pair of the piezoceramic transducers on the manipulator model. During active sensing tests, one of the piezoceramic transducers is utilized as an actuator that can generate a linear swept-sine wave within a wide frequency range, while the other one acts as a sensor to acquire the signals through the data-acquisition (DAQ) system.

The strength of the acquired signal is directly correlated with the characteristics of the interface of two bolted steel disks. Higher preloads on bolts can induce more micro-contact or true contact area along the bolted-plate interface, which thus allows stronger propagation of the stress wave from the actuator to the sensor. In other words, any changes of the characteristics of bolted plates interface, such as interface profile and axial preload, can readily alter the acquired signal. Accordingly, the active sensing results (i.e., the energy or the frequency response of the signals) can be used to estimate the preload of the bolts as well as the integrity of the bolted connections. Thus, the PZT-based active sensing method is selected to evaluate the inspection performance of the proposed robotic inspection tool for exploring the status of the undersea bolted connections subjected to a series of different applied torques on the bolt-nut assemblies.

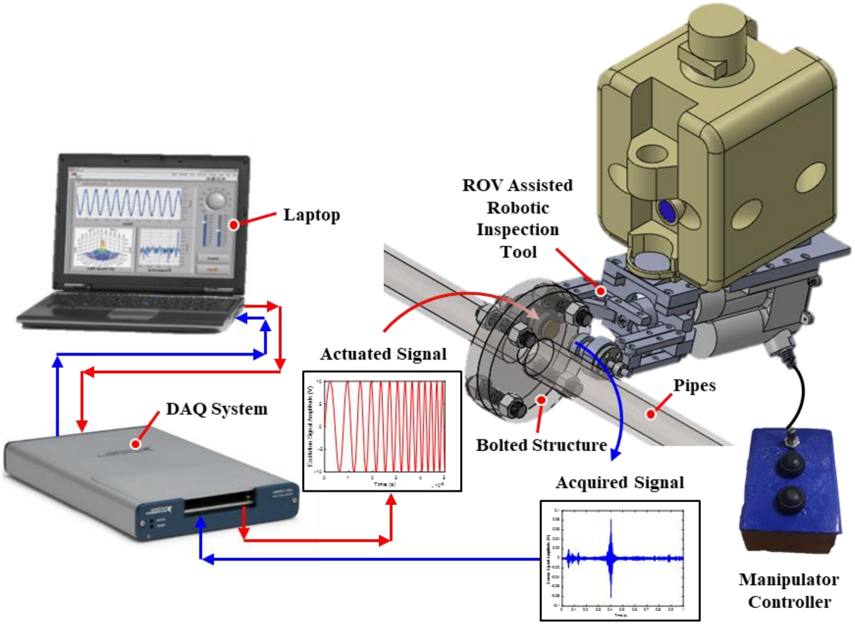

Figure 7-4 Illustration of the ROV-enabled robotic inspection principle

### 7.3.2 Spectrum Presentation Principle

Despite the time-domain responses of the acquired signal provides a fundamental insight of the system's characteristics, the spectrum of the response also further describes its characteristics in frequency domain. By applying Fourier transform, the frequency-domain representation of the acquired signal, $f(t)$, can be obtained to provide an alternative and useful view of the signal's properties. It primarily emphasizes the distribution of frequency changes over the frequency domain.

$$F(\omega)=\frac{1}{\sqrt{2\pi}}\int_{-\infty}^{+\infty} f(t)\cdot e^{-i\omega\tau}\,d\tau\ . \tag{7-1}$$

Then, the distribution of spectra, $P(\omega)$, over the frequency domain can be written as

$$P(\omega) = \left|F(\omega)\right|^2 = \left|\frac{1}{\sqrt{2\pi}}\int_{-\infty}^{+\infty} f(t) \cdot e^{-i\omega\tau} d\tau\right|^2 . \tag{7-2}$$

## 7.4 Undersea Test Setup and Procedures

The bolted specimen is composed by two piece of disk-shaped steel plates with diameter of 127.00 mm and the thickness of 12.70 mm with four bolt-nut assemblies. The entire bolted specimen is rigidly held on a PVC pipe for inspections. To prepare the field test of the proposed ROV-enabled robotic inspection tool, inspection procedures was first conducted in water tank in laboratory, as demonstrated in Fig. 7-5(a) and Fig. 7-5(b). During each measurements, the ROV was properly operated to approach the bolted plates and the manipulator actuated by its remote controller to clamp to the pre-drawn circular marker on the surface of the plates. This pre-drawn marker ensured the same location for each point-to-point inspection. A swept-sine signal with an amplitude of 10 volts and excitation frequency range from 1 kHz to 350 kHz in 1 second was generated by DAQ board (National Instruments USB-6361) via one of the piezoceramic transducers on the robotic sensing manipulator, while another transducer acquired the transmitted signals simultaneously at a sampling frequency of 2 MHz. To verify the effectiveness of this robotic sensing manipulator, the applied torque on the four sets of bolt-nut assemblies was altered from 0 to 20 ft-lb with 10 ft-lb increments through using a digital torque wrench, Craftsman 913918. The entire experimental set-up was submerge in sea water to conduct undersea inspection, as shown in Fig. 7-5 (c) and Fig. 7-5(d).

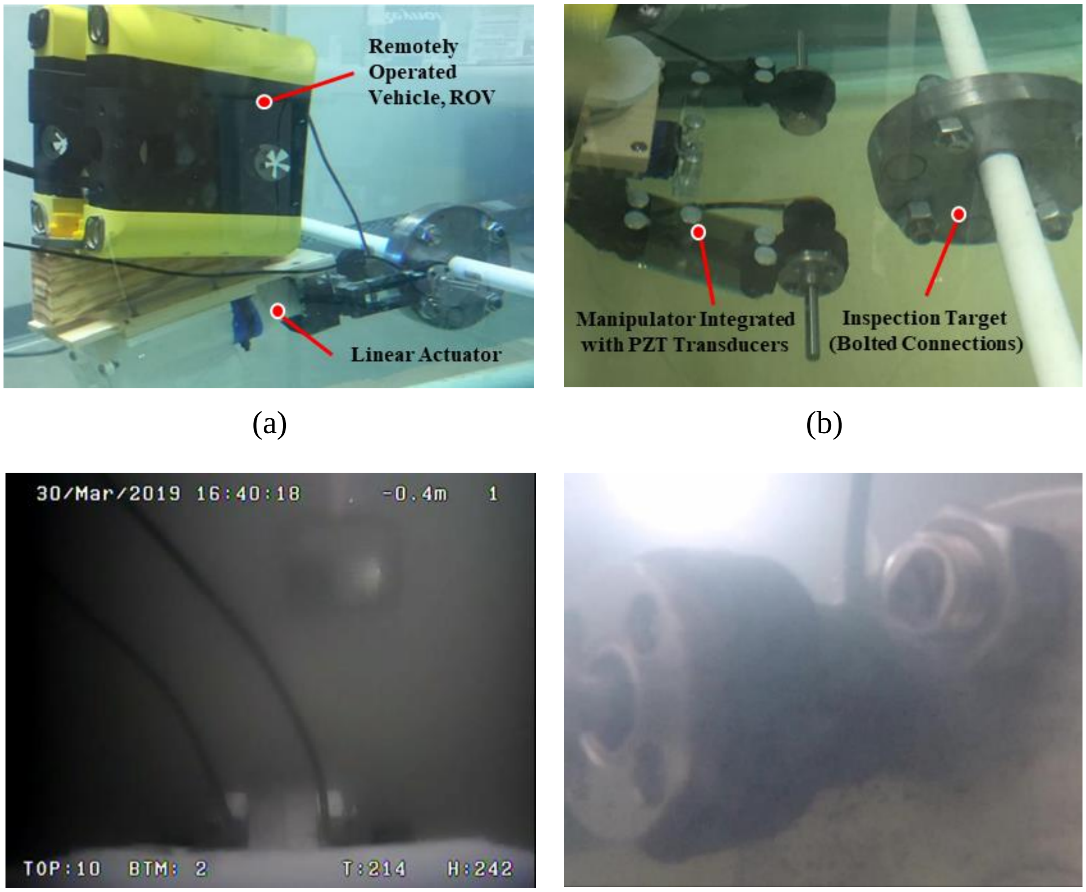

(a) (b)

(c) (d)

Figure 7-5 Experimental demonstration of bolted connection inspection: (a) and (b) in water tank in laboratory; (c) and (d) undersea tests in field

## 7.5 Undersea Test Results and Discussions

### 7.5.1 Time-domain Representations

It is noted that the inspection location on the bolted structure was the same and the magnetic contact fore for the transducers-structures interface was a constant. Additionally, a swept-sine wave signal was used as a reference input signal for each measurement. Therefore, the different applied torques on bolts could directly change the axial loads and contact characteristics of bolted plates as well as influencing the sensor's acquired signals. First of all, the distance of the piezoceramic transducers on the robotic manipulator was operated to be around the thickness of the bolted specimen and the active sensing measurement was performed on the transducers themselves to distinguish the signal difference in air and under sea water. The results, as shown in Fig. 7-6, show that sea water medium is applicable for wave transmission at certain distance. Subsequently, the proposed ROV enabled robotic inspection manipulator was employed to inspect the bolted specimen undersea in field. By comparing these received responses in time domain, it can be clearly illustrated that the distinction of signal strength when the bolts were subject to the different torque values. In other words, the dominant amplitude of the acquired signals is increased from 0.051 volts to 0.072 volts when the applied torque is from 0 ft-lb to 10 ft-lb. With one more increment of 10 ft-lb on the bolts, the corresponding signal amplitude rises to 0.082 volts. Therefore, undersea test results demonstrate that the time-domain responses effectively reflect the tightness of the bolts.

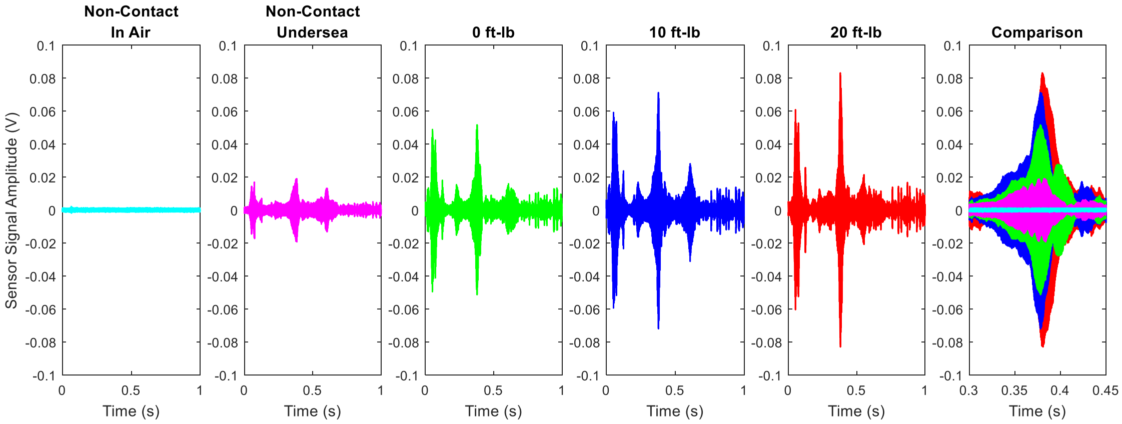

Figure 7-6 Time-domain response of undersea bolt inspection in field

### 7.5.2 Frequency-domain Representations

The frequency-domain response or spectrum of the acquired signal through the application of Fourier transform technique can offer an alternative insight of the signal characteristics, such as resonant frequency and spectral power. Generally, with a higher torque value applied on the bolts, the tightness can strengthen the mechanical property of the stiffness and thus increase the resonant frequencies of the entire bolted specimen. In this section, frequency-domain responses over the driving frequency range, from 1 kHz to 350 kHz, was obtained from the acquired time-domain signal from the active sensing measurements. The corresponding results are illustrated in a 3-D plot in the Fig. 7-7(a). The dominant frequency and spectral power are zoomed in frequency range of 120 kHz to 150 kHz, as shown in the Fig. 7-7(b). It is clear that the dominant resonant frequency is 132.3 kHz, 132.9 kHz and 133.8 kHz and the corresponding spectral power is $1.33\times10^{-8}$, $2.67\times10^{-8}$ and $3.96\times10^{-8}$ under the applied torque of 0 ft-lb, 10 ft-lb and 20 ft-lb (1ft-lb = 1.356 N-m) on the bolts, respectively. The spectrum representations indicate that both the resonant frequency and the spectral power were enhanced with increasing torque values on the bolted plates. Therefore, the spectrum of the acquired signal can provide two key parameters, modal frequency and the spectral strength, which can be straightforwardly utilized to indicate the tightness of the undersea bolted structure.

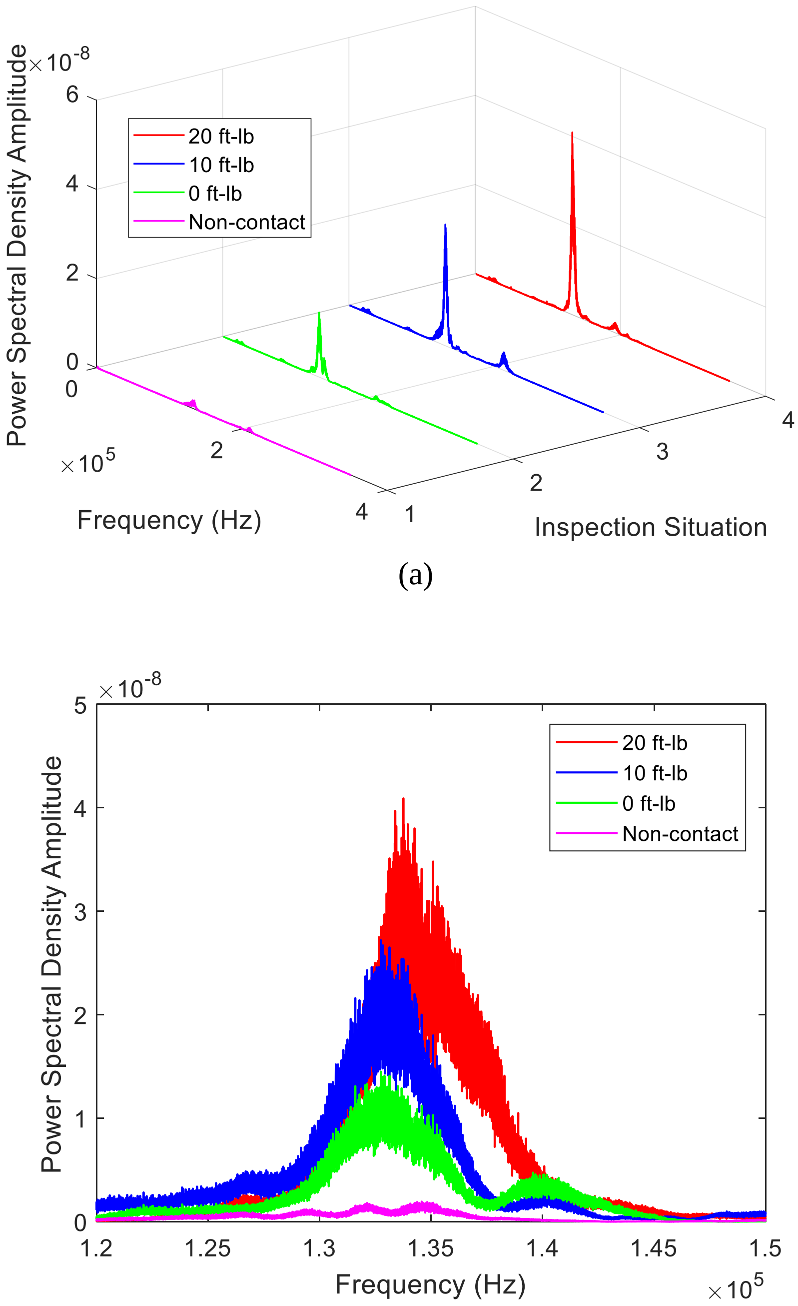

(a)

(b)

Figure 7-7 Frequency-domain response of undersea bolt inspection in field: (a) the comparison in 3-D view; (b) the comparison in zoomed-in view

### 7.5.3 Wavelet Packet Transform-based Energy Results

The wavelet packet transform-based energy of the acquired signals has been further explored to represent the status of the subsea bolted structure under different torques on the bolt-nut assemblies. During the computational procedures, the selection of decommission level was determined by the sensitivity analysis of the results and computational efficiency. Therefore, the original acquired time-domain signal was decomposed into 5th level with 32 sets of wavelet packet components in a way that the total WPT-based signal energy was computed through the summation of each component's energy, as described in Section 2.1.2. The derived results enable an adequate precision of the signal energy. As illustrated in Fig. 7-8, the WPT-based energy results of the transducers themselves with a certain distance verifies that sea water media can assist the transmission of stress waves rather than the corresponding measurement in air. For the ROV-enabled robotic inspection of undersea bolted connections under different values of torques, 0 ft-lb, 10ft-lb and 20 ft-lb, the corresponding WP-based energy index results are $1.2\times10^4$, $2.09\times10^4$ and $2.25\times10^4$, respectively. The increasing trend indicates the tightness level of the bolted plates associated with the applied torques or axial load on the bolts. Therefore, the proposed wavelet packed method-based energy can quantitatively distinguish the status of the subsea bolted connections by using the acquired signal from the proposed ROV-enabled robotic sensing measurements in field.

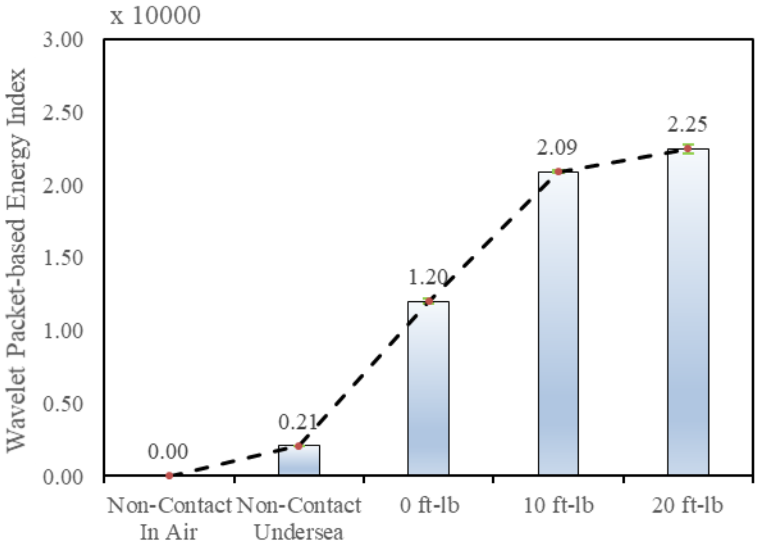

Figure 7-8 Wavelet packet transform-based energy index of undersea bolt inspection

## 7.6 Summary

Pipeline infrastructures play a dominant role to support the development of oil and gas industry. However, the bolt and connector failure has been a major issue in practical applications, especially for subsea pipeline system. These bolt-related failures can immediately cause leakages of contents and serious environmental issues. To minimize bolt failures, a desired inspection method of subsea applications is expected to remotely conducting an undersea inspection. To achieve this goal, a ROV enabled undersea robotic inspection is proposed and evaluated in undersea operating environment. In this chapter, a robotic sensing manipulator model was proposed and designed. The fingertip of the manipulator was integrated with piezoceramic transducers to function as a sensing manipulator. The design allows to adjust the clamping width to accommodate the different inspected objects through the remote operation. Furthermore, an underwater ROV has been utilized to incorporate the proposed robotic sensing manipulator to fulfill a remote inspection goal for undersea bolted connections. To evaluate the inspection performance of the proposed ROV-enabled remote undersea inspection method, a field test was conducted in Galveston Island for inspecting the status of the bolted specimen associated with different sets of applied torques. A swept-sine wave based active sensing method was conducted on ROV-enabled robotic inspection tool for undersea inspection. The field test data were analyzed in time domain and frequency domain. The acquired signal's amplitude in time domain and the corresponding WPT-based energy index show an increasing trend under a higher torque on the bolts. In addition, frequency-domain responses clearly illustrate that the tightness level of the bolts through spectral power values and the corresponding resonant frequency. Therefore, the undersea field test demonstrated the effectiveness of the proposed ROV-enabled remote undersea inspection method for undersea bolted connections.

# 8. Conclusions and Future Work

In this dissertation, a comprehensive integrity monitoring system is proposed and developed through the implementation of cutting-edge sensing technologies to thoroughly investigate the integrity of a bolted flange assembly under different conditions, including tensile loads and internal pressure. The integrity monitoring system include piezo-based active sensing method, electromechanical impedance (EMI) measurement, Fiber Bragg Gratings (FBG) enabled bolt strain monitoring, AE leak detection system and internal pressure monitoring system. To conduct and demonstrate the proposed research, a pair of API 6A flanges (4-1/16", Type 6B, 2000 psi) were selected. The piezo-based electromechanical impedance technique was studied to monitor the characteristic changes over the ring gasket of bolted flange connection subjected to the internal pressure loads, including pressurization and depressurization process. A repeatability study reveals that a near-linear relationship between the resonant frequencies and the corresponding internal pressure, which verifies the effectiveness of the proposed piezo-based electromechanical impedance method in monitoring the pressure-induced variation on the bolted flange joint. In addition, pressure-induced leaks were also investigated and detected by implementing acoustic emission system, pressure transducer, and FBG-enabled smart bolts. The leak occurred around the ring gasket was artificially induced by injecting nitrogen gas. Results clearly illustrated that the FBG sensors measure the real-time strains of the bolts and reflect the internal pressure changes. The acoustic signals can be used to identify the pressure-induced leak through signal features of AE hits and AE energy; and the leaking pressure value was also determined by the pressure signals. After each monitoring system was verified, the flange joint was tested on the MTS test frame to thoroughly investigate the effect of combined tensile loads and internal pressure on the integrity of a bolted flange assembly using the proposed comprehensive integrity monitoring system. The real-time characteristic variations and leakage failure of the bolted flange connection was monitored and identified. Moreover, a leakage failure envelope was preliminarily obtained considering the internal pressure and tensile loads of the bolted flange joint corresponding to the different torques, which offered a useful guide to secure the performance and integrity of the bolted flange joint and mitigate the potential leakage failures in the field.

Furthermore, a touch-enabled bolt connection inspection approach using piezoceramic transducers was developed to expand the breadth of the monitoring system from on-land to offshore environment. A proof-of-concept clamping device that mimics two robotic fingers and uses magnets to secure a temporary and effective coupling between the transducers and the bolted connection, such as a flange. Upon touching, one PZT transducer mounted on one end of clamping device generates stress waves that propagate across the connection interface, and the other PZT transducer mounted on the other end of the clamp detects the propagating stress wave. Experimental studies validated the feasibility of the proposed touch-based inspection approach for identifying the status of bolted connection under the different applied torques in air and in salt water in laboratory. Moreover, an undersea ROV with robotic manipulator was leveraged to improve the touch-based inspection capacity for conducting a remote undersea inspection of subsea bolted connections. A robotic manipulator model was designed and fabricated. The fingertip of the manipulator was integrated with piezoceramic transducers and magnets to function as a sensing manipulator. The undersea operation of the ROV and the robotic manipulator can be remotely controlled. A field test was conducted in local marine environment to evaluate the inspection performance of the proposed ROV-enable remote undersea inspection method. The undersea field test demonstrated that the developed ROV-enabled robotic inspection approach was a promising undersea inspection technique to reliably evaluate the integrity of the subsea bolted connections under different torques on bolts.

In the future, the study of the leakage failure envelope can be enhanced by performing the cases of higher torques on the bolts through a higher capacity of test frame. The influence of the bending loads on the bolted flange joint concerning the sealing integrity is also meaningful to interpret the sealing integrity of the flange connections. Furthermore, the development of analytical models or finite element analysis to evaluate bolted connections considering the mating surface profile is useful to interpret the connection behaviors and verify the results under different loads. For subsea bolted connections inspection, the ROV-enabled remote undersea inspection device can be upgraded on the automatic operations of the ROV and the sensing manipulator for automatically inspecting the subsea bolted structures in future.

# References

[1] Y. Bai and Q. Bai, *Subsea engineering handbook*: Gulf Professional Publishing, 2018.

[2] E. Roos, H. Kockelmann, and R. Hahn, "Gasket characteristics for the design of bolted flange connections of metal-to-metal contact type," *International Journal of Pressure Vessels and Piping,* vol. 79, pp. 45-52, 2002.

[3] M. M. Krishna, M. Shunmugam, and N. S. Prasad, "A study on the sealing performance of bolted flange joints with gaskets using finite element analysis," *International Journal of Pressure Vessels and Piping,* vol. 84, pp. 349-357, 2007.

[4] National Academies of Sciences, and Medicine, *High-Performance Bolting Technology for Offshore Oil and Natural Gas Operations*. Washington, DC: The National Academies Press, 2018.

[5] Y. Bai and Q. Bai, *Subsea pipelines and risers*: Elsevier, 2005.

[6] S. M. Suggs and R. M. Meyer, "Gasket for flange connections," ed: Google Patents, 1998.

[7] J. Jiang, P. Zhang, D. Patil, H. N. Li, and G. Song, "Experimental studies on the effectiveness and robustness of a pounding tuned mass damper for vibration suppression of a submerged cylindrical pipe," *Structural Control and Health Monitoring,* 2017.

[8] B. D. C. Pinheiro and I. P. Pasqualino, "Fatigue analysis of damaged steel pipelines under cyclic internal pressure," *International Journal of Fatigue,* vol. 31, pp. 962-973, 2009.

[9] T. Alam, A. Islam, and Z. N. Farhat, "Slurry erosion of pipeline steel: Effect of velocity and microstructure," *Journal of Tribology,* vol. 138, 2016.

[10] P. C. Okonkwo, R. A. Shakoor, M. M. Zagho, and A. M. A. Mohamed, "Erosion behaviour of API X100 pipeline steel at various impact angles and particle speeds," *Metals,* vol. 6, p. 232, 2016.

[11] L. Huo, C. Li, T. Jiang, and H.-N. Li, "Feasibility study of steel bar corrosion monitoring using a piezoceramic transducer enabled time reversal method," *Applied Sciences,* vol. 8, p. 2304, 2018.

[12] J. Peng, L. Xiao, J. Zhang, C. Cai, and L. Wang, "Flexural behavior of corroded HPS beams," *Engineering Structures,* vol. 195, pp. 274-287, 2019.

[13] X. Zeng, F.-F. Dong, X.-D. Xie, and G.-F. Du, "A new analytical method of strain and deformation of pipeline under fault movement," *International Journal of Pressure Vessels and Piping,* vol. 172, pp. 199-211, 2019.

[14] J. Zhu, S. C. M. Ho, D. Patil, N. Wang, R. Hirsch, and G. Song, "Underwater pipeline impact localization using piezoceramic transducers," *Smart Materials and Structures,* vol. 26, p. 107002, 2017.

[15] M. Ho, S. El-Borgi, D. Patil, and G. Song, "Inspection and monitoring systems subsea pipelines: A review paper," *Structural Health Monitoring,* p. 1475921719837718, 2019.

[16] J. Ou and H. Li, "Structural health monitoring in mainland China: review and future trends," *Structural health monitoring*, vol. 9, pp. 219-231, 2010.

[17] S. Nagarajaiah and K. Erazo, "Structural monitoring and identification of civil infrastructure in the United States," *Structural Monitoring and Maintenance*, vol. 3, p. 51, 2016.

[18] P. C. Chang, A. Flatau, and S. Liu, "Health monitoring of civil infrastructure," *Structural health monitoring*, vol. 2, pp. 257-267, 2003.

[19] Y. An, E. Chatzi, S. H. Sim, S. Laflamme, B. Blachowski, and J. Ou, "Recent progress and future trends on damage identification methods for bridge structures," *Structural Control and Health Monitoring*, vol. 26, p. e2416, 2019.

[20] N. Li, F. Wang, and G. Song, "New entropy-based vibro-acoustic modulation method for metal fatigue crack detection: An exploratory study," *Measurement*, vol. 150, p. 107075, 2020.

[21] Q. Kong, R. H. Robert, P. Silva, and Y. Mo, "Cyclic crack monitoring of a reinforced concrete column under simulated pseudo-dynamic loading using piezoceramic-based smart aggregates," *Applied sciences*, vol. 6, p. 341, 2016.

[22] Q. Sun, B. Yuan, X. Mu, and W. Sun, "Bolt preload measurement based on the acoustoelastic effect using smart piezoelectric bolt," *Smart Materials and Structures*, vol. 28, p. 055005, 2019.

[23] Y.-J. Cha, K. You, and W. Choi, "Vision-based detection of loosened bolts using the Hough transform and support vector machines," *Automation in Construction*, vol. 71, pp. 181-188, 2016.

[24] T.-C. Nguyen, T.-C. Huynh, J.-Y. Ryu, J.-H. Park, and J.-T. Kim, "Bolt-loosening identification of bolt connections by vision image-based technique," in *Nondestructive Characterization and Monitoring of Advanced Materials, Aerospace, and Civil Infrastructure 2016*, 2016, p. 980413.

[25] C. Wang, N. Wang, M. Ho, X. Chen, and G. Song, "Design of a New Vision-based Method for the Bolts Looseness Detection in Flange Connections," *IEEE Transactions on Industrial Electronics*, 2019.

[26] J.-H. Park, T.-C. Huynh, S.-H. Choi, and J.-T. Kim, "Vision-based technique for bolt-loosening detection in wind turbine tower," *Wind Struct,* vol. 21, pp. 709-726, 2015.

[27] G. Morgenthal and N. Hallermann, "Quality assessment of unmanned aerial vehicle (UAV) based visual inspection of structures," *Advances in Structural Engineering,* vol. 17, pp. 289-302, 2014.

[28] B. Lei, Y. Ren, N. Wang, L. Huo, and G. Song, "Design of a new low-cost unmanned aerial vehicle and vision-based concrete crack inspection method," *Structural Health Monitoring,* p. 1475921719898862, 2020.

[29] Y. Ham, K. K. Han, J. J. Lin, and M. Golparvar-Fard, "Visual monitoring of civil infrastructure systems via camera-equipped Unmanned Aerial Vehicles (UAVs): a review of related works," *Visualization in Engineering,* vol. 4, p. 1, 2016.

[30] L. Wang and Z. Zhang, "Automatic detection of wind turbine blade surface cracks based on UAV-taken images," *IEEE Transactions on Industrial Electronics,* vol. 64, pp. 7293-7303, 2017.

[31] B. Lei, N. Wang, P. Xu, and G. Song, "New crack detection method for bridge inspection using UAV incorporating image processing," *Journal of Aerospace Engineering,* vol. 31, p. 04018058, 2018.

[32] C. Eschmann, C.-M. Kuo, C.-H. Kuo, and C. Boller, "Unmanned aircraft systems for remote building inspection and monitoring," in *Proceedings of the 6th European Workshop on Structural Health Monitoring, Dresden, Germany*, 2012, p. 13.

[33] P. Liu, A. Y. Chen, Y.-N. Huang, J.-Y. Han, J.-S. Lai, S.-C. Kang, T.H. Wu, M.C. Wen, and M.H. Tsai, "A review of rotorcraft unmanned aerial vehicle (UAV) developments and applications in civil engineering," *Smart Struct. Syst,* vol. 13, pp. 1065-1094, 2014.

[34] A. D. Hay, "Bolt, stud or fastener having an embedded fiber optic Bragg Grating sensor for sensing tensioning strain," ed: Google Patents, 1999.

[35] L. Ren, T. Feng, M. Ho, T. Jiang, and G. Song, "A smart “shear sensing” bolt based on FBG sensors," *Measurement,* vol. 122, pp. 240-246, 2018.

[36] Z. Zhang, M. Liu, Y. Liao, Z. Su, and Y. Xiao, "Contact acoustic nonlinearity (CAN)-based continuous monitoring of bolt loosening: Hybrid use of high-order harmonics and spectral sidebands," *Mechanical Systems and Signal Processing,* vol. 103, pp. 280-294, 2018.

[37] F. Huda, I. Kajiwara, N. Hosoya, and S. Kawamura, "Bolt loosening analysis and diagnosis by non-contact laser excitation vibration tests," *Mechanical Systems and Signal Processing,* vol. 40, pp. 589-604, 2013.

[38] Q. Kong, J. Zhu, S. C. M. Ho, and G. Song, "Tapping and listening: A new approach to bolt looseness monitoring," *Smart Materials and Structures,* vol. 27, p. 07LT02, 2018.

[39] Y. Zhang, X. Zhao, X. Sun, W. Su, and Z. Xue, "Bolt loosening detection based on audio classification," *Advances in Structural Engineering,* vol. 22, pp. 2882-2891, 2019.

[40] F. Wang, S. C. M. Ho, and G. Song, "Modeling and analysis of an impact-acoustic method for bolt looseness identification," *Mechanical Systems and Signal Processing,* vol. 133, p. 106249, 2019.

[41] G. Park, C. R. Farrar, F. L. di Scalea, and S. Coccia, "Performance assessment and validation of piezoelectric active-sensors in structural health monitoring," *Smart Materials and Structures,* vol. 15, p. 1673, 2006.

[42] G. Song, H. Gu, and Y.-L. Mo, "Smart aggregates: multi-functional sensors for concrete structures—a tutorial and a review," *Smart materials and structures,* vol. 17, p. 033001, 2008.

[43] L. Zhou, Y. Zheng, G. Song, D. Chen, and Y. Ye, "Identification of the structural damage mechanism of BFRP bars reinforced concrete beams using smart transducers based on time reversal method," *Construction and Building Materials,* vol. 220, pp. 615-627, 2019.

[44] Y. Xu, M. Luo, Q. Liu, G. Du, and G. Song, "PZT transducer array enabled pipeline defect locating based on time-reversal method and matching pursuit de-noising," *Smart Materials and Structures,* vol. 28, p. 075019, 2019.

[45] J. Zhang, Y. Li, Y. Huang, J. Jiang, and S.-C. M. Ho, "A feasibility study on timber moisture monitoring using piezoceramic transducer-enabled active sensing," *Sensors,* vol. 18, p. 3100, 2018.

[46] J. Jiang, C. Hei, Q. Feng, and J. Jiang, "Monitoring of epoxy-grouted bonding strength development between an anchored steel bar and concrete using PZT-enabled active sensing," *Sensors,* vol. 19, p. 2096, 2019.

[47] Y. Yang, C.-T. Ng, and A. Kotousov, "Bolted joint integrity monitoring with second harmonic generated by guided waves," *Structural Health Monitoring,* vol. 18, pp. 193-204, 2019.

[48] T. Wang, G. Song, Z. Wang, and Y. Li, "Proof-of-concept study of monitoring bolt connection status using a piezoelectric based active sensing method," *Smart Materials and Structures,* vol. 22, p. 087001, 2013.

[49] F. Wang, Z. Chen, and G. Song, "Monitoring of multi-bolt connection looseness using entropy-based active sensing and genetic algorithm-based least square support vector machine," *Mechanical Systems and Signal Processing,* vol. 136, p. 106507, 2020.

[50] T. Wang, G. Song, S. Liu, Y. Li, and H. Xiao, "Review of bolted connection monitoring," *International Journal of Distributed Sensor Networks,* vol. 9, p. 871213, 2013.

[51] S. Bhalla, A. S. K. Naidu, C. W. Ong, and C.-K. Soh, "Practical issues in the implementation of electromechanical impedance technique for NDE," in *Smart Structures, Devices, and Systems*, 2002, pp. 484-494.

[52] W. S. Na and J. Baek, "A review of the piezoelectric electromechanical impedance based structural health monitoring technique for engineering structures," *Sensors,* vol. 18, p. 1307, 2018.

[53] Y. Yang, Y. Y. Lim, and C. K. Soh, "Practical issues related to the application of the electromechanical impedance technique in the structural health monitoring of civil structures: I. Experiment," *Smart Materials and Structures,* vol. 17, p. 035008, 2008.

[54] J. Zhang, C. Zhang, J. Xiao, and J. Jiang, "A PZT-Based Electromechanical Impedance Method for Monitoring the Soil Freeze–Thaw Process," *Sensors,* vol. 19, p. 1107, 2019.

[55] S. Bhalla, P. A. Vittal, and M. Veljkovic, "Piezo-impedance transducers for residual fatigue life assessment of bolted steel joints," *Structural Health Monitoring,* vol. 11, pp. 733-750, 2012.

[56] T. Panidis, I. Pavelko, V. Pavelko, S. Kuznetsov, and I. Ozolinsh, "Bolt-joint structural health monitoring by the method of electromechanical impedance," *Aircraft Engineering and Aerospace Technology: An International Journal,* 2014.

[57] L. Huo, D. Chen, Y. Liang, H. Li, X. Feng, and G. Song, "Impedance based bolt pre-load monitoring using piezoceramic smart washer," *Smart Materials and Structures,* vol. 26, p. 057004, 2017.

[58] F. Wang, S. C. M. Ho, L. Huo, and G. Song, "A novel fractal contact-electromechanical impedance model for quantitative monitoring of bolted joint looseness," *Ieee Access,* vol. 6, pp. 40212-40220, 2018.

[59] G. Park, H. Sohn, C. R. Farrar, and D. J. Inman, "Overview of piezoelectric impedance-based health monitoring and path forward," *Shock and vibration digest*, vol. 35, pp. 451-464, 2003.

[60] W. Li, T. Liu, D. Zou, J. Wang, and T.-H. Yi, "PZT based smart corrosion coupon using electromechanical impedance," *Mechanical Systems and Signal Processing,* vol. 129, pp. 455-469, 2019.

[61] V. G. M. Annamdas and C. K. Soh, "Application of electromechanical impedance technique for engineering structures: review and future issues," *Journal of Intelligent material systems and structures,* vol. 21, pp. 41-59, 2010.

[62] H. Wadley and R. Mehrabian, "Acoustic emission for materials processing: a review," *Materials Science and Engineering,* vol. 65, pp. 245-263, 1984.

[63] C. U. Grosse and M. Ohtsu, *Acoustic emission testing*: Springer Science & Business Media, 2008.

[64] J. Yu, P. Ziehl, B. Zárate, and J. Caicedo, "Prediction of fatigue crack growth in steel bridge components using acoustic emission," *Journal of Constructional Steel Research,* vol. 67, pp. 1254-1260, 2011.

[65] M. Shigeishi, S. Colombo, K. Broughton, H. Rutledge, A. Batchelor, and M. Forde, "Acoustic emission to assess and monitor the integrity of bridges," *Construction and building materials,* vol. 15, pp. 35-49, 2001.

[66] L. Golaski, P. Gebski, and K. Ono, "Diagnostics of reinforced concrete bridges by acoustic emission," *Journal of acoustic emission,* vol. 20, pp. 83-89, 2002.

[67] A. Nair and C. Cai, "Acoustic emission monitoring of bridges: Review and case studies," *Engineering structures,* vol. 32, pp. 1704-1714, 2010.

[68] A. Berkovits and D. Fang, "Study of fatigue crack characteristics by acoustic emission," *Engineering Fracture Mechanics,* vol. 51, pp. 401-416, 1995.

[69] T. Roberts and M. Talebzadeh, "Acoustic emission monitoring of fatigue crack propagation," *Journal of Constructional Steel Research,* vol. 59, pp. 695-712, 2003.

[70] R. Miller, A. Pollock, D. Watts, J. Carlyle, A. Tafuri, and J. Yezzi Jr, "A reference standard for the development of acoustic emission pipeline leak detection techniques," *Ndt & E International,* vol. 32, pp. 1-8, 1999.

[71] S. Li, Y. Wen, P. Li, J. Yang, and L. Yang, "Leak detection and location for gas pipelines using acoustic emission sensors," in *2012 IEEE International Ultrasonics Symposium,* 2012, pp. 957-960.

[72] L.-Y. Sun, Y.-B. Li, Z.-G. Qu, S.-J. Jin, and Y. Zhou, "Study on acoustic emission detection for pipeline leakage based on EMD signal analysis method," *Journal of Vibration and Shock,* vol. 26, pp. 161-164, 2007.

[73] M. R. Lee and J. H. Lee, "Acoustic emission technique for pipeline leak detection," in *Key Engineering Materials*, 2000, pp. 887-892.

[74] H. Nakamura, M. Ohtsu, M. Enoki, Y. Mizutani, M. Shigeishi, H. Inaba, M. Nakano, T. Shiotani, S. Yuyama, and S. Sugimoto, *Practical acoustic emission testing*: Springer, 2016.

[75] G. Song, H. Gu, and H. Li, "Application of the piezoelectric materials for health monitoring in civil engineering: an overview," in *Engineering, Construction, and Operations in Challenging Environments: Earth and Space 2004*, ed, 2004, pp. 680-687.

[76] J. F. Tressler, S. Alkoy, and R. E. Newnham, "Piezoelectric sensors and sensor materials," *Journal of electroceramics*, vol. 2, pp. 257-272, 1998.

[77] R. Capocci, G. Dooly, E. Omerdić, J. Coleman, T. Newe, and D. Toal, "Inspection-class remotely operated vehicles—A review," *Journal of Marine Science and Engineering*, vol. 5, p. 13, 2017.

[78] R. D. Christ and R. L. Wernli Sr, *The ROV manual: a user guide for remotely operated vehicles*: Butterworth-Heinemann, 2013.

[79] P. I. Macreadie, D. L. McLean, P. G. Thomson, J. C. Partridge, D. O. Jones, A. R. Gates, M.C. Benfield, and S.P. Collin, "Eyes in the sea: unlocking the mysteries of the ocean using industrial, remotely operated vehicles (ROVs)," *Science of the Total Environment*, vol. 634, pp. 1077-1091, 2018.

[80] D. McStay, J. McIlroy, A. Forte, F. Lunney, T. Greenway, K. Thabeth, and G. Dean, "A new tool for the rapid remote detection of leaks from subsea pipelines

during remotely operated vehicle inspections," *Journal of Optics A: Pure and Applied Optics,* vol. 7, p. S346, 2005.

[81] S. Sivčev, J. Coleman, E. Omerdić, G. Dooly, and D. Toal, "Underwater manipulators: A review," *Ocean Engineering,* vol. 163, pp. 431-450, 2018.

[82] C. C. Ciang, J.-R. Lee, and H.-J. Bang, "Structural health monitoring for a wind turbine system: a review of damage detection methods," *Measurement science and technology,* vol. 19, p. 122001, 2008.

[83] F. Wang and G. Song, "Monitoring of multi-bolt connection looseness using a novel vibro-acoustic method," *Nonlinear Dynamics,* pp. 1-12, 2020.

[84] J. Zhang, Y. Li, Y. Huang, J. Jiang, and S.-C. Ho, "A feasibility study on timber moisture monitoring using piezoceramic transducer-enabled active sensing," *Sensors,* vol. 18, p. 3100, 2018.

[85] F. Han, J. Jiang, K. Xu, and N. Wang, "Damage Detection of Common Timber Connections Using Piezoceramic Transducers and Active Sensing," *Sensors,* vol. 19, p. 2486, 2019.

[86] S. Bhalla, S. Moharana, V. Talakokula, and N. Kaur, *Piezoelectric materials: applications in SHM, energy harvesting and biomechanics*: John Wiley & Sons, 2016.

[87] X. Qing, W. Li, Y. Wang, and H. Sun, "Piezoelectric transducer-based structural health monitoring for aircraft applications," *Sensors,* vol. 19, p. 545, 2019.

[88] S. Müller, "Transfer-Function Measurement with Sweeps DIRECTOR’S CUT INCLUDING PREVIOUSLY UNRELEASED MATERIAL," 2001.

[89] L. Cohen, *Time-frequency analysis* vol. 778: Prentice hall, 1995.

[90] W. J. Staszewski and A. N. Robertson, "Time–frequency and time–scale analyses for structural health monitoring," *Philosophical Transactions of the Royal Society A: Mathematical, Physical and Engineering Sciences,* vol. 365, pp. 449-477, 2007.

[91] J.-B. Ihn and F.-K. Chang, "Detection and monitoring of hidden fatigue crack growth using a built-in piezoelectric sensor/actuator network: I. Diagnostics," *Smart materials and structures,* vol. 13, p. 609, 2004.

[92] J.-B. Ihn and F.-K. Chang, "Detection and monitoring of hidden fatigue crack growth using a built-in piezoelectric sensor/actuator network: II. Validation using riveted joints and repair patches," *Smart materials and structures,* vol. 13, p. 621, 2004.

[93] I. Antoniadou, G. Manson, W. Staszewski, T. Barszcz, and K. Worden, "A time–frequency analysis approach for condition monitoring of a wind turbine gearbox under varying load conditions," *Mechanical Systems and Signal Processing,* vol. 64, pp. 188-216, 2015.

[94] S. Qian and D. Chen, "Joint time-frequency analysis," *IEEE Signal Processing Magazine,* vol. 16, pp. 52-67, 1999.

[95] M. Portnoff, "Time-frequency representation of digital signals and systems based on short-time Fourier analysis," *IEEE Transactions on Acoustics, Speech, and Signal Processing,* vol. 28, pp. 55-69, 1980.

[96] G. G. Yen and K.-C. Lin, "Wavelet packet feature extraction for vibration monitoring," *IEEE transactions on industrial electronics*, vol. 47, pp. 650-667, 2000.

[97] Z. Sun and C. Chang, "Statistical wavelet-based method for structural health monitoring," *Journal of structural engineering*, vol. 130, pp. 1055-1062, 2004.

[98] X. Zhao and B. Ye, "Convolution wavelet packet transform and its applications to signal processing," *Digital Signal Processing*, vol. 20, pp. 1352-1364, 2010.

[99] J.-G. Han, W.-X. Ren, and Z.-S. Sun, "Wavelet packet based damage identification of beam structures," *International Journal of Solids and Structures*, vol. 42, pp. 6610-6627, 2005.

[100] M. Gokhale and D. K. Khanduja, "Time domain signal analysis using wavelet packet decomposition approach," *Int'l J. of Communications, Network and System Sciences*, vol. 3, p. 321, 2010.

[101] M. Gokhale and D. K. Khanduja, "Time domain signal analysis using wavelet packet decomposition approach," *International Journal of Communications, Network and System Sciences*, vol. 3, p. 321, 2010.

[102] C. Liang, F. P. Sun, and C. A. Rogers, "Coupled electro-mechanical analysis of adaptive material systems-determination of the actuator power consumption and system energy transfer," *Journal of intelligent material systems and structures*, vol. 8, pp. 335-343, 1997.

[103] S. Merlo, M. Norgia, and S. Donati, "Handbook of Optical Fibre Sensing Technology," ed: New York: John Wiley & Sons, 2002.

[104] M. Majumder, T. K. Gangopadhyay, A. K. Chakraborty, K. Dasgupta, and D. K. Bhattacharya, "Fibre Bragg gratings in structural health monitoring—Present status and applications," *Sensors and Actuators A: Physical*, vol. 147, pp. 150-164, 2008.

[105] Y. B. Lin, C. L. Pan, Y. H. Kuo, K. C. Chang, and J. C. Chern, "Online monitoring of highway bridge construction using fiber Bragg grating sensors," *Smart Materials and Structures*, vol. 14, p. 1075, 2005.

[106] C. Barbosa, N. Costa, L. Ferreira, F. Araújo, H. Varum, A. Costa, C. Fernandes, and H. Rodrigues, "Weldable fibre Bragg grating sensors for steel bridge monitoring," *Measurement Science and Technology*, vol. 19, p. 125305, 2008.

[107] R. Tennyson, A. Mufti, S. Rizkalla, G. Tadros, and B. Benmokrane, "Structural health monitoring of innovative bridges in Canada with fiber optic sensors," *Smart materials and Structures*, vol. 10, p. 560, 2001.

[108] Z. Jia, L. Ren, D. Li, and H. Li, "Fiber Bragg grating strain sensor for measurement of vortex-induced vibration," in *Earth and Space 2010: Engineering, Science, Construction, and Operations in Challenging Environments*, ed, 2010, pp. 1601-1608.

[109] Z. Jia, L. Ren, H. Li, T. Jiang, and W. Wu, "Pipeline leakage identification and localization based on the fiber Bragg grating hoop strain measurements and particle swarm optimization and support vector machine," *Structural Control and Health Monitoring*, vol. 26, p. e2290, 2019.

[110] X. Huang, D. Sheng, K. Cen, and H. Zhou, "Low-cost relative humidity sensor based on thermoplastic polyimide-coated fiber Bragg grating," *Sensors and Actuators B: Chemical,* vol. 127, pp. 518-524, 2007.

[111] T. Yeo, T. Sun, and K. Grattan, "Fibre-optic sensor technologies for humidity and moisture measurement," *Sensors and Actuators A: Physical,* vol. 144, pp. 280-295, 2008.

[112] P. Kronenberg, P. K. Rastogi, P. Giaccari, and H. G. Limberger, "Relative humidity sensor with optical fiber Bragg gratings," *Optics letters,* vol. 27, pp. 1385-1387, 2002.

[113] M. Schroeck, W. Ecke, and A. Graupner, "Strain monitoring in steel rock bolts using FBG sensor arrays," in *Applications of Optical Fiber Sensors*, 2000, pp. 298-304.

[114] S. C. M. Ho, W. Li, B. Wang, and G. Song, "A load measuring anchor plate for rock bolt using fiber optic sensor," *Smart Materials and Structures,* vol. 26, p. 057003, 2017.

[115] G. Song, W. Li, B. Wang, and S. C. M. Ho, "A review of rock bolt monitoring using smart sensors," *Sensors,* vol. 17, p. 776, 2017.

[116] J. Jiang, S. C. M. Ho, T. Tippitt, Z. Chen, and G. Song, "Feasibility study of a touch-enabled active sensing approach to inspecting subsea bolted connections using piezoceramic transducers," *Smart Materials and Structures*, 2020.